# Purely Optical Tomography: Atlas-Based Reconstruction of Brain Activation

by

Anna Custo

Submitted to the Department of Electrical Engineering and Computer Science
in partial fulfillment of the requirements for the degree of

Doctor of Philosophy in Computer Science and Engineering

at the

MASSACHUSETTS INSTITUTE OF TECHNOLOGY

June 2008



Author . .....
Department of Electrical Engineering and Computer Science
May 16, 2008

Certified by . .....
W. Eric L. Grimson
Bernard Gordon Professor of Medical Engineering, CSAIL, MIT
Thesis Supervisor

Certified by . .....
William M. Wells III
Associate Professor of Radiology, Harvard Medical School
Thesis Supervisor

Accepted by . .....
Terry P. Orlando
Chairman, Department Committee on Graduate Students

# Purely Optical Tomography: Atlas-Based Reconstruction of Brain Activation

by

Anna Custo

Submitted to the Department of Electrical Engineering and Computer Science
on May 16, 2008, in partial fulfillment of the
requirements for the degree of
Doctor of Philosophy in Computer Science and Engineering

## Abstract

Diffuse Optical Tomography (DOT) is a relatively new method used to image blood volume and oxygen saturation in vivo. Because of its relatively poor spatial resolution (typically no better than 1-2 cm), DOT is increasingly combined with other imaging techniques, such as MRI, fMRI and CT, which provide high-resolution structural information to guide the characterization of the unique physiological information offered by DOT. This work aims at improving DOT by offering new strategies for a more accurate, efficient, and faster image processor. Specifically, after investigating the influence of Cerebral Spinal Fluid (CSF) properties on the optical measurements, we propose using a realistic segmented head model that includes a novel CSF segmentation approach for a more accurate solution of the DOT forward problem. Moreover, we outline the benefits and applicability of a Diffusion Approximation-based faster forward model solver. We also describe a new registration algorithm based on superficial landmarks which is an essential tool for the purely optical tomographic image process proposed here.

A purely optical tomography of the brain during neural activity will greatly enhance DOT applicability and provide many advantages, in the sense that DOT low cost, portability and non-invasiveness would be fully exploited without the compromises due to the MRI role in the DOT forward image process. We achieve a purely optical tomography by using a generalized head model (or *atlas*) in place of the subject specific anatomical MRI. We validate the proposed imaging protocol by comparing measurements derived from the DOT forward problem solution obtained using the subject specific anatomical model versus these acquired using the atlas registered to the subject, using a database of 31 healthy human subjects, and focusing on a set of 12 functional regions of interest. We conclude our study presenting data obtained from 3 experimental subjects having undergone median nerve stimuli. We apply our purely optical tomography protocol to the 3 subjects and analyze the observations derived from both the DOT forward and inverse solutions. The experimental results demonstrate that it is possible to guide the DOT forward problem with a general anatomical model in place of the subject's specific head geometry to localize the macroanatomical structures of neural activity.

Thesis Supervisor: W. Eric L. Grimson
Title: Bernard Gordon Professor of Medical Engineering, CSAIL, MIT

Thesis Supervisor: William M. Wells III
Title: Associate Professor of Radiology, Harvard Medical School

Thesis Committee: David A. Boas
Title: Associate Professor of Radiology, Harvard Medical School

Thesis Committee: Berthold K.P. Horn
Title: Professor of Computer Science, CSAIL, MIT

Thesis Committee: Anders Dale
Title: Professor of Neurosciences and Radiology, UCSD

# Acknowledgments

This work is the result of the efforts of many and in particular I would like to thank my advisors: Prof. Eric Grimson, for having words of encouragements when I most needed them and for supporting me financially for so many years; Prof. Sandy Wells, for guiding me every step of the way and patiently teaching me how to be an independent researcher; Prof. David Boas, for providing the key ideas that made this work possible and for checking the conceptual soundness and novelty of this research. This work is also the fruit of key collaborations and contributions and I would like to especially acknowledge the role of Ippeita Dan, whose group provided important algorithms and insights, Anders Dale, who helped shaping up the initial stages of this research, Elizabeth Hillman, who patiently taught me how to write a good journal paper, Rickson Mesquita, who provided the experimental data, Leonardo Angelone, who provided the single subject dataset, Bruce Fischl, who helped and guided many stages of this work and provided the 32 subjects dataset, and Dough Greve, who helped clarifying the usage of some tools of FreeSurfer.

In some way it seems like yesterday when I started my PhD at MIT, in September 2001, and yet it seems like a lifetime ago. I would like to take the opportunity to thank the people that made this journey and its conclusion possible, starting with my family, to whom this thesis is dedicated: they have inspired me, encouraged me, prayed for me and supported me in many ways throughout my 80 months at MIT and I would not have made it without them: THANK YOU. I would also like to thank my friends and colleagues: in many cases they have been my "family" at MIT, they have brought that ounce of balance my life is permanently lacking, they offered a shoulder to lean on when I needed it, they put me back on my feet when I was trembling, they shared my moments of sadness and of happiness, they laughed and cried with me: they cared. Lucy, Francesca, Gergana, and the rest of my friends: thank you for being in my life.

# Contents

# List of Figures

# List of Tables

# Chapter 1

# Introduction

## 1.1 Diffuse Optical Tomography

Diffuse Optical Tomography (DOT) is a relatively new method that can be used to image blood volume and oxygen saturation in vivo. It uses near infrared light and has the advantage of low cost and portability. The feasibility of diffuse optical imaging techniques is due to the properties of near infrared light in biological tissue. The optical absorption coefficient ($\mu_a$) depends on the total hemoglobin concentration and oxygenation within the tissue; therefore, calculating $\mu_a$ provides useful information about the physiological conditions of the tissue [23]. For example, during the last few years DOT has been tested for application to imaging breast cancer [109, 24, 72, 114, 59, 110, 84, 48] and brain function [69, 121, 68, 49, 81, 102, 55, 120]. Our main contributions to improved optical tomography are twofold: (1) we increase the accuracy of the head model used in the DOT forward problem by designing a better segmentation of the critical Cerebral Spinal Fluid (CSF) layer; (2) we exploit DOT specific advantages by eliminating the Magnetic Resonance Imaging (MRI) component of the DOT image process; we achieve this goal by using a generalized head model (hereby called an atlas) in place of the subject specific anatomical MRI, and measuring the error thus introduced experimentally (in the DOT forward and inverse solutions) and in a simulation framework (in the DOT forward solution).

### 1.1.1 Physiology

From the imaging point of view, the consequences of neural activity are the transmission of messages via electrical pulses and the change of status of the cerebral blood vessels. The first phenomenon is captured by Electroencephalography (EEG), which is the measurement of the electrical phenomena associated with neural signaling during brain activity. Electrodes are placed on the scalp and record part of the single axon action potentials; more effective but invasive modalities to measure the neuron activity are intracranial (or subdural) EEG and Electrocorticography (ECoG): these techniques increase the SNR and spatial resolution of the recordings by placing electrodes directly on the surface of the cortex. Magnetoencephalography (MEG) is another imaging modality measuring the electrical signal produced during brain ac-

tivity: MEG records the magnetic fields produced by electrical activity in the brain via extremely sensitive superconducting quantum interference devices (SQUIDs). On the other hand, blood related changes due to neural activity are measured by functional MRI (fMRI) and Diffuse Optical Tomography (DOT). During brain activity the local capillaries response to the increasing request of oxygen supplies includes vaso-dilation, increase of blood flow and of the amount of nutrients delivered to the active neurons. Among these nutrients is oxygen, carried by hemoglobin, which is called oxy-hemoglobin (HbO) when it is enriched with oxygen and deoxy-hemoglobin (HbR) when it is not. 'Hemodynamic' refers to changes in blood flow and blood oxygenation and is coupled with neural activity [26] even though the precise relationship between the two is still under investigation. It is known, though, that the increase of blood flow due to brain activation occurs after a delay of approximately 1-5 seconds, the peak rises over 4-5 seconds and then falls back to baseline (typically slightly undershooting the baseline level) [6]. fMRI images the hemodynamic changes because oxy-hemoglobin is diamagnetic whereas deoxy-hemoglobin is paramagnetic and therefore the local magnetic resonance signal varies with the local oxygenation level (from which the name of the fMRI measurements, Blood Oxygen Level Dependent, or BOLD, signal). BOLD contrast increases with the increase of oxygenated hemoglobin because the blood magnetic susceptibility becomes closer to the tissue magnetic susceptibility. The overall BOLD contrast, however, is determined by the combined effect of the vascular oxygenation level and the Cerebral Blood Flow (CBF): an increase in CBF greater than the change in oxygen consumption will lead to an increased BOLD signal and similarly a decrease in CBF outstripping hemoglobin oxygenation changes will cause a decreased BOLD signal intensity.

Diffuse Optical Imaging (DOI) of brain activity includes applications like Event Related Optical Signal (EROS), a fast 2D topographic measurement of cellular activity during brain activation using the scattering properties of the neurons [56], Near Infrared Spectroscopy (NIRS), that uses the electromagnetic spectrum of oxy- and deoxy-hemoglobin to measure the vascular effect of brain activation [122], and Diffuse Optical Tomography (DOT), which computes a tomographic reconstruction of the 3D head volume enabling long term neural activity monitoring as well as lesion diagnosis. DOT equipment has a high temporal resolution, comparable to electroencephalography and magnetoencephalography (milliseconds), and its spatial resolution is about one millimeter in voxel size, but it can only probe a few centimeters deep (just the cortical surface) due to the rapidity of photons' absorption.

Although the neuro-vascular coupling is still under investigation, it appears that the metabolic change of oxygen carried by the hemoglobin is a good indication of brain activity, even though it is not tightly synchronized with the cortical electrical signals. Some even hypothesize that there is a more subtle coupling between blood flow and neurons, claiming that there may be highly specific concentrations of blood flow that target specific neuronal activity in a way that affects the properties of the neurons [91]. Understanding the relationship between Cerebral Blood Flow (CBF), Cerebral Blood Volume (CBV), and changes in blood oxygenation during neuronal

activation will enable us to discern the contributions of flow and oxygen consumption to the hemodynamic response as measured by fMRI, and thus differences between the effects of vascular plumbing and the Cerebral Metabolic Rate of Oxygen ($CMRO_2$), which will lead us to a better interpretation of hemodynamic signals for the neurosciences, better exploiting longitudinal and cross-subject studies, and likely having a significant impact in diagnosis and treatment of neuro-diseases such as stroke, Alzheimer's Disease (AD), and psychiatric disorders. $CMRO_2$ is derived from other hemodynamic parameters using the formula [88]:

$$(1 + rCMRO_2) = (1 + rCBF)(1 + rCBV_{ven})^{-1}(1 + r[HbR]_{ven}) \ , \qquad (1.1)$$

where the $r$ suffix stands for relative values during activation with respect to baseline values, $r[HbR]_{ven}$ is the relative concentration of deoxy-hemoglobin in the venous vascular compartment and $rCBV_{ven}$ is the relative cerebral blood volume in the venous capillary compartment [71, 80, 74]. In order to estimate $rCMRO_2$ with fMRI it is necessary to use the assumption of a relationship between blood flow and volume, otherwise it is not possible to measure relative changes in CBV during activation; the Grubb relation $CBV = CBF^{\alpha}$ with $\alpha = 0.38$ [60] is typically considered applicable during brain activation in humans. Diffuse Optical Tomography reduces the reliance on the flow-volume model by providing more quantitative experimental data for estimating $rCMRO_2$. The brain oxygen metabolism can also be written as:

$$rCMRO_2 = CBF(SaO_2 - SvO_2) \ , \qquad (1.2)$$

where $SaO_2$ and $SvO_2$ are the arterial and venous oxygen saturation respectively and

$$SvO_2 = \frac{[HbO]_{ven}}{[HbO]_{ven} + [HbR]_{ven}} \ ,$$

and $[HbR]_{ven}$ and $[HbO]_{ven}$ indicates the deoxy- and oxy-hemoglobin concentrations in the venous compartment respectively; if we assume $SaO_2$ to equal 1 (to simplify notation, but not a necessary assumption) we obtain the $rCMRO_2$ expression of Equation 1.1. These important measurements of brain activation are calculated using a linear model relating small local changes of absorption coefficient $\mu_a$ (measured by optical tomography) to concentration of oxy- and deoxy-hemoglobin [65, 70]:

$$\begin{cases} \mu_{a,780} = [HbR] \cdot \varepsilon_{[HbR],780} + [HbO] \cdot \varepsilon_{[HbO],780} \\ \mu_{a,830} = [HbR] \cdot \varepsilon_{[HbR],830} + [HbO] \cdot \varepsilon_{[HbO],830} \end{cases} \ , \qquad (1.3)$$

where $[HbR]$ and $[HbO]$ are the concentration of deoxy- and oxy-hemoglobin respectively, $\varepsilon_{[HbO],780}$ and $\varepsilon_{[HbR],780}$ are the extinction coefficients of oxy- and deoxy-hemoglobin at wavelength $\lambda = 780$ respectively. $\varepsilon_{[HbO]}$ and $\varepsilon_{[HbR]}$ are known quantities that measure how well hemoglobin scatters and absorbs electromagnetic radiation: a low extinction coefficient means that the radiation easily penetrates it. These two wavelengths are chosen to maximize SNR in highly scattering biological tissues because, at these wavelengths, oxy- and deoxy-hemoglobin are the dominant light ab-

sorbers and their concentrations are sufficiently low ($< 100\mu$M) to allow light to pass through several centimeters of tissue and still be detected [112, 65, 38, 18].

### 1.1.2 Mathematical models

The DOT imaging problem can be described as follows: near infrared light is scattered in a medium with optical properties $x$ and some light intensity $y$ is recorded at the detectors' positions. Solving an imaging problem (described as $f(x) = y$; solve for $x$) requires a good combination of forward and inverse models. The former models the process producing the set of measurements (establishing the rules to calculate $f(x)$). The inverse problem arises when it is necessary to recover an image of the optical properties of the medium from the observed data (i.e. $x = f^{-1}(y)$). This problem is ill posed because the number of unknown parameters (in the order of thousands) is many times larger than the number of measurements (in the order of hundreds); hence the inverse procedure typically involves use of regularization techniques [14, 9]. Because of its relatively poor spatial resolution (typically no better than 1-2 cm), DOT is increasingly combined with other imaging techniques, such as MRI and CT, which provide high-resolution structural information to guide the characterization of the unique physiological information offered by DOT [15, 84, 12, 105, 92, 19].

#### 1.1.2.1 Forward problem

Near Infrared light shone on a semi-infinite biological medium is rapidly absorbed but a small portion of it scatters back to the surface. Photon transport in highly scattering tissues is modeled analytically by the Radiative Transfer Equation (RTE) and numerically with Monte Carlo simulations. RTE is difficult to solve and therefore the numerical solution is preferred as an effective way of predicting light intensity exiting the medium and thus inferring baseline optical properties of the medium itself or their changes. RTE can be solved by introducing approximations such as the diffusion approximation (described below) which has more computationally efficient numerical solutions but is less accurate than Monte Carlo simulations.

**1.1.2.1.1 The physics:** Figure 1-1 describes photon migration in a human head: light is injected in the medium via a bundle of fiber optics (called optode) and travels through the various tissues (in the figure the blue layer represents skin-type tissues, light blue stands for skull, yellow for Cerebral Spinal Fluid (CSF), red for gray matter and maroon indicates white matter). Each tissue is optically described by absorption ($\mu_a$) and scattering ($\mu_s$) coefficients that characterize the level of attenuation of the injected light; in other words, $\mu_a$ and $\mu_s$ are the inverse of the photon mean free path for absorption and scattering respectively [63]. For a medium with no scattering the level of attenuation is empirically described by the Beer-Lambert Law:

$$\Psi = -\log_{10}\frac{\Phi}{\Phi_o},$$

where $\Psi$ is the absorbance of the material, $\Phi$ is the intensity of light at a specified wavelength $\lambda$ as it exits the medium, and $\Phi_o$ is the intensity of the incident light. The physical model of light propagation in heterogeneous media (such as biological tissues) accounts for the combined effect of the scattering events and the level of absorption of the different tissue types photons traverse. The Radiative Transfer Equation (RTE), the Diffusion Approximation (DA) or the Monte Carlo numerical simulation are the most common methods to predict light intensity ($\Phi$ from Figure 1-1) as a function of the injected fluence rate ($\Phi_o$ from Figure 1-1) and the scattering and absorbing effect of the medium. Figure 1-1 shows an example of likely trajectories of photons injected at position $\mathbf{r}_o$ and time $t_o$: if a receiver (which is a bundle of optical fibers dedicated to receiving rather than sending photons) is placed at position $\mathbf{r}_1$ it will collect at time $t_1$ photons that traveled along the path indicated by the gray arrows connecting $\Phi_o$ to $\Phi$, whereas, if a detector is placed too far from the source (the white square in the figure) it will not receive any photon due to the exponential decay of light intensity in highly scattering and absorbing tissues. Detectors placed closest to the source will receive more light but will not probe deep tissues (for example the detector placed in $\mathbf{r}_2$ receives photons that traveled through deeper tissues than the detector in $\mathbf{r}_1$) and since we are interested in probing the gray matter, has been empirically determined that a source-detector separation of 28-38 mmin an adult head is the best compromise between SNR and depth sensitivity.

**1.1.2.1.2 Radiative Transfer Equation:** The Radiative Transfer Equation [118] models the energy transfer due to light propagation in a tissue. Before discussing the transfer equation we introduce some relevant physical quantities, starting with the radiance, which is the flow of radiation energy through a small area in the radiation field at position vector $\mathbf{r}$, with direction $\hat{s}$ at time $t$:

*Radiance*:

$$R(\mathbf{r}, \hat{s}, t) \ , \tag{1.4}$$

which is energy flow per unit area per unit solid angle per unit time [number of photons / (s mm$^2$ sr)].

*Fluence rate* or *Intensity*:

$$\Phi(\mathbf{r}, t) = \int_{4\pi} R(\mathbf{r}, \hat{s}, t) d\Omega \ , \tag{1.5}$$

which has the dimensions of energy flow per unit area [number of photons / (s mm$^2$)].

*Fluence*:

$$F(\mathbf{r}) = \int_{-\infty}^{+\infty} \Phi(\mathbf{r}, t) dt \ , \tag{1.6}$$

which has the dimensions of energy per unit area [number of photons / mm$^2$]; sometimes in this text the letter $\Phi$ is used to indicate fluence as it better relates to the

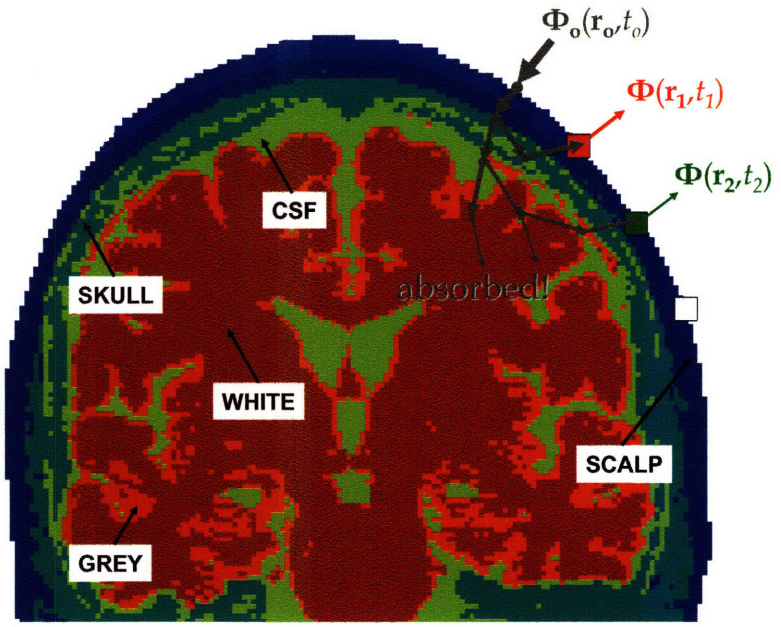


Figure 1-1: Photon migration in a human head: light is injected in the medium via a bundle of optical fibers (called optode) and travels through the various tissues (in the figure the blue layer represents skin-type tissues, light blue stands for skull, yellow for Cerebral Spinal Fluid (CSF), red for gray matter and maroon indicates white matter). Each tissue is optically characterized by absorption ($\mu_a$) and scattering ($\mu_s$) coefficients that describe the level of attenuation of the injected light. $\Phi(\mathbf{r}_i, t_i)$ and $\Phi_o(\mathbf{r}_o, t_o)$ are the detected light intensity at position $\mathbf{r}_i$ and time $t_i$ and the injected fluence rate respectively. The gray arrows show examples of likely trajectories of the injected photons: if a detector (red, green or white squares) is placed at position $\mathbf{r}_1$ it will collect at time $t_1$ photons that traveled along the path indicated by the gray arrows connecting $\Phi_o(\mathbf{r}_o, t_o)$ to $\Phi(\mathbf{r}_1, t_1)$ (red square); whereas, if a detector is placed too far from the source (the white square) it will not receive any photon due to the exponential decay of light intensity in highly scattering and absorbing tissues. The thickness of the gray arrows represents the light intensity as it exponentially decreases with depth/source-detector separation. Detectors placed closest to the source will receive more light but will not probe deep tissues (for example the detector placed in $\mathbf{r}_2$, green square, receives photons that traveled through deeper tissues than the detector in $r_1$, red square) and since we are interested in probing the cortex, the source-detector separation of 28-38 mmin an adult head is the best compromise between SNR and depth sensitivity.

fluence rate from which it is derived by time integration.

*Current density* (or *energy flux*):

$$\vec{J}(\mathbf{r},t) = \int_{4\pi} \hat{s} R(\mathbf{r},\hat{s},t) d\Omega \ , \tag{1.7}$$

which has the dimensions of energy flow per unit area [number of photons / (s mm$^2$)]. $\vec{J}$ is basically the fluence rate pointing in the prevalent direction of the energy flow.

The Radiative Transfer Equation (also found in the literature as the radiative transport equation) is a differential equation describing radiance, and can be derived via conservation of energy. The RTE describes the competing effects on energy loss of a beam of light due to divergence (effect of scattering away from the beam) and extinction (effect of absorption) and energy gain due to convergence (which is the effect of scattering toward the beam) and the contribution of the injected photons. Optical properties such as refractive index $n$, absorption coefficient $\mu_a$, scattering coefficient $\mu_s$, and scattering anisotropy $g$ vary spatially but are considered time-invariant. The expression of the RTE (or Boltzmann transport equation) is [118, 63]:

$$\frac{1}{\nu}\frac{\partial R(\mathbf{r},\hat{s},t)}{\partial t} = -\hat{s}\cdot\nabla R(\mathbf{r},\hat{s},t) - \mu_t R(\mathbf{r},\hat{s},t) + \mu_s H + R_o(\mathbf{r},\hat{s},t) \ , \tag{1.8}$$

where $\nu$ is the speed of light in the tissue determined by the relative refractive index $n$, $\mu_t = \mu_a + \mu_s$ is the extinction coefficient, $R_o(\mathbf{r},\hat{s},t)$ is the radiance of the light source, $H$ accounts for the scattering effect and is equal to:

$$H = \int_{4\pi} R(\mathbf{r},\hat{s},t)\Theta(\hat{s}'\cdot\hat{s})d\Omega',$$

and $\Theta(\hat{s}'\cdot\hat{s})$ is the phase function, representing the probability of light with propagation direction $\hat{s}'$ being scattered into a solid angle $d\Omega$ around $\hat{s}$. In an adult head the phase function does not depend only on the angle between the scattered $\hat{s}'$ and incident $\hat{s}$ directions (which is, $\Theta(\hat{s}'\cdot\hat{s}) \neq \Theta(\hat{s}\cdot\hat{s}')$ ) but is a function of the average of the cosine of the scattering angle $g$ (called the scattering anisotropy factor):

$$g = \int_{4\pi} (\hat{s}'\cdot\hat{s})\Theta(\hat{s}'\cdot\hat{s})d\Omega \ . \tag{1.9}$$

The scattering anisotropy factor $g$ is used in Monte Carlo simulations of photon migration to calculate the scattering angle within the particular voxel containing the scattering event (see the description of Monte Carlo below).

**1.1.2.1.3 Diffusion Approximation:** The Diffusion Approximation (DA) follows from the RTE when directional and temporal broadening is assumed [118, 63], or, in other words, when $\mu_a/\mu_s' << 1$, where $\mu_s'$ is the reduced or transport scattering coefficient (or reduced mean free path) which is defined as: $\mu_s' = \mu_s(1-g)$ and $g$

is defined in Equation 1.9; the inverse of $\mu_s'$ can be interpreted as "the distance a photon has to travel before it loses all information regarding its initial direction" [63]. Remembering that $\mu_a$ and $\mu_s$ are the inverse of the photon mean free path for absorption and scattering, the diffusion approximation means that the number of scattering events is assumed much smaller than the number of absorption events (which leads to assuming that radiance is nearly isotropic after numerous scattering events) and that time for substantial current density change is much longer than the time to traverse one transport mean free path. With the diffusion approximation the number of independent variables in the radiance expression at any spatial and temporal point are reduced with respect to the six of RTE ($x$, $y$ and $z$ from the position vector $\mathbf{r}$, polar and azimuthal angles from direction $\hat{s}$, and $t$), as radiance is considered largely isotropic and its spherical harmonics expansion ($Y_{n,m}$) is reduced to the isotropic and first-order anisotropic terms only [118]:

$$R(\mathbf{r},\hat{s},t) \approx \sum_{n=0}^{1}\sum_{m=-n}^{n} R_{n,m}(\mathbf{r},t)Y_{n,m}(\hat{s}) \ , \tag{1.10}$$

where $R_{n,m}$ are the expansion coefficients, the single isotropic term corresponds to $n = 0$ and the three anisotropic terms correspond to $n = 1$ and are written as follows:

$$R_{0,0}(\mathbf{r},t)Y_{0,0}(\hat{s}) = \frac{\Phi(\mathbf{r},t)}{4\pi} \tag{1.11}$$

and

$$\sum_{m=-1}^{1} R_{1,m}(\mathbf{r},t)Y_{1,m}(\hat{s}) = \frac{3}{4\pi}\vec{J}(\mathbf{r},t)\cdot\hat{s} \ , \tag{1.12}$$

and from Equations 1.10, 1.11 and 1.12 we derive an expression of the approximated radiance:

$$R(\mathbf{r},\hat{s},t) \approx \frac{\Phi(\mathbf{r},t)}{4\pi} + \frac{3}{4\pi}\vec{J}(\mathbf{r},t)\cdot\hat{s} \ . \tag{1.13}$$

When we substitute Equation 1.13 in Equation 1.8, integrate over the complete $4\pi$ solid angle, multiply by the direction $\hat{s}$ before evaluating and use the second assumption of diffusion theory (temporal broadening) we obtain the expression of diffusion equation (for more details see [118]):

$$\frac{1}{\nu}\frac{\partial\Phi(\mathbf{r},t)}{\partial t} + \mu_a\Phi(\mathbf{r},t) - \nabla\cdot(D\nabla\Phi(\mathbf{r},t)) = \Phi_o(\mathbf{r},t) \ , \tag{1.14}$$

where $D$ is the diffusion coefficient:

$$D = \frac{\varepsilon}{3(\mu_a(r)+\mu_s')}.$$

An important difference with RTE is that DA does not explicitly depend on the scattering coefficient $\mu_s$ but only on the reduced scattering coefficient, which means that diffusion is unaffected by the changes of the anisotropy of the scattering medium

if the reduced scattering coefficient stays constant.

**1.1.2.1.4 Monte Carlo simulation of the RTE:** Monte Carlo simulation of photon migration is an accurate solution of RTE although time consuming (typically $3x10^8$ photons are propagated within 10-15 hours on an Opteron computer cluster). The assumptions introduced on photon behavior with the Diffusion Equation 1.14 give rise to inaccuracies, especially for a photon beam incident on a medium of limited depth as the absorption coefficient $\mu_a$ increases and the scattering coefficient $\mu_s$ decreases within one transport mean free path of the location of the light source (where radiance is not yet isotropic). In order to simulate photon migration on the human head using Monte Carlo it is necessary to specify the head tissue types and their optical properties; the head model is typically described by a 3D volume of voxels (which are the 3D spatial unit) indexed with the label assigned to each tissue type. In Figure 1-2 we describe the Monte Carlo process as implemented by Boas at al. [16]: the parameters of the Monte Carlo photon migration simulator are compiled into a single configuration file which lists the optical properties (such as absorption and scattering coefficients, refractive index $n$ and scattering anisotropy factor $g$ for each specified tissue type), the simulation technical parameters (such as the number of injected photons, the direction of photon injection and detection, which is toward the AC point, the number of time steps and their length, the random seed) and the anatomical model parameters (such as the location and name of the segmented anatomical head model, the number and location of each source and detector and the voxel unit size). For each photon (or photon batch for increased computational speed) the photon trajectories through the head are simulated, taking into account the scattering events and the absorption factor to sample from a distribution the most likely photon direction and energy attenuation (or residual weight). Specifically, given the initial position and direction of the photon specified in the configuration file, (1) the length to the first scattering event is calculated from an exponential distribution; (2) then the photon weight is decreased by $\exp(-\mu_a L)$ and (3) the photon position is increased by $L$. At each step a new scattering angle is calculated using the probability distribution given by the Henyey-Greenstein phase function [119] and steps (1-3) are repeated until the photon exits the medium or has traveled longer than 10 ns (chosen because the probability of photon detection after 10 ns is exceedingly small). The probability of internal reflection is calculated when the photon reaches the outermost medium boundary and if reflection occurs, the photon migration continues back into the medium, otherwise the photon journey ends and a new photon is launched into the medium. The optical properties at the photon' current position are updated every space unit step (we typically use 1 mmvoxel as space unit) and the scattering angle is determined by the value of the scattering anisotropy factor $g$ of the voxel where the scattering event has occurred. The un-normalized photon fluence within the medium is calculated by accumulating the photon weight every 1 unit space in the voxel corresponding to the present position of the photon. After propagating all the photons throughout the medium, the photon fluence within the medium is calculated by normalizing the accumulated photon fluence $F(\mathbf{r})$ by accounting for the principle

of energy conservation: the exiting photon flux plus the number of photons absorbed in the medium must equal the number of simulated photons, which we normalize to 1 [16]; hence, we obtain the normalization factor for $F(\mathbf{r})$ from this relation:

$$\sum_{surf} \vec{J}_{out}(\mathbf{r}_j) A_j + \sum_{vol} F(\mathbf{r}_i) \mu_a(\mathbf{r}_i) V_{voxel} = 1 \ , \tag{1.15}$$

where $F(\mathbf{r}_i)\mu_a(\mathbf{r}_i)$ is the number of photons absorbed at a given point, $\vec{J}_{out}(\mathbf{r}_i)$ is the normalized exiting photon flux (which is, divided by the number of simulated photons), $\mathbf{r}_j$ and $\mathbf{r}_i$ are the surface and volume voxel position respectively, $V_{voxel}$ is the 3D volume and $A_j$ is the area of the surface element at position $\mathbf{r}_j$. The resulting normalized light intensity is described in Equation 1.19.

#### 1.1.2.2 Inverse problem

The DOT forward model essentially describes photon migration through an heterogeneous highly scattering biological tissue: we use an implementation [16] of Monte Carlo numerical simulation of photon propagation in a segmented adult head model (see the Monte Carlo description in the previous section for more details); this simulation yields the forward matrix $A$, where for each voxel $j$ and each source-detector pair $m$ (which forms the measurements' list) the sensitivity to absorption changes $A_{j,m}$ is recorded. For functional brain imaging, the changes in optical properties within the head volume are fairly small and thus changes in optical measurements can be linearly related to the local changes in absorption coefficient $\mu_a$ (assuming invariant scattering). Therefore, differential images are obtained using the Born approximation for absorption changes:

$$y = A\Delta x \ , \tag{1.16}$$

where the measurement vector $y$ is calculated as $y = \Delta\Phi/\Phi_o$, $\Delta\Phi$ is the change in the detected light intensity, $\Phi_o$ is the injected light intensity, $\Delta x$ is the vector indicating voxel-wise absorption perturbation, and an element of the imaging matrix $A$ is $A_{j,m}$, which is the spatial sensitivity to absorption changes in voxel $j$ as measured by source-detector pair $m$, is the sensitivity profile, otherwise known as the three-point Green's function, which is the convolution of the direct and adjoint two-point Green's functions [9, 70, 8]:

$$A_{j,m} = \sum_{t_m=t_o}^{T} \left( \frac{1}{G(\mathbf{r}_{S_m}, \mathbf{r}_{D_m}, t_m)} \int_{-\infty}^{+\infty} G(\mathbf{r}_{D_m}, \mathbf{r}_j, \tau) G(\mathbf{r}_j, \mathbf{r}_{S_m}, t_m - \tau) d\tau \right) \ , \tag{1.17}$$

where $G(\mathbf{r}_{S_m}, \mathbf{r}_{D_m}, t_m)$ is the time domain Green's function, which is the photon density distribution at time delay $t_m$ for source position $\mathbf{r}_{S_m}$ and detector position $\mathbf{r}_{D_m}$ involved in the $m^{th}$ measurement [9], $\mathbf{r}_j$ is the position of the $j^{th}$ voxel and time is summed over the initial time step $t_o$ and the maximum time delay $T$.

The inverse problem as stated in Equation 1.16 is ill posed, as there are fewer

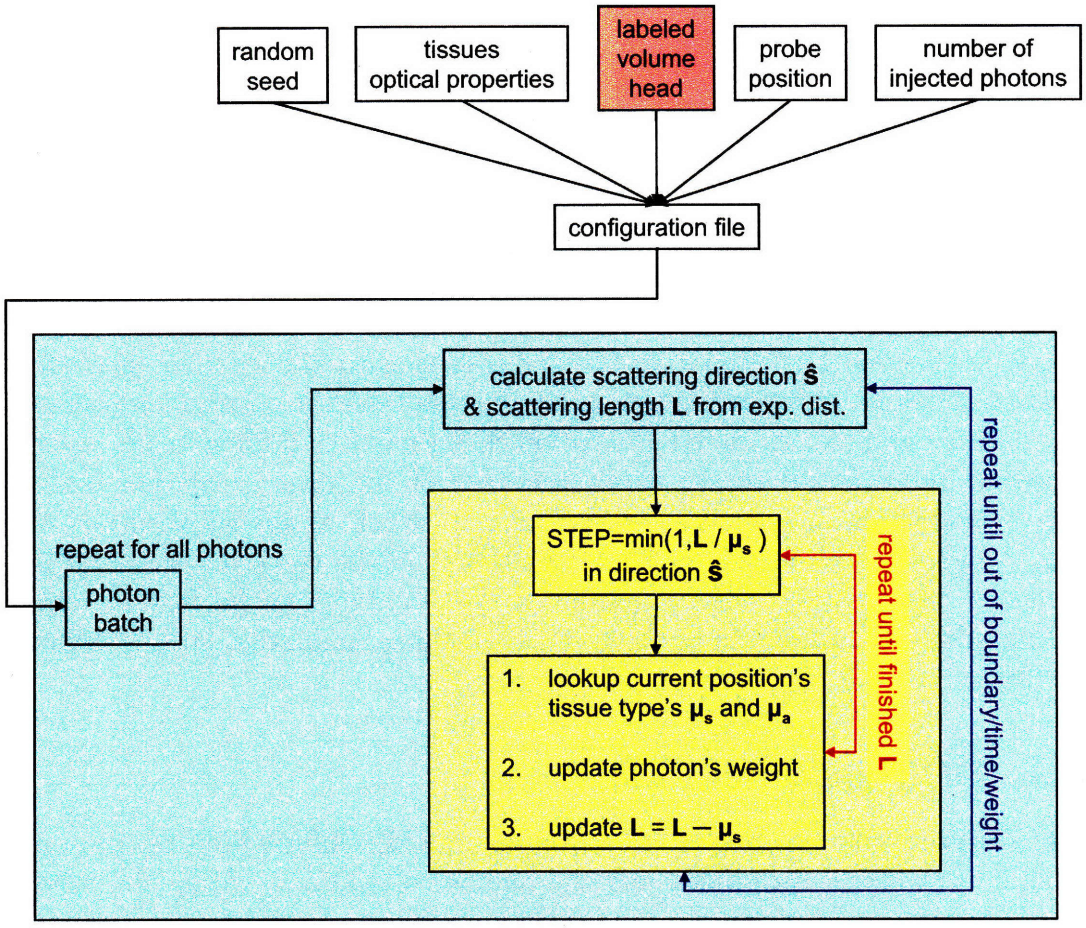


Figure 1-2: In order to simulate photon migration on the human head using Monte Carlo is necessary to specify the medium tissue types and their optical properties (purple box); the medium is typically described by a 3D volume of voxels (which are the 3D spatial unit) indexed with the label assigned to each tissue type. The configuration file lists the parameters of the Monte Carlo photon migration simulator; these parameters include the optical properties (such as absorption and scattering coefficients, refractive index $n$ and scattering anisotropy factor $g$ for each specified tissue type), the simulation technical parameters (such as the number of injected photons, the number of time steps and their length, the random seed) and the anatomical model parameters (such as the location and name of the segmented anatomical head model, the number and location of each source and detector and the voxel unit size). For each photon (or photon batch for increased computational speed) is simulated the photon most likely trajectory through the head, taking into account the scattering events and the absorption factor, iteratively updating the photon's energy attenuation (or residual weight).

measurements (size of $y$, typically less than a hundred) than unknowns (size of $\Delta x$, which is the number of voxels in the head volume, typically several thousands), and therefore the linear problem is underdetermined and its regularized solution can be expressed using the Moore-Penrose pseudoinverse [75]:

$$\hat{x} = A^T(AA^T - \alpha I)^{-1}y \ , \tag{1.18}$$

where $I$ is the identity matrix, $\alpha$ is the Tickonov regularization parameter [14], $y$ is the measurement vector from Equation 1.16, and $A$ is the sensitivity matrix from Equation 1.17. The solution of the inverse problem, $\hat{x}$, is a vector indicating the level of absorption perturbation in each voxel, which is key to calculating hemodynamic changes (see Section 1.1.1 Equation 1.3) and consequently the vascular effect of brain activation. Because only few photons probe further than the cortical surface, optical measurements and reconstructed absorption changes have a limited depth resolution. A possible improvement of the depth accuracy of the inverse solution $\hat{x}$ is given by the introduction of a cortical constraint [19], which means substituting $A$ with $A_{cortex}$, which is equal to the sensitivity matrix $A$ in the cortical voxels and is zero elsewhere. The depth resolution of the inverse solution can be further improved by using additional spatial priors from other imaging modalities, such as functional MRI [28].

### 1.1.3 DOT measurements

Monte Carlo simulation of photon migration provides information on the number of photons traversing each voxel and the number of photons exiting the head at a detector location or dispersing in air. This information is used to determine useful measurements such as the total light intensity collected at detector positions, the photon's mean distance traveled through a tissue or region of interest (called Partial Path Length), and the photon's mean distance traveled through the medium sub-regions normalized by the source-detector distance (called Partial Pathlength Factor).

#### 1.1.3.1 Detected light intensity in time-domain and continuous wave

From the simulated photon propagation in a medium, light intensity (or fluence rate) in Time Domain (TD – DOT) is calculated as follows (see Equation (2) from [16]):

$$\Phi_j(t_i) = \frac{1}{N_j(t_i)\Delta t} \sum_{l=1}^{N_j(t_i)} \prod_{m=1}^{N_R} \exp(-\mu_{a,m} L_{j,l,m}) \ , \tag{1.19}$$

where $\Phi_j(t_i)$ is the measured photon fluence rate at detector $j$, $N_j(t_i)$ is the number of injected photons collected at detector $j$ in a time-gate of width $\Delta t$ centered at time $t_i$, $\exp(-\mu_{a,m} L_{j,l,m})$ accounts for the effects of absorption in each region where $L_{j,l,m}$ is the pathlength of photon $l$ through region $m$, and the photon migration time is related to the photon pathlength by the speed of light in the medium. $N_R$ is the number of regions through which the photons migrate. The Continuous Wave (CW)

fluence is calculated by summing $\Phi_j(t_i)$ over time index $i$.

#### 1.1.3.2 Partial Path-Length - PPL

Tissue scattering causes the photons to travel a greater distance than the geometric distance between the source and detector. The partial pathlength of light through each of the tissue types $m$ is defined [115, 96, 54, 99] using the modified Beer-Lambert Law to obtain the change in the absorption coefficient from the change in the intensity of the detected light $\Delta$OD through the tissue:

$$\Delta \text{OD} = \Delta \ln(\frac{\Phi_o}{\Phi}) \ , \tag{1.20}$$

where $\Phi_o$ is the intensity of the incident light, $\Phi$ is the intensity of the detected light as given by Equation 1.19. The expression of the mean optical path length is given by:

$$\text{PPL}_{i,j,m} = \partial \text{OD} / \partial \mu_{a,m} \ , \tag{1.21}$$

where $\text{PPL}_{i,j,m}$ is the pathlength photons injected from source $i$ and escaped from the medium at detector location $j$ have traveled in tissue type $m$. Therefore, when substituting the light intensity expression from Equation 1.19 and taking the derivative with respect to small changes in $\mu_a$, we obtain:

$$\text{PPL}_{j,m} = \frac{\sum_{l=1}^{N_j(t_i)} \prod_{m=1}^{N_R} L_{j,l,m} \exp(-\mu_{a,m} L_{j,l,m})}{\sum_{l=1}^{N_j(t_i)} \prod_{m=1}^{N_R} \exp(-\mu_{a,m} L_{j,l,m})} \ . \tag{1.22}$$

#### 1.1.3.3 Partial Path-length Factor - PPF

A dimensionless factor, the Partial Path length Factor PPF, has been frequently used in optical imaging studies and is derived from Equation 1.19:

$$\text{PPF}_{i,j,m} = \frac{\text{PPL}_{i,j,m}}{d} \ , \tag{1.23}$$

where $d$ is the distance between source $i$ and detector $j$ and $m$ is the tissue type or region of interest we are calculating the partial pathlength factor of.

### 1.1.4 DOT work flow

After describing the neuro-vascular effects of brain activation (Section 1.1.1) and the physics of the optical imaging process measuring it (Section 1.1.2), we proceed outlining our actual implementation of optical tomography (see Figure 1-3):

**input:** we compile the set of required input for the Monte Carlo simulation of photon migration into a configuration file [16], including the subject's anatomical head segmented into 3 to 5 tissue types (see each chapter for specific implementations) and the coordinates of the sources and detectors constituting the optical probe; when simulating photon migration on a virtual subject (which is, a subject not

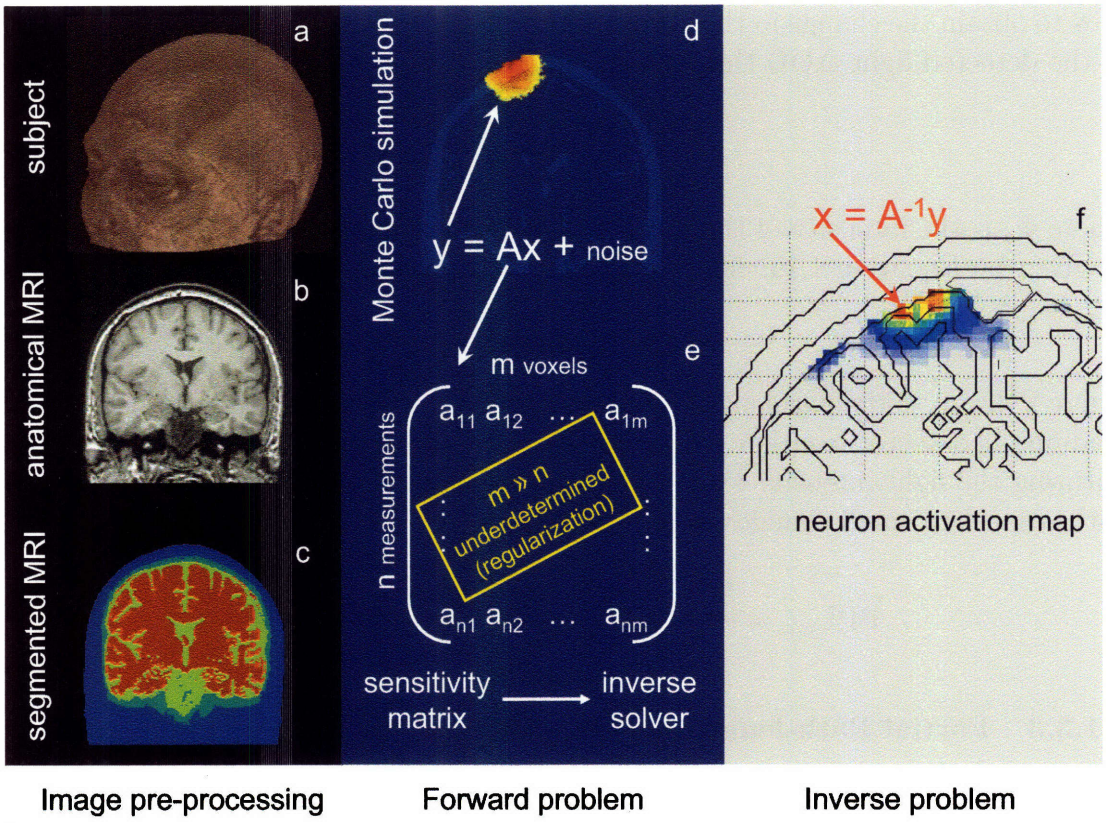


Figure 1-3: The stages of Diffuse Optical Tomography are divided in three parts: on the left box (black background) the image pre-processing, which includes the acquisition of the physical or virtual subject's (a) anatomical model (b) then segmented into various tissue types (c); in the middle (blue background) is outlined the DOT forward model steps, including the simulation of photon migration using Monte Carlo (d), which gives rise to the sensitivity matrix $A$ (e) used in the linear model $y = Ax +$ noise, and inverted to calculate brain activation (f). In fact, $A$ can not be simply inverted because the problem is underdetermined and therefore regularization is needed (see Section 1.1.2.2).

physically available but of whom we have the anatomical MRI), we can design the optical probe as we see fit and virtually place it on the scalp, whereas, when we are designing an experiment on a physical subject, we acquire the subject's specific anatomical MR while marking the locations of the physical probe on the subject's head so that the optodes positions are visible on the MR scan and can subsequently be listed on the configuration file;

**forward model steps:** in the head model input of the Monte Carlo simulation, particular care is given to an accurate segmentation of the Cerebral Spinal Fluid (CSF) layer because optical measurements are sensitive to its thickness (see Chapter 2). We designed an algorithm to further improve CSF segmentation using MR intensity thresholding combined with anatomical constraints (see Section 2.3.2.1 for details). The Monte Carlo simulation is performed for each source and for each one of the two selected wavelengths (see Section 1.1.1); only one wavelength is used when we are only interested in the forward model solution;

**forward model output:** as described in details in Section 1.1.2.2, the Monte Carlo simulation yields to: (1) the sensitivity matrix $A$, calculated as the three-point Green's function (see Equation 1.17) and representing the spatial sensitivity to absorption changes at each voxel for each source-detector pair, (2) the detected light intensity (see Equation 1.19) in time-domain and continuous wave, and (3) a region-wise measure of sensitivity to absorption changes, which is the Partial Path Length (PPL) (see Equation 1.21), derived from the light intensity. The PPL and light intensity $\Phi$ are used to quantitatively and qualitatively validate hypothesis on the forward model respectively, whereas the imaging matrix $A$ is used to solve the inverse problem and calculate neuronal activation;

**inverse problem steps:** when interested in validating hypothesis on brain functional data, we need to solve the DOT inverse problem, or, in other words, we need to obtain the absorption perturbation vector $\Delta x$ from the optical measurements $y$ via the sensitivity matrix $A$ calculated in the DOT forward model. The inverse solver can be applied to experimental data (actual optical measurements acquired on a physical subject) or simulated measurements (perturbation vector designed ad hoc to simulate activation on the regions of choice). In the latter case, white gaussian noise $w$ is added to the forward model in order to simulate the optical measurements ($y = A\Delta x + w$);

**inverse problem output:** the regularized and cortically constrained solution of the inverse problem (see Section 1.1.2.2) is the perturbation vector $\Delta x$, which is zero for non-active voxels and non-zero for voxels with increased or decreased absorption coefficient due to the localized changes in tissue oxygenation. Using two different wavelengths, we can obtain the level of oxy- and deoxy-hemoglobin by applying Equation 1.3 to the perturbation vectors $\Delta x_{\lambda_1}$ and $\Delta x_{\lambda_2}$ and thus calculate the hemodynamic response to local neuron activity with $\approx 1$ cm spatial resolution and better than 1 ns temporal resolution.

## 1.2 Thesis outline

This work aims at improving Diffuse Optical Tomography (DOT) by offering new strategies for a more accurate, efficient, and faster image processor. Specifically, after investigating the influence of Cerebral Spinal Fluid (CSF) properties over the optical measurements (Chapter 2), we propose using a realistic segmented head model that includes a novel CSF segmentation approach for a more accurate solution of the DOT forward problem. Moreover, in Chapter 3, we outline the benefits and applicability of a Diffusion Approximation-based faster forward model solver such as the one proposed by Barnett et al. [13]. In Chapter 4 we describe a new registration algorithm based on superficial landmarks which is an essential tool for the purely optical tomographic image process proposed in Chapter 5. A purely optical tomography of the brain during neural activity will greatly enhance DOT applicability and have many advantages, in the sense that the DOT low cost, portability and non-invasiveness would be fully exploited without the compromises due to the MRI role in the DOT forward image process.

### 1.2.1 Cerebral Spinal Fluid study

Studying the effect of Cerebral Spinal Fluid (CSF) measurements of brain activity has never been done before because CSF does not affect significantly other functional imaging technologies (such as fMRI) and because investigating CSF-induced effects requires having access to its accurate anatomical model, which is difficult to obtain as its MR intensity range is not unique. Our contributions in this field include the design and testing of a semi-supervised segmentation algorithm tailored to accurately identify CSF and bone from T1 weighted multi-flip angle anatomical MRIs (see Section 2.3.2.1). Moreover, we investigate the impact of CSF scattering coefficient ($\mu_s'$) on DOT forward model as it greatly affects optical measurements (see Section 2.1). We successfully validated the hypothesis that varying CSF $\mu_s'$ from zero up to the order of the typical CSF inverse line-of-sight distance, or about 0.3 $mm^{-1}$, does not affect significantly sensitivity to absorption changes in the brain; this hypothesis is key for applying the diffusion equation (and hence its more computational time efficient analytical solvers) instead of the radiative transit equation to describe photon migration in the human head (see Chapter 3). Furthermore, we study the effect of CSF thickness on DOT measurements (see Section 2.2) and find that a 50% change in CSF thickness produces small errors (less than 15% for source-detector separation $< 32$ mm). Consequent to these findings, we investigate the variability of CSF thickness across population (see Section 2.3) hoping to find a link between personal data (such as gender and age) and CSF thickness, which would lead to the possibility of customizing a generalized anatomical head model (atlas) to replace a specific subject anatomy in the DOT forward model (see Chapter 5). Our results show that CSF thickness is highly correlated with age (p value $< 0.005$), whereas gender has no bearing on CSF thickness. Our collective studies yield these conclusions and main contributions:

1. we provided evidence validating the hypothesis that CSF scattering coefficient

can be approximated at $\sim 0.3$ mm$^{-1}$with errors less than 20% in time-domain and continuous wave; consequently, diffusion approximation based solutions of DOT forward problem can be used, greatly improving the computational run time (from $\sim$ 12 hours to few minutes);

2. we designed a novel CSF/bone accurate segmentor that can be used to model human head's tissue types for the EEG, MEG and DOT forward problems;

3. we investigated the age and gender relationship with CSF thickness and found that only age is highly correlated with CSF; this results lead to a linear model of age versus CSF thickness that can be used to customize a general anatomical model of the human head to represent the subject's specific in order to achieve a purely optical tomographic image process;

4. our more accurate CSF segmentor enables us to perform longitudinal studies of CSF thickness to investigate neurodegeneration and test the efficacy of various treatments as done in cortical thickness studies [31, 73, 4, 50, 58, 37, 107, 78, 117, 61, 20, 79, 124, 123, 104, 83].

### 1.2.2 Faster forward problem solver

An accurate photon migration model is key for a reliable solution of the DOT inverse problem that leads to brain activation maps. The most accurate mathematical model describing photon migration is the Radiative Transfer Equation (RTE), but unfortunately an analytical solution of the RTE is not known and therefore the RTE is solved numerically by using accurate but computationally expensive Monte Carlo based algorithms. In Chapter 3 we investigate the applicability of a faster alternative to a Monte Carlo numerical solution of the RTE (see Equation 1.8) based on the Diffusion Approximation (DA) (see Equation 1.14). For validation purposes, we compare the performances of the Monte Carlo (MC) simulator proposed by Boas et al. [16] with these of the Finite Difference (FD) algorithm presented by Barnett at al. [13] that solves Diffusion Approximation analytically. Our results show that the Finite Difference approach to the diffusion equation offers greater computational efficiency, but at the cost of modeling accuracy: in particular partial pathlength within the brain measured in continuous-wave using FD introduces an error between 20% and 40% with respect to the pathlength predicted by MC. The time-resolved data are more encouraging, though, suggesting that a Time Domain DOT instrument can succesfully take advantage of a more efficient solution of the Diffusion Approximation of photon migration as long as the first few data points are discarded and the separation between source and detectors is sufficient to probe the brain (errors less than 12% at source-detector distances over 28 mmand after 1.4 ns). Therefore, we conclude that diffusion based methods can well predict photon scattering through the human head provided that a realistic head model is used and the probe is designed to maximize Contrast to Noise Ratio (CNR) in the brain.

### 1.2.3 Non-volumetric registration

In Chapter 4, we describe a novel method, $SLR_{10\text{-}20}$, to register a general head model to a specific subject's head based on alignment of superficial landmarks (the EEG 10-20 electrodes system) and we validate it against the subject's anatomical MRI (our ground truth) and against the commonly used volumetric affine registration method available in the Statistical Parametric Mapping (SPM5) toolbox [3]. We analyze a dataset of 32 healthy subjects' MRIs and the MNI single subject atlas (see Section 4.2.1); we describe the superficial landmarks system adopted (the EEG 10-20 international system) and how it is used to estimate the affine transformation matrix (see Section 4.2.3 and the virtual 10-20 algorithm designed by Jurcak et al. [76]); then we present several validation metrics: (1) we compare the surface meshes/volumes of the subjects normalized to the atlas using SPM5 and $SLR_{10\text{-}20}$; (2) we compare the two registration algorithms' performances in surface landmarks preservation, (3) in cortical depth preservation, and (4) CSF thickness preservation; finally, (5) we test our registration algorithm for the preservation of cortical landmarks against "ground truth" (which is, the location of the same landmarks on the un-registered subjects).

Overall, $SLR_{10\text{-}20}$ performs better than SPM5 in preserving mesh, volumes and superficial landmarks; its accuracy in mapping cortical landmarks is not worse than the intrinsic variability of macroanatomical and cytoarchitettonical structures across subjects [40] (see Table B.3), suggesting that $SLR_{10\text{-}20}$ is well suited to register to a specific subject's head a general anatomical head model which is then used to guide DOT forward problem without the intervention of MRI (see Chapter 5).

Furthermore, our non-volumetric registration algorithm can be used for longitudinal EEG and MEG studies when an anatomical MR of the subject is not advisable or available; the locations of the 10-20 points are acquired in most EEG studies, making the application of $SLR_{10\text{-}20}$ particularly suitable.

From the validation of $SLR_{10\text{-}20}$ we can also observe that, since affine registrations preserve relative distances, the cortical depth measurements in MNI space (see Figure 4-8) agree with the observations reported for the CSF population study (see Figure 2-16), that is, decrease of cortical thickness and consequently increase of CSF thickness are effects of normal aging [31, 73, 108] as well as neurodegeneration due to various diseases [4, 50, 58, 37, 107, 78, 117, 61, 20, 79, 124, 123, 104, 83]; therefore, studying cortical thickness can be another non-invasive effective way to investigate neurodegeneration and its treatment.

### 1.2.4 Purely optical tomography

In Diffuse Optical Imaging of brain activity a 3D MRI-based subject anatomical model is used to simulate light propagation in highly scattering tissues. However, an MRI scan is expensive and might not always be available for particular subjects or might not be feasible in certain situations (for example, for claustrophobic subjects).

Currently the most successful method of solving the DOT inverse problem is to use subject-specific anatomical information which is derived from an MR anatomical scan.

In Chapter 5 we describe an imaging protocol that uses solely Diffuse Optical Tomography to reconstruct brain activation. The approach consists of using an atlas-based anatomical model instead of the subject's anatomy and simulating photon migration on the atlas model (DOT forward model) while acquiring optical measurements from the subject, and then reconstructing the location of cortical activation (by solving the DOT inverse problem). The benefits of this novel method comes from the elimination of the need for MRI, and its associated issues (such as high costs, possible subject's discomfort and claustrophobia during the MR anatomical scan, prohibiting studies on neonatal subjects, lack of portability).

We first present a preliminary study using one single subject registered to an atlas using MRI-based registration (Section 5.1). We validate our claim that an atlas can be a suitable substitute to the subject specific anatomical model by comparing the simulated optical measurements obtained using the subject specific anatomical model versus the generic adult human head model. The most relevant measurement, the partial pathlength within the brain, indicates that such anatomical approximation can be used without introducing a significant error (relative error $\leq 10\%$), provided that a suitable atlas is selected.

The preliminary study is limited by the size of the dataset (one subject and one atlas) and by the use of a registration algorithm that still needs MR anatomical information. The natural development of the idea of using a general anatomical model in place of the subject specific is described in Section 5.2. Using a dataset of 31 healthy human subjects, we measure sensitivity to absorption changes (solution of the forward model) on a chosen set of 24 functional Region Of Interests (ROIs) and compare the results obtained using the registered atlas versus these calculated using the true subject's anatomical model on a dataset of 31 healthy subjects. The new registration algorithm, based on superficial landmarks, is described in Chapter 4. The registered atlas' CSF thickness is modified according to the subject's age the atlas is registered to, following up the study of Chapter 2. Moreover, we solve DOT forward and inverse problem on three experimental subjects: optical measurements are acquired on the physical subjects and photon migration is simulated on both the subjects' heads and on the atlases registered to the experimental subjects using $SLR_{10\text{-}20}$; the inverse problem is solved using the subject's data and the reconstructed activation map is compared to that calculated guiding DOT forward model with the registered atlas: the qualitative results (see Figures 5-19 and 5-20) show that the activation focus is localized in the correct gyri using the atlas model, although the subject and atlas cortical geometry is not exactly the same and the activation level of contrast is different. Overall, we demonstrate that is possible to use a general anatomical model to represent a subject's to guide DOT forward model to localize the macroanatomical structure of activation.

# Chapter 2

# Cerebral Spinal Fluid modeling

We investigate the effect of Cerebral Spinal Fluid (CSF) in optical tomography; in particular we focus on the impact of CSF scattering coefficient and CSF thickness on the DOT forward model as these are the two parameters to which DOT is most susceptible. To the best of our knowledge, CSF model analysis has never been done before, mostly because CSF does not affect significantly most functional imaging technologies (such as fMRI and PET), but also because investigating the CSF layer requires having access to its accurate anatomical model, which is difficult to obtain. We are interested in studying the CSF scattering coefficient, $\mu_s'$, to validate the hypothesis that varying $\mu_s'$ within a certain range (as a function of CSF thickness) will not affect optical measurements; this hypothesis is essential to apply the diffusion equation (and hence its more computational time efficient analytical solvers) instead of the transfer equation to describe photon migration (which is the DOT forward model). On the other hand, we first study the effect of CSF thickness on DOT measurements, then we investigate the variability of CSF thickness across populations hoping to find a link between personal data, such as age and gender, and CSF thickness, which would lead to the possibility of customizing a generalized anatomical head model (atlas) to replace a specific subject anatomy in the DOT forward model.

## 2.1 Effective scattering coefficient

Efficient computation of the time-dependent forward solution for photon transport in a head model is a key capability for performing accurate reconstruction for functional Diffuse Optical Tomography (DOT) of the brain. The diffusion approximation to photon transport is much faster to simulate than the physically-correct radiative transfer equation (RTE), however, it is commonly assumed that scattering lengths must be much smaller than all system dimensions and all absorption lengths for the approximation to be accurate. Neither of these conditions is satisfied in the Cerebro Spinal Fluid (CSF). Since line-of-sight distances in the CSF are small, of the order a few mm, we explore the idea that the CSF scattering coefficient may be modeled by any value from zero up to the order of the typical inverse line-of-sight distance, or about 0.3 $mm^{-1}$, without significantly altering calculated detector signals or partial

pathlengths relevant for functional measurements. We demonstrate this in detail using Monte Carlo simulation of the RTE in a three-dimensional head model based on clinical MRI data, with realistic optode geometries. Our findings lead us to expect that the diffusion approximation will be valid even in the presence of the CSF, with consequences for faster solution of the DOT forward problem.

The advantages of the use of the anatomical MRI of the human head have been shown for a spatially constrained iterative reconstruction process that greatly improves the depth resolution of the measured optical properties [19] as well as for improving quantitative functional imaging [19, 17]. In this work we use Monte Carlo (MC) modeling, which implements the transport equation [119, 16], to accurately simulate light propagation through an anatomically accurate MRI-based 3D model of the human head. We simulated both time-resolved and continuous wave measurements to validate our hypothesis of an effective CSF scattering coefficient by measuring the error introduced when using a CSF scattering coefficient larger than a near zero value (we use the reference CSF scattering coefficient of 0.001 $mm^{-1}$). Given this new larger effective $\mu_s'$, the conditions for validity of the diffusion approximation may hold to a much greater degree than previously thought, allowing accurate diffusion solution.

We calculate the deviation from our reference measurements of the photon fluence detected on the surface of the head and of the sensitivity to the brain. The results presented in this paper support our hypothesis that non-scattering CSF region can be treated with a larger scattering coefficient (0.3 $mm^{-1}$) with only 20% difference in the measurements. This result will also have relevance for the debate on the exact CSF scattering coefficient, since it demonstrates that as long as it is less than the inverse typical line-of-sight distances, its exact value is not relevant. Thus, it is in principle possible that the diffusion equation may provide sufficiently accurate modeling of photon migration through the human head, greatly reducing computational expense.

### 2.1.1 Head model and probe placement

We use MRI segmented data to determine the head geometry that we employ in the study. With this adult head model we can specify up to five tissue types (scalp, skull, CSF, gray and white matter, see Figure 2-1), though for this particular study we use only three (as described in Table 2.1). The whole volume is voxelized in a cube with 128 voxels per side ($128^3$ voxel in total, 2x2x2 $mm^3$each).

Table 2.1: CSF scattering study's optical properties

| Tissue type | $\mu_a$ [$mm^{-1}$] | $\mu_s$ [$mm^{-1}$] | Tissue thickness [mm] |
|---|---|---|---|
| scalp and skull | 0.019 | 0.86 | 3-8 (scalp) 7-8 (skull) |
| CSF | 0.004 | 0.001, 0.01, 0.1<br>0.2, 0.3, 0.7, 1.0 | 2-4 |
| brain | 0.01 | 1.11 | 4-10 (gray) > 40 (white) |

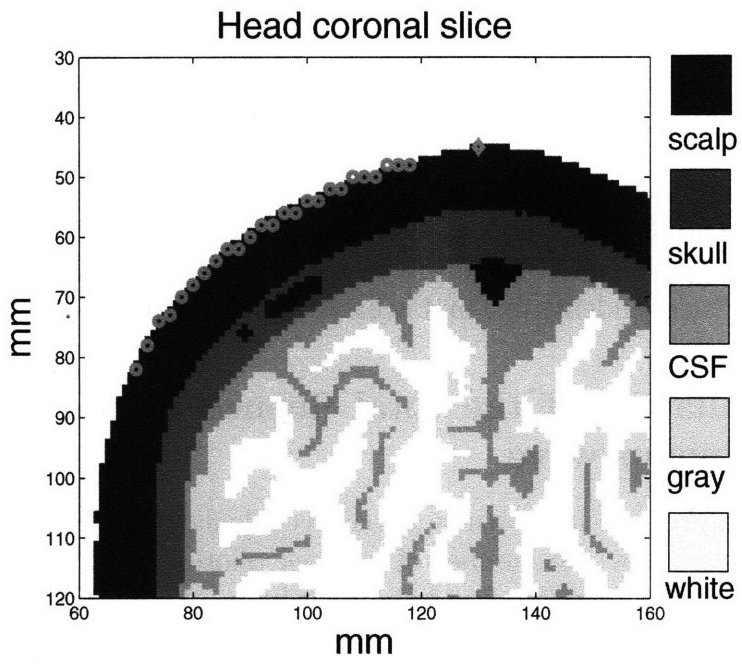


Figure 2-1: Head geometry and probe placement. The gray diamond on the top of the head indicates the position of the single source and the gray circles show the position of the twenty five detectors, equally spaced 2 mmapart from each other, starting at 12 mmfrom the source.

### 2.1.2 Optical properties

CSF is characterized by low scattering and absorption coefficients ($\mu_s'$ ~0.001 mm$^{-1}$ and $\mu_a$ ~0.004 mm$^{-1}$, which is typical of transparent tissues). We mostly use a higher scattering coefficient for CSF because we believe that $\mu_s'$ can be modeled as an inverse of the average CSF layer thickness [13]. Therefore, in our model we calculate CSF $\mu_s' = 1/\text{thickness}_{\text{CSF}}$, which gives us a $\mu_s'$ of ~0.25 mm$^{-1}$. Interestingly, the latest papers from Okada's group [54] also use a $\mu_s'$ of 0.25 mm$^{-1}$ for the CSF.

For the purpose of this study, we use a linear probe (see Figure 2-1), in which the sources and detectors are positioned along a line on the surface of the head, all placed in the same coronal slice. The probe features a single source (the gray diamond in Figure 2-1) and 25 detectors placed at 12, 14, 16, 18 , 60 mmfrom the source position (the gray circles in Figure 2-1). We chose this particular arrangement of optodes to analyze the effect of the CSF scattering coefficient on the measured photon fluence as a function of the separation between the source and the detector. Furthermore, the same probe has been used in similar studies by Okada et al. [98].

### 2.1.3 Solution of Transport Equation

Monte Carlo is a simple method that offers a great deal of freedom in defining geometries and optical properties based on the radiative transfer equation [119, 16].

The method models photon trajectories through heterogeneous tissues, reproducing the randomness of each scattering event in a stochastic fashion (a random seed is employed). When a photon is detected, its partial optical path length for each of the tissue types through which it passed are recorded in a history file. Monte Carlo methods have the disadvantage of being computationally expensive to obtain a decent signal to noise ratio (SNR) in highly scattering thick tissues. We run 11 independent Monte Carlo simulations of $10^8$ photons so that we can calculate the standard deviation across the independent runs and achieve an appropriate SNR.

### 2.1.4 Calculation of the total fluence in time domain and continuous wave

The detected fluence rate in the time domain is calculated by normalizing the propagated light intensity by the number of injected photons (see Equation 1.19). The propagated photons' energy is a function of $\exp(-\mu_{a,m}L_{j,l,m})$; the exponential factor describes how rapidly light is absorbed in highly scattering biological tissues. The fluence rate expression is described in Equation 1.19.

The resultant intensity $\Phi_{i,j,k}$ is a 3-dimensional matrix. The first dimension $i$ is the time index, the second $j$ is the detector index, and the third $k$ is the Monte Carlo run index. In order to increase the SNR, the $k$ independent Monte Carlo simulations are averaged. By summing over time the light intensity (Equation 1.19), we obtain the expression of the fluence in continuous-wave:

$$\Phi_j = \sum_{t_i} \left( \frac{1}{N_j(t_i)\Delta t} \sum_{l=1}^{N_j(t_i)} \prod_{m=1}^{N_R} \exp(-\mu_{a,m}L_{j,l,m}) \right) . \tag{2.1}$$

### 2.1.5 Calculation of Partial optical Path Length (PPL) and relative sensitivity

The partial path length is the distance light traveled through a region or tissue $m$ and is a function of the optical density OD (see Equations 1.21 and 1.20). As a reminder, the optical density is expressed as:

$$\partial \mathrm{OD}/\partial \mu_{a,m} \approx < L_m > . \tag{2.2}$$

where $\mathrm{OD} = \ln(\Phi_o/\Phi)$ and where $\Phi$ is given by Equation 1.19 and $\Phi_o$ is the incident number of photons. The partial path length factor is $L_m$, which is the fraction of the path that is in tissue $m$.

We calculate the relative sensitivity to absorption changes by calculating the partial optical pathlength error with respect to the most accurate measurement, which is the one calculated with CSF scattering coefficient equal to 0.001 $\mathrm{mm}^{-1}$. In other words, we calculate how well we can approximate the measurement obtained using CSF zero-scattering with a higher CSF scattering value. A small approximation er-

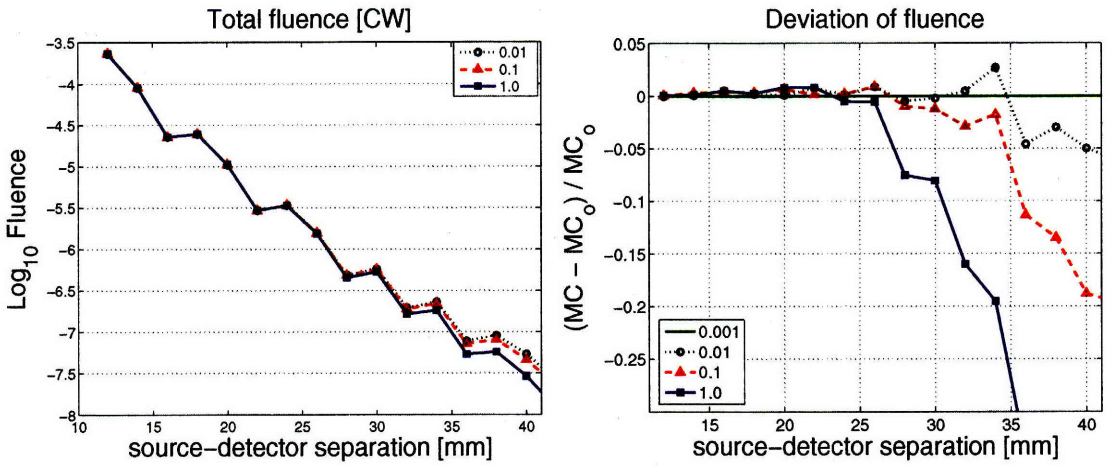


(a) (b)

Figure 2-2: (a) Total detected fluence simulated with Monte Carlo in continuous wave. (b) Relative fluence in continuous wave calculated with respect to $MC_o$, which is the Monte Carlo prediction when $\mu'_{s,CSF} = 0.001$ mm$^{-1}$.

ror due to the use of an effective CSF scattering coefficient will enable modeling photon migration with Diffusion Approximation which can be solved analytically by time-efficient algorithms (see Chapter 3).

## 2.1.6 Results

### 2.1.6.1 Fluence and partial pathlength for continuous wave

In Figure 2-2 we show the total measured fluence versus source-detector separation for different $\mu'_{s,CSF}$ (Figure 2-2a) and the fractional difference relative to $\mu'_{s,CSF} = 0.001$ mm$^{-1}$ (Figure 2-2b). The total fluence is normalized by the incident fluence, i.e. the total number of photons launched in the Monte Carlo simulation. We see that the detected fluence varies little when the $\mu'_{s,CSF} \leq 0.1$ mm$^{-1}$ but that a significant difference occurs for separations greater than 25 mm. In Figure 2-2b we see that at small separations (12-22 mm) the fractional difference for increasing $\mu'_{s,CSF}$ is less than 2%, becoming significant ($> 20\%$) at larger separations ($> 32$ mm) when $\mu'_{s,CSF}$ is 1.0 mm$^{-1}$. This is to be expected because smaller separations are predominantly sensitive to scalp-skull and therefore do not probe the CSF layer.

In Figure 2-3a we show the continuous-wave partial pathlength for the scalp-skull region and the brain region versus the source detector separation for different scattering coefficients in the CSF region. The results show that the sensitivity of the measurement to absorption changes does not change as $\mu'_s$ in the CSF space increases from 0.01 to 0.1 mm$^{-1}$, but that a change is observed with $\mu'_s = 1.0$ mm$^{-1}$. This is consistent with the hypothesis that the sensitivity will change as the scattering length becomes smaller than the typical line of sight distance through the CSF, which is approximately 3 mm in our model.

In Figure 2-3b,c we plot the fractional difference in the partial pathlength for the scalp-skull region and the brain region relative to that when $\mu'_{s,CSF} = 0.001$ mm$^{-1}$. In Figure 2-3b we observe a difference greater than 3% at larger separations (> 30 mm) for a CSF model with $\mu'_s = 1.0$ mm$^{-1}$, and a difference less than 1% for $\mu'_{s,CSF} = 0.1$ and 0.01 mm$^{-1}$. Figure 2-3c shows the same fractional difference observed in the brain. In the brain, even at small separations we observe a large difference only when $\mu'_{s,CSF} = 1.0$ mm$^{-1}$, increasing from 20% to 47% as the separation increases. For the smaller $\mu'_{s,CSF}$ we observe differences less than 10% at all separations.

To investigate the variation in more detail, we plot in Figure 2-4a-b the deviation in detected photon fluence at the surface of the scalp (Figure 2-4a) and the deviation in the partial pathlength in the scalp-skull and brain (Figure 2-4b) versus $\mu'_s$ of the CSF at source-detector separations of 20, 30, and 40 mm. These results show that a change greater than 20% is not observed until $\mu'_s > 0.3$ mm$^{-1}$, except at 40 mm separation. We believe that the large discrepancy observed at 40 mm is due to the weak signal reaching far detectors. These results support our hypothesis that we can treat this void-like region with a larger scattering coefficient ($0.1 < \mu'_s < 0.3$ mm$^{-1}$) and obtain similar results (errors between 10 and 20 % for CW measurements with source-detector spacing of < 40 mm).

We also note from Figs. 2-3a and 2-4b that the brain PPL, which corresponds to sensitivity of the CW measurement to absorption changes in the brain, is higher when CSF $\mu'_s$ is low, than when CSF $\mu'_s$ matches that of the brain.

#### 2.1.6.2 Fluence and Partial pathlength in the Time Domain (TD - DOT)

We further explore this result for time resolved photon migration. In Figure 2-5a we show how the partial pathlength varies with photon transit time in the medium. These results confirm what we have seen in continuous wave: the time resolved fluence is approximately the same when $\mu'_{s,CSF}$ is less than 0.1 mm$^{-1}$ but a significant difference is observed for a larger scattering coefficient. In Figure 2-5b we quantify this change relative to the fluence when $\mu'_{s,CSF} = 0.001$ mm$^{-1}$ and observe a greater than 50% deviation for $\mu'_{s,CSF} = 1.0$ mm$^{-1}$ and mostly less than 8% deviation when $\mu'_{s,CSF} = 0.1$ and 0.01 mm$^{-1}$.

In Figure 2-6 we explore how the CSF scattering coefficient affects the partial pathlength in the superficial layers and the brain versus time delay. The absolute partial pathlength in Figure 2-6a shows that no difference is observed for $\mu'_{s,CSF} = 0.1$ and 0.01 mm$^{-1}$ but that a difference is observed when $\mu'_s$ is increased further to 1.0 mm$^{-1}$. The deviation with increasing $\mu'_{s,CSF}$ relative to a $\mu'_{s,CSF}$ of 0.001 mm$^{-1}$ is shown in fig. 2-6b and 2-6c for the superficial and brain regions respectively. Little deviation is observed in the superficial scalp-skull region as the deviation is never larger than 15%. A more significant difference is observed for the brain, where the partial pathlength is underestimated by 20% to 50% for $\mu'_{s,CSF} = 1.0$ mm$^{-1}$ whereas the error is less

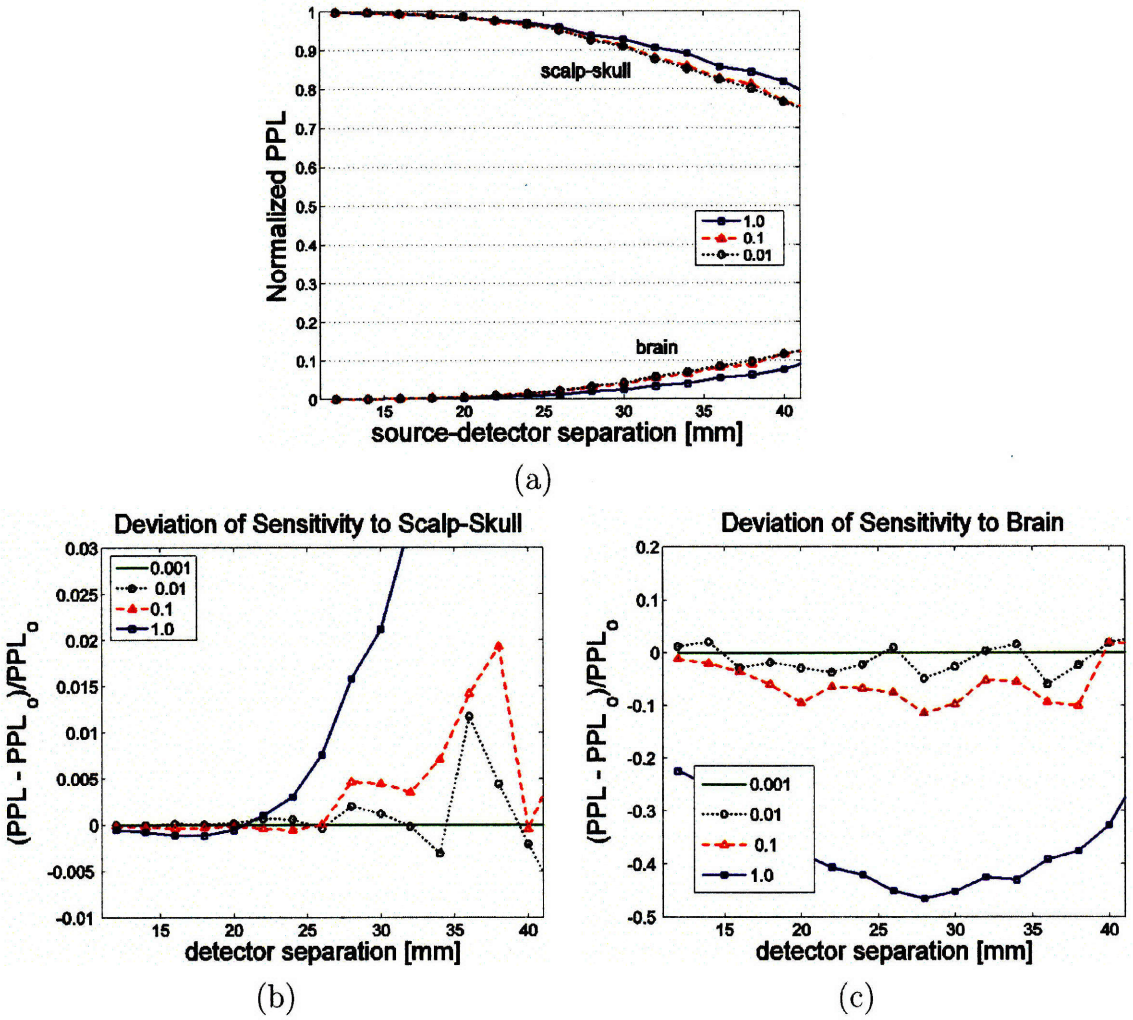


Figure 2-3: (a) Monte Carlo normalized pathlength calculated versus separation for three different $\mu'_{s,CSF}$: 0.01, 0.1 and 1.0 mm$^{-1}$ in continuous wave. The PPL is normalized by the total sensitivity to all tissue types. (b) Monte Carlo measure of relative sensitivity to scalp-skull layer versus separation when varying $\mu'_{s,CSF}$ in continuous wave ($\mu'_s = 0.01$, 0.1 and 1.0 mm$^{-1}$). The error is calculated with respect to PPL$_o$, which is the Monte Carlo prediction of PPL when $\mu'_{s,CSF} = 0.001$ mm$^{-1}$. (c) Monte Carlo measure of relative sensitivity to brain versus separation when varying $\mu'_{s,CSF}$ in continuous wave ($\mu'_s = 0.01$, 0.1 and 1.0 mm$^{-1}$). The error is calculated with respect to PPL$_o$, which is the Monte Carlo prediction of PPL when $\mu'_{s,CSF} = 0.001$ mm$^{-1}$.

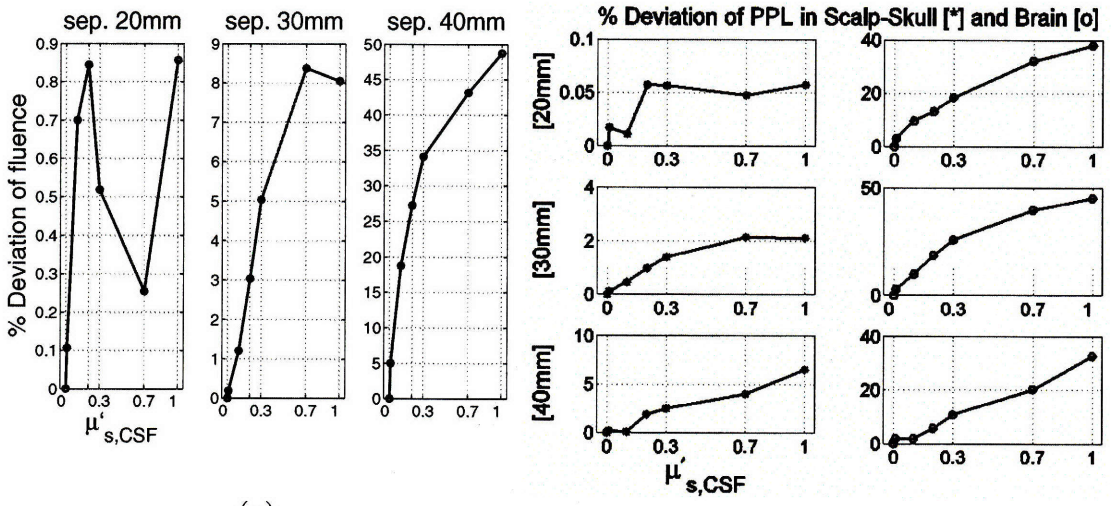


(a) (b)

Figure 2-4: (a) Deviation of fluence as a function of $\mu'_{s,CSF}$ (percentage changes with respect to $\mu'_{s,CSF} = 0.001$ mm$^{-1}$). CSF scattering coefficient varies from 0.001 to 1.0 mm$^{-1}$. The data are calculated via Monte Carlo simulations in continuous wave using $\mu'_{s,CSF}$ values of 0.001, 0.01, 0.1, 0.2, 0.3, 0.7, and 1.0. (b) Percent deviation of partial pathlength as a function of $\mu'_{s,CSF}$. The deviation is calculated with respect to PPL measured when CSF $\mu'_{s,CSF} = 0.001$ mm$^{-1}$. CSF scattering coefficient varies from 0.001 to 1.0 mm$^{-1}$ taking values of 0.001, 0.01, 0.1, 0.2, 0.3, 0.7, and 1.0, and the pathlength factor is simulated with Monte Carlo in continuous wave. Results are shown for separations of 20, 30, and 40 mm.

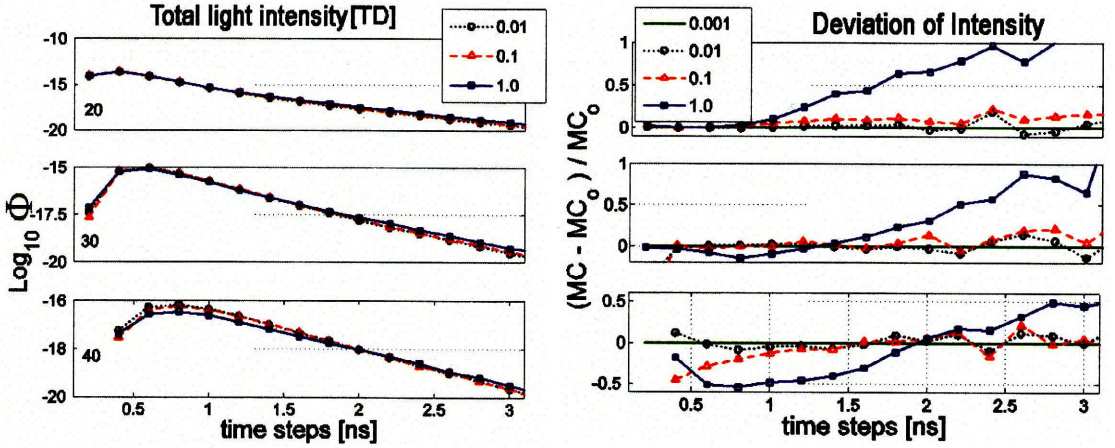


(a) (b)

Figure 2-5: (a) Temporal Point Spread Function predicted by Monte Carlo. (b) Temporal Point Spread Function relative error with respect to the reference measurement $MC_o$, simulated with $\mu'_{s,CSF} = 0.001$ mm$^{-1}$. Results are shown for separations of 20, 30, and 40 mm.

than 20% when $\mu'_{s,CSF} < 0.3$ mm$^{-1}$. In all cases, the error is greater at the earliest photon migration times when brain sensitivity is weakest.

Figure 2-7a and 2-7b show the deviation in detected fluence (Figure 2-7a) and partial pathlength factor (Figure 2-7b) versus $\mu'_{s,CSF}$ at 20, 30, and 40 mmat a time delay of 2 ns, where we see that changes greater than 20% only occur when $\mu'_s > 0.3$ mm$^{-1}$. These results further support the observation that the CSF layer can be accurately characterized by a scattering coefficient value between 0 and 0.3 mm$^{-1}$ and still provide detected fluence and brain sensitivity with an approximation error within DOT level of accuracy (between 10 and 20%).

As with the CW results, we note that for time-domain measurements the partial pathlength in the brain also increases when the CSF scattering coefficient is low (see Figure 2-6a, 2-7b). Also, importantly, sensitivity to absorption changes in the brain is significantly enhanced at time delays greater than 1.5 ns with respect to CW sensitivity measurements (compare Figure 2-3a and 2-6a).

### 2.1.7 Conclusions

We performed extensive simulation studies to quantify the deviation in photon migration measurements and sensitivity to brain given a range of CSF scattering coefficient values. Through the analysis of total fluence and partial optical pathlength using Monte Carlo simulations in an accurate MRI-based 3D head geometry we found that the CSF scattering coefficient can increase up to the inverse of its typical thickness without significant variation from a near zero scattering coefficient. The results support our initial hypothesis that an effective CSF scattering coefficient of approximately 0.3 mm$^{-1}$can be used. Under these circumstances it may be possible to obtain accurate solutions of the forward problem with the Diffusion Approximation. The advantage of using the diffusion approximation is that we can utilize faster algorithms to simulate photon migration in the adult head.

Our results also suggest that low-scattering CSF increases DOT measurement sensitivity to brain, in contrast to previous studies that assumed a simplified smooth CSF layer[32, 94, 33, 113]. CSF may change the depth sensitivity profile, but this does not mean that the signal from the cortex is decreased in the presence of low-scattering CSF. We hypothesize that the presence of the CSF layer has the effect of concentrating measurement sensitivity to the more superficial layers of the cortex, but that the overall sensitivity to cortical hemodynamics is not adversely affected.

In conclusion, our results indicate that:

1. Using a diffusion model with a CSF reduced scattering coefficient of approximately 0.3 mm$^{-1}$leads to measurements with errors no larger than 20%, for both time-domain and continuous wave.

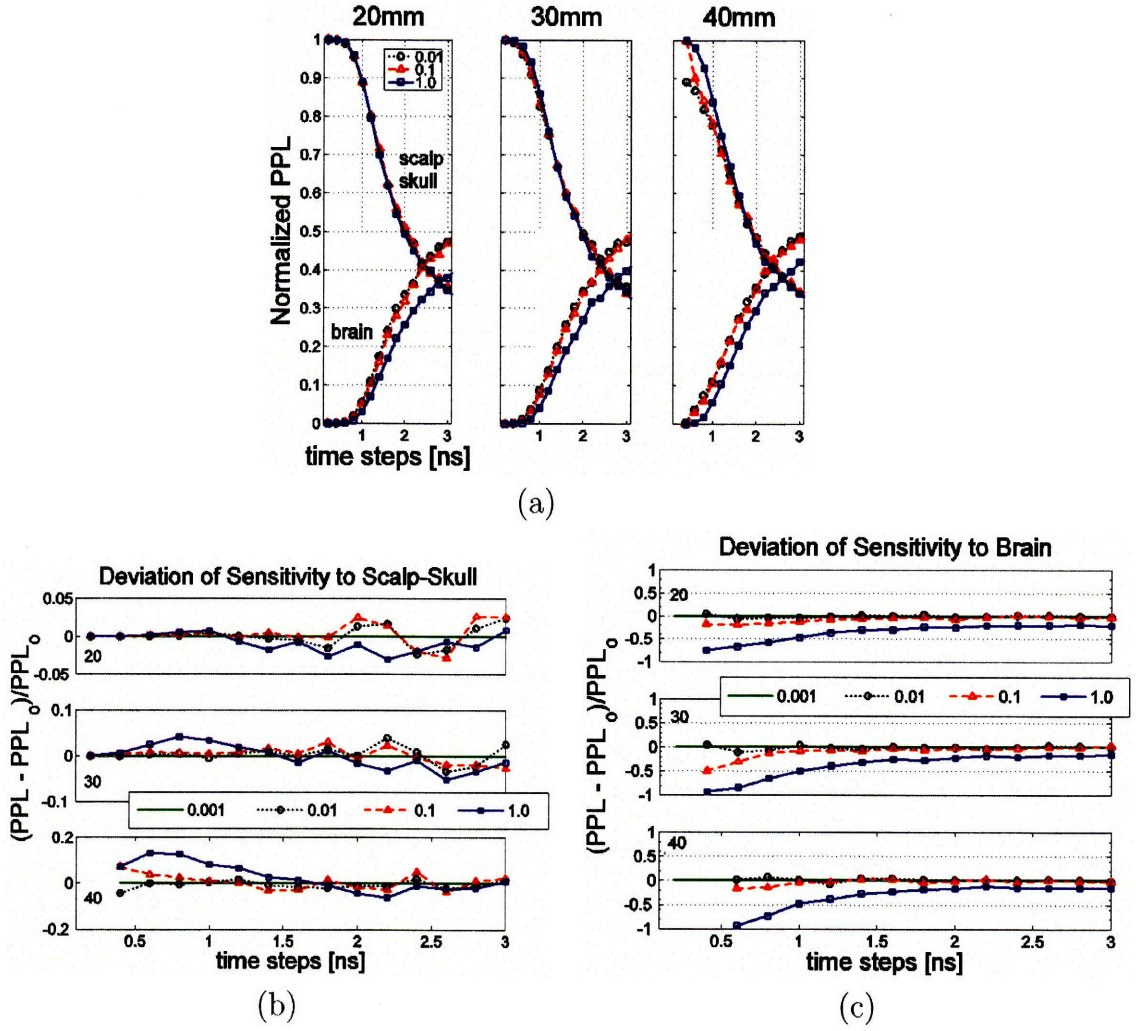


Figure 2-6: (a) Monte Carlo prediction of the optical pathlength factor at three $\mu'_{s,CSF}$: 0.01, 0.1 and 1.0 mm$^{-1}$ versus time delay normalized by the total PPL. Results are shown for separations of 20, 30, and 40 mm. (b) Relative sensitivity to absorption changes in the scalp-skull layer when $\mu'_s = 0.01$, 0.1 and 1.0 mm$^{-1}$ versus time delay as predicted by Monte Carlo. The reference measure of sensitivity to scalp-skull is given by simulating PPL when $\mu'_{s,CSF}$ is 0.001 mm$^{-1}$. (c) Time resolved Monte Carlo predictions of the relative sensitivity to absorption changes in the brain when $\mu'_{s,CSF}$ assumes the values 0.01, 0.1 and 1.0 mm$^{-1}$. The reference measure of sensitivity to brain is given by simulating PPL when $\mu'_{s,CSF}$ is 0.001 mm$^{-1}$. Results are shown for separations of 20, 30, and 40 mm.

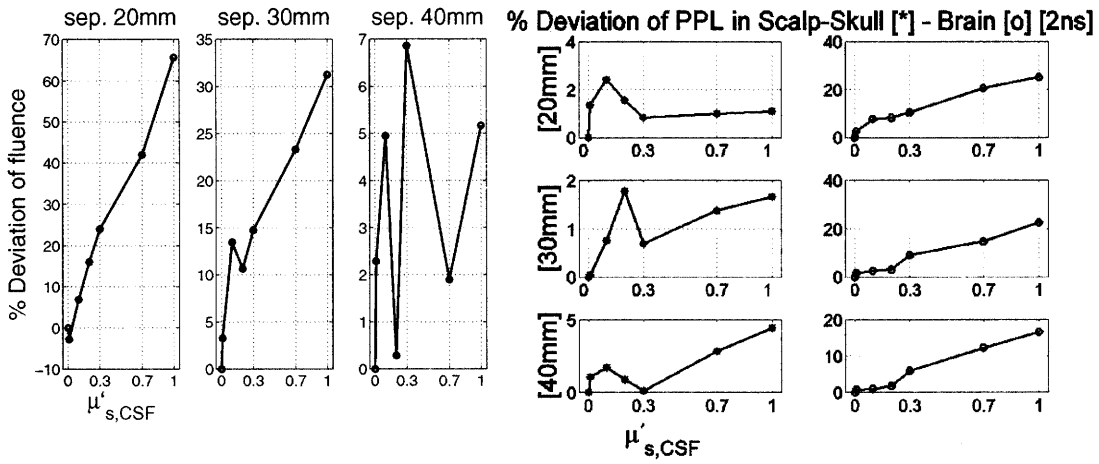


(a) (b)

Figure 2-7: (a) Deviation of fluence as a function of $\mu'_{s,CSF}$ (percentage changes with respect to $\mu'_{s,CSF} = 0.001$ mm$^{-1}$) at 20, 30 and 40 mm separation from the source at a time delay of 2 ns. CSF scattering coefficient varies between 0.001 and 1.0 mm$^{-1}$. (b) Percent deviation of Partial pathlength as a function of $\mu'_{s,CSF}$. The deviation is calculated with respect to PPL measured when CSF $\mu'_{s,CSF} = 0.001$ mm$^{-1}$. The results are shown for source-detector separations of 20, 30 and 40 mm, for a time delay of 2 ns.

2. The sensitivity of DOT measurements to cortical activity are not adversely affected by the presence of CSF in a realistic 3D head geometry

3. Time-Domain measurements can further reduce the effect of the CSF layer by increasing sensitivity to deeper tissues, in agreement with previous findings of Steinbrink et al.[111], Montcel et al.[90] and Okada et al.[94].

## 2.2 Cerebral Spinal Fluid thickness: effect on DOT

We established that the CSF scattering coefficient affects optical measurements (see Section 2.1); here we proceed to explore the effect of CSF thickness on optical measurements. We conduct our study by varying the CSF thickness of a reference head geometry (the MNI single subject atlas [25]) by eroding, dilating, and thresholding the probability of a voxel belonging to CSF. Knowing the effect of CSF thickness on the DOT forward model will lead to considerations on parameters related to CSF thickness variability (such as the subject's age and gender, see Section 2.3): if CSF thickness is predictable using the subject's personal information, then a general head model can be customized to match a subject's CSF thickness without the intervention of anatomical MRI information, and the general head can be used in place of the subject's head for the solution of the DOT forward model, yielding a purely optical tomography image process (see Chapter 5). Our observations indicate that changes

in CSF thickness of $\sim 3$ mm(often that is 50% of the typical CSF thickness) result in small errors (less than 15% for separation less than 32 mmfrom the source). Moreover, we have investigated the effect of skull thickness on optical partial pathlength (results not shown) and have found that a variation of skull thickness of a few millimiters did not significantly affect the partial pathlength.

### 2.2.1 Methods

We simulate photon migration by combining eight independent Monte Carlo runs [16], injecting $10^8$ photons in each simulation. We specify four tissue types with optical properties as described in Table 2.2, which are the same as those used previously [18, 112, 13].

Table 2.2: Subject vs. atlas study's optical properties

| Tissue type | $\mu_a$ [mm$^{-1}$] | $\mu_s$ [mm$^{-1}$] |
|---|---|---|
| scalp | 0.0159 | 0.8 |
| skull | 0.0101 | 1.0 |
| CSF | 0.0004 | 0.01 |
| brain | 0.0178 | 1.25 |

The head model employed is the MNI Colin head [25], 181x181x217 voxels of 1 mm$^3$ each (see Section 4.2.1 for more details on the MNI atlas). The atlas' segmentation is also provided by [25], and it specifies each voxel's probability of belonging to one of the four tissues of interest (scalp, skull, CSF, and brain). We calculate the default segmented head model (model A in Figure 2-8), by choosing the tissue of highest probability for each voxel.

We compare four different head models (see Figure 2-9B-E) varying CSF thickness of the reference MNI model (model A, see Figure 2-8A). We calculate a CSF inflated model (B) by taking CSF voxels at 0.01% from the MNI statistical Colin head [25]. Conversely, we inflate the CSF layer by dilatation (model C) using a 3x3 structural element. The last two models are characterized by a thinner CSF layer: the first (model D) is calculated by inflating the non-CSF tissues, by taking gray matter, scalp and skull voxels at 5%; the second one (model E) is obtained by erosion by a factor of 3. We use a linear probe as shown in Figure 2-9 (the red square is the single source, the red stars are the 25 detectors, equally spaced between 10 mmand 58 mmseparation from the source).

We calculate the total fluence ($\Phi$) and partial path length (for method details see [27]) for each of the five configurations described above (see Figure 2-10a for $\Phi$ and Figure 2-11a for PPL). Then, we calculate the error induced by a thicker or thinner CSF layer relative to the *ground truth* (which is model A) and show the results in Figure 2-10b (relative fluence) and Figure 2-11b (relative PPL).

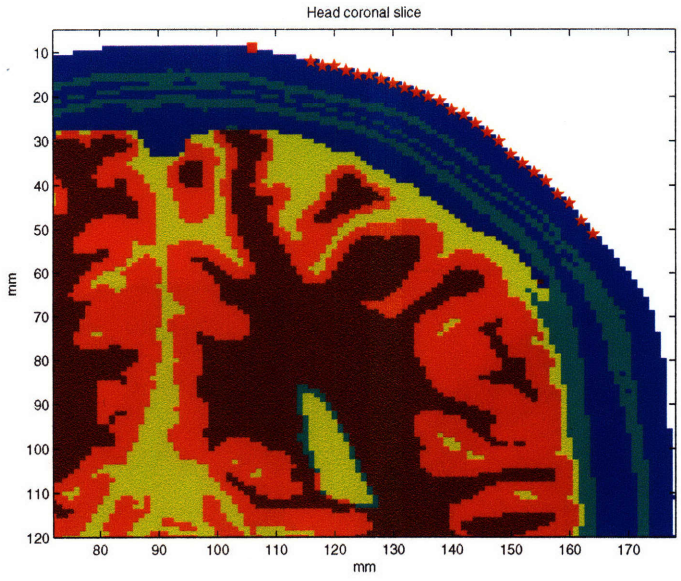


(A)

Figure 2-8: The figure shows a coronal slice of the head model used as a reference for CSF thickness. The chosen head template is the well known MNI single subject atlas [25]. The linear probe is visible on the top-right side of the slice: the red square is the single source, the red stars are the 25 detectors, equally spaced between 10 mmand 58 mmseparation from the source.

### 2.2.2 Results and Conclusions

In Figure 2-10a we plot the fluence $\Phi$ in continuous-wave in logarithmic scale (see Equation 2.1) as a function of source-detector separation: each symbol represents data from each model, the default measurements from model A are plotted with a black star, model B and C (increased CSF thickness) are marked with blue symbols, and model D and E (decreased CSF thickness) are colored in red. Figure 2-10b shows the fluence deviation (in percent) with respect to the fluence measured with the default head model A ($\Phi_o$), as a function of source-detector separation: empty symbols are used for models with increased CSF thickness, whereas full symbols indicates data calculated for the models with decreased CSF thickness. Overall, we see that, within 36 mmfrom the source, the fluence discrepancy is less than 20%.

In Figure 2-11a, we show the normalized partial pathlength within CSF, brain and scalp-skull tissues, normalized so that:

$$\sum_{m=[scalp-skull,CSF,brain]} (\mathrm{PPL}_m) = 1.$$

The partial pathlength is the partial derivative of the optical density with respect to the changes of absorption coefficient in a tissue type and therefore is a good measure of sensitivity to absorption changes of that specific tissue. The plot shows the PPL for

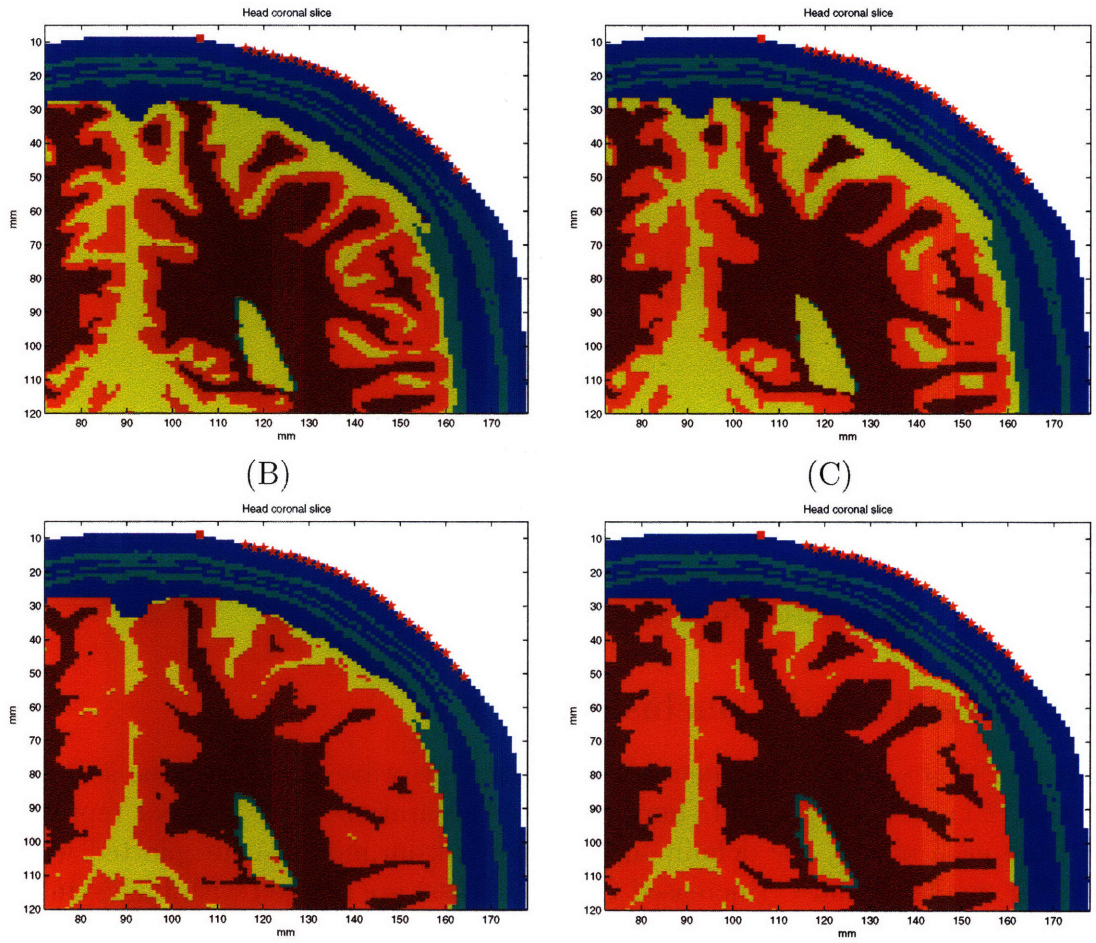


Figure 2-9: The figures show a coronal slice of the head models used to guide photon migration simulations. (B-C) are the CSF thickened models, (D-E) are the CSF thinned models. The optical probe is visible on the slices: the red square represent the single source location and the red stars show the position of the detectors. Note how the thresholded models (B and D) best preserve the layers structures compared to model C and E (for example, model E has an anatomically incorrect thin gray matter layer over CSF).

scalp-skull in red, the PPL for CSF in black, and the PPL for brain in blue; the plot on the top row shows the total normalized PPL for models with increased CSF thickness (model B dash-dot line; model C dotted line) compared to the default model A (solid line); the bottom plot shows the PPL of models with decreased CSF thickness (model D in dash-dot line; model E with dotted line), showing model A with a solid line as the control case. The qualitative plot in Figure 2-11(a) is complemented by the quantitative plot in Figure 2-11(b) that leads to a more thorough performance analysis; the relative sensitivity is calculated by subtracting the PPL calculated by model A ($PPL_o$) to the PPL calculated by model B, C, D and E (called simply PPL in the plot $y$ axis label), multiplying the result by 100, and then dividing the result by $PPL_o$ (see Equation 5.5); the relative difference in predicted sensitivity within the scalp-skull layer is very small for every model (within 1.1% error for source-detector separation less than 26 mm, which is the range of greater sensitivity to superficial tissues, highlighted by the light gray box); the more interesting relative sensitivity to absorption changes in the brain (lower plot) shows that in the source-detector separation range of highest sensitivity to the brain (highlighted by the light gray box), which is between 28 mmand 38 mm, the discrepancy between the reference PPL ($PPL_o$ of model A) and the other models' PPL is small (less than 10%) for models B (black) and D (blue), that are obtained modifying CSF thickness by thresholding, whereas larger discrepancy (between 10% and 30%) is observed for models C (red) and E (cyan), that do not preserve as well the tissues layers architecture.

All plots confirm that a 50% change in CSF thickness produces small errors (less than 15% for separation less than 32 mmfrom the source). The only significant discrepancies observed are (1) in brain sensitivity when CSF is eroded at separations shorter than 18 mm, due to the extremely small signal reaching the brain at such separations and (2) when CSF is dilated at separations larger than 24 mm, due to the low absorbing effect of the thicker clear layer: more photons probing the brain at $> 24$ mm separation are scattered back and detected, hence the higher measured PPL.

## 2.3 Cerebral Spinal Fluid thickness: variability across population

For imaging brain activation using Diffuse Optical Tomography (DOT) we use a subject specific MR anatomical scan to spatially constrain the Monte Carlo simulation of photon migration. To fully exploit DOT advantages (such as low cost and portability), we propose using an anatomical head atlas. Because DOT is sensitive to Cerebral Spinal Fluid (CSF) thickness, as shown in Section 2.2, we would like the atlas head's CSF thickness to match that of the subject. Here, we show how to predict the subject's CSF thickness knowing only age.

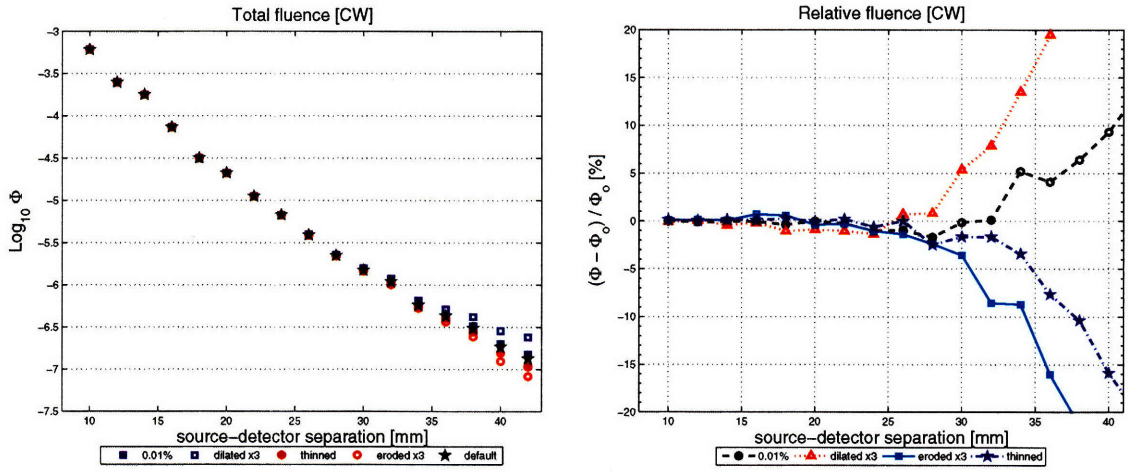


(a) (b)

Figure 2-10: (a) Logarithmic scale plot of the fluence $\Phi$ in continuous-wave as a function of source-detector separation: each symbol represents data from each model, the default measurements from model A are plotted with a black star, model B and C (increased CSF thickness) are marked with blue symbols, and model D and E (decreased CSF thickness) are colored in red. (b) Plot of the fluence deviation (in percent) with respect to the fluence measured with the default head model A ($\Phi_o$), as a function of source-detector separation: empty symbols are used for models with increased CSF thickness, whereas full symbols indicates data calculated for the models with decreased CSF thickness.

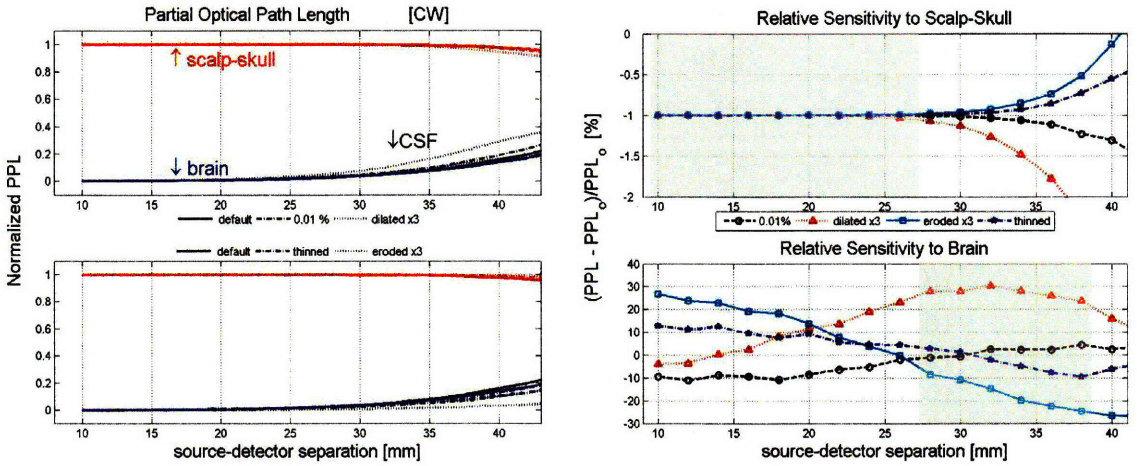


Figure 2-11: (a) Plot of the normalized partial pathlength within CSF, brain and scalp-skull tissues: the PPL for scalp-skull is shown in red, the PPL for CSF in black, and the PPL for brain in blue; the plot on the top shows the total normalized PPL for models with increased CSF thickness (model B dash-dot line; model C dotted line) compared to the default model A (solid line); the bottom plot shows the PPL of models with decreased CSF thickness (model D in dash-dot line; model E with dotted line), showing model A with a solid line as control case. The qualitative plot in (a) is complemented by the quantitative plot in (b) that leads to a more thorough performance analysis; the relative difference in predicted sensitivity within the scalp-skull layer is very small for every model (within 1.1% error for source-detector separation less than 26 mm, which is the range of greater sensitivity to superficial tissues, highlighted by the light gray box); the more interesting relative sensitivity to absorption changes in the brain (lower plot) shows that in the source-detector separation range of highest sensitivity to the brain (highlighted by the light gray box), which is between 28 mm and 38 mm, the discrepancy between the reference PPL ($PPL_o$ of model A) and the other models' PPL is small (less than 10%) for models B (black) and D (blue), that are obtained modifying CSF thickness by thresholding, whereas larger discrepancy (between 10% and 30%) is observed for models C (red) and E (cyan), that do not preserve as well the tissues layers architecture.

### 2.3.1 The data set

For this study we use a dataset of anatomical MRIs of thirty-two healthy subjects, 18 males and 14 females, between 21 and 76 years old. In Table 2.3 we show the subjects' age and gender.

Table 2.3: Subjects' Dataset

| **Sbj** | age | gnd | **Sbj** | age | gnd | **Sbj** | age | gnd |
|---|---|---|---|---|---|---|---|---|
| 1 | 36.67 | M | 2 | 22.97 | M | 3 | 71.25 | M |
| 4 | 42.95 | M | 5 | 72.38 | F | 6 | 72.03 | M |
| 7 | 23.39 | M | 8 | 43.08 | F | 9 | 69.28 | M |
| 10 | 26.59 | F | 11 | 76.60 | F | 12 | 22.96 | F |
| 13 | 59.67 | F | 14 | 43.05 | M | 15 | 72.37 | F |
| 16 | 73.05 | M | 17 | 25.90 | F | 18 | 34.51 | F |
| 19 | 51.81 | F | 20 | 69.20 | M | 21 | 70.24 | M |
| 22 | 25.02 | M | 23 | 25.85 | F | 24 | 24.51 | M |
| 25 | 21.79 | M | 26 | 65.08 | F | 27 | 69.14 | M |
| 28 | 25.46 | M | 29 | 57.55 | F | 30 | 52.15 | M |
| 31 | 68.37 | F | 32 | 37.33 | M | – | –.– | - |

The anatomical MRI acquisitions are FLASH scans with TR = 20 ms, TE = 1.8 ms and variable flip angles (here used 30°) [44]. Each subject's MRI is segmented into skin-skull-CSF-brain using FreeSurfer's mri_watershed segmentation tool [1]. This initial estimate is refined into a more accurate CSF segmentation (Figure 2-12E and Figure 2-13E, yellow tissue); the description of the segmentation process is outlined in 2.3.2.1.

### 2.3.2 Methods

To calculate CSF thickness, we first prepare the dataset by extracting a fine mesh from the 3D voxel image. The mesh is calculated by selecting the superficial voxels by means of a differential-shift method that extracts the volume's boundaries, and then transforming the matrix voxel coordinates $i$, $j$, $k$ into Cartesian coordinates $x$, $y$, $z$ centered at $(i, j, k) = (1, 1, 1)$. Each mesh point corresponds to a scalp voxel above the ears' line and each subject is described by a mesh of 30,000 to 90,000 points.

#### 2.3.2.1 New CSF segmentation

Starting from the mri_watershed segmentation, we redefine CSF as the voxels labeled CSF by mri_watershed (Figure 2-12C and 2-13C, green tissue) and, at the same time, the voxels within the intensity range of CSF (Figure 2-13B). A similar idea has been tried for a better bone segmentation, but unsuccessfully: the intensity range of the skull is overlapping with the intensity of superficial skin pixels making them

inseparable. Each segmented head has been cut below the ears' line to eliminate voxels not involved in the imaging process of brain activity.

Then, we re-labeled the remainder of Figure 2-12C CSF (Figure 2-12D and 2-13D, maroon tissue) as skull (Figure 2-12E and 2-13E, light-blue tissue). These are voxels outside the CSF intensity range but surround CSF, which are our best definition of skull voxels. Unfortunately, poor characterization of the skull makes conducting a population skull thickness study unfeasible, although bone tissue also highly affects DOT measurements. However, our study on a single subject's (see Section 2.2) skull thickness (data not shown) suggests that a small variation on bone thickness (within 3 mm) does not significantly affect skull optical path length.

In Figure 2-12A-E is shown a close-up of the MRI anatomical image and its segmentations; some tissues are labeled for clarity: CSF is the dark gray tissue of Figure 2-12A, filling the ventricles and surrounding the gray matter; in Figure 2-12C, the mri_watershed segmentation, CSF is colored in green, whereas in Figure 2-12E, our final segmentation, CSF is the light-blue tissue. Each step of the new CSF segmentation process is shown in Figure 2-13A-E: from the subject's MRI (A) we calculate a map of voxels within the CSF intensity range (B) and we calculate the final CSF (D) by intersecting the voxels in image B with the CSF voxels from image C. Finally, we re-label the portion of CSF in C but not in D as skull (result shown in Figure 2-13E). To conclude our segmentation process we need one last step: mri_watershed segmentation cuts off some scalp voxels that we manually reintegrate by thresholding Figure 2-13A with the proper skin intensity range and then filling the gaps using connected components.

#### 2.3.2.2 Calculation of CSF thickness

After calculating each subject's head segmentation, we compute the CSF thickness by extracting a scalp mesh (one point per scalp voxel) and then projecting each mesh point toward the Anterior Commissure (AC) which "*is a bundle of white fibers, connecting the two cerebral hemispheres across the middle line [...]. On sagittal section it is oval in shape, its long diameter being vertical and measuring about 5 mm. It serves in this way to connect the two temporal lobes, but it also contains decussating fibers from the olfactory tracts*" [57]. The Anterior Commissure point has the advantage of being easily and uniquely identifiable from both the anatomical MR and the segmentation images (see Figure 2-14). At each 0.1 mm step, we examine the current position's tissue type and record it, stopping after 400 steps or after probing 5 mm of brain.

### 2.3.3 Results

Figure 2-15 shows how CSF thickness varies on three subjects selected to span the dataset age range: a 27 year old female, a 43 year old male and a 72 year old female. We plot CSF thickness at each sampled mesh point using a jet color scheme. It is easy to notice the strips of lighter blue and yellow (thicker CSF) along the sulci and

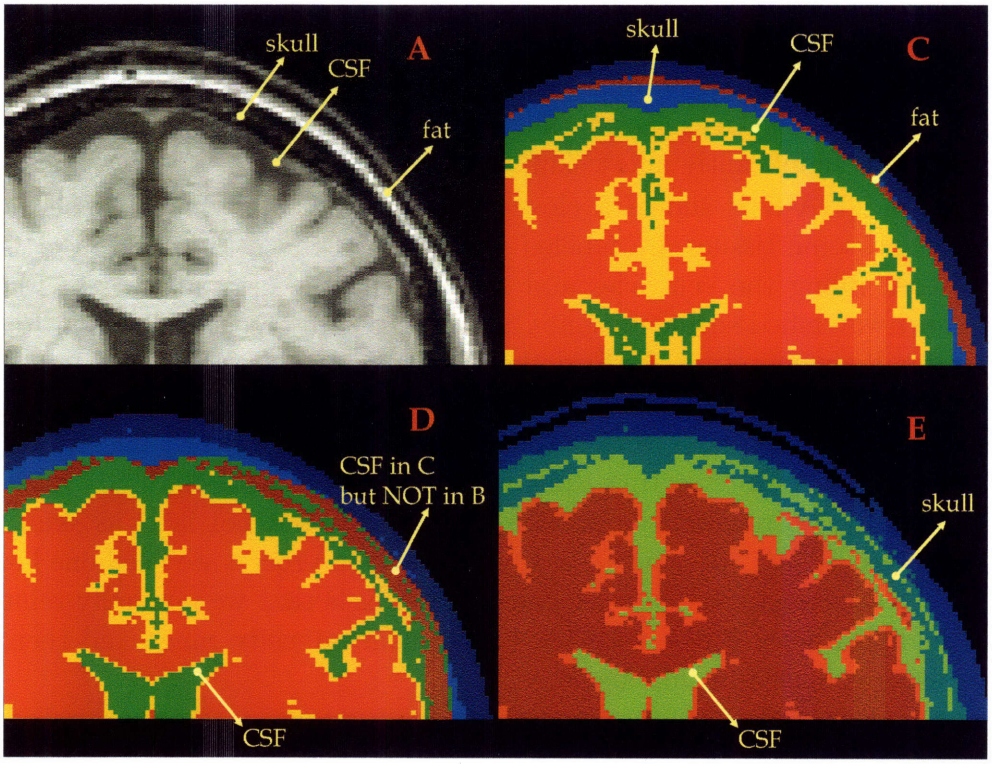


Figure 2-12: (A) shows the subject anatomical MRI; for clarity some tissue types are labeled (skull, fat and CSF). Optically we group together fat, muscle and skin as they have indistinguishable optical properties. (C) shows the segmentation calculated with FreeSurfer's mri_watershed; the green tissue is labeled CSF, the maroon is labeled fat and the light blue as skull. It is clear that such labeling is incorrect when looking at the intensity map A. (D) is C where CSF is calculated as the intersection between the CSF in C and a thresholded CSF map from A (shown in Figure 2-13B). The green tissue is again CSF and the maroon is what is labeled CSF in the mri_watershed segmentation (C) but is not in the CSF intensity range (which is not CSF in the map from Figure 2-13B). In (E) is shown our best CSF segmentation. CSF is in yellow and corresponds to the green tissue of image D; what was colored in maroon in D is now colored in light blue and labeled skull; when comparing image E to image A, the improvement of the segmentation is clearly visible.

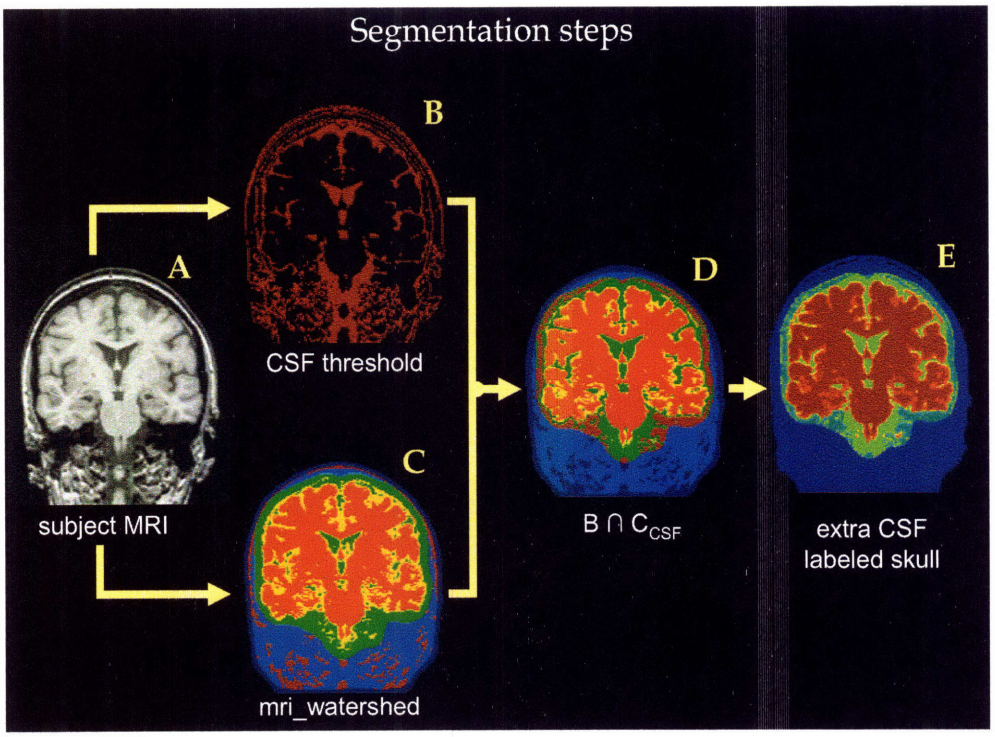


Figure 2-13: From the subject's MRI (A) we calculate a thresholded map of CSF (B) and we calculate the final CSF (D) by intersecting B with the CSF found by FreeSurfer's mri_watershed (in C, and the result of the intersection shown in D). Finally, we re-label the portion of CSF in C but not in D as skull (E). The segmentation offered by mri_watershed peels off some scalp voxels that we manually reintegrate by thresholding A with the proper skin intensity range and then filling the gaps using connected components.

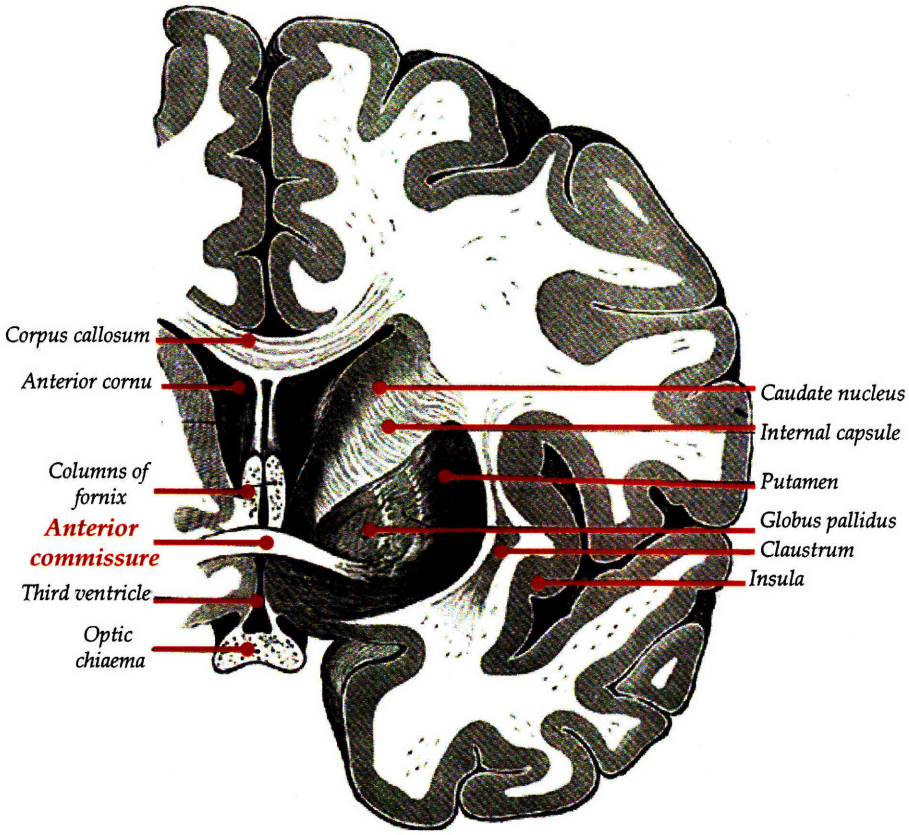


Figure 2-14: Anterior Commissure (AC) point (from the $20^{th}$ U.S. edition of Gray's Anatomy of the Human Body [57]) is a bundle of white fibers, connecting the two cerebral hemispheres across the middle line; it has the advantage of being easily and uniquely identifiable from both the anatomical MR and the segmentation images.

the gradually increasing CSF thickness (over 10 mm) spreading over the entire head with the progressing of age.

We repeated the same measurements on the subjects' heads normalized to the MNI standard space using Statistical Parametric Mapping (SPM5) registration toolbox (Wellcome Department of Cognitive Neurology, University College, London) [3]. These data (not shown) non surprisingly confirm the un-normalized results, since affine transformations do not affect relative distances and thicknesses.

#### 2.3.3.1 Age

In Figure 2-16 the median of the CSF thickness over the queried mesh points is shown as a function of age. We use red stars for female subjects and blue circles for male subjects. With few exceptions, subjects under 35 years of age are characterized by a median CSF thickness of no more than 3.2 mm, whereas subjects over 38 have thicker CSF, and in particular subjects older than 64 exhibit the highest median CSF thickness of over 5.5 mm and up to 6.5 mm. We calculated the statistical correlation of age and CSF thickness and found them highly positively correlated ($p < 0.005$).

#### 2.3.3.2 Gender

The relationship between gender and CSF thickness is presented in Figure 2-17. We show the gender histogram with bins of 0.5 mm width; on the $y$ axis we report the number of subjects in the same CSF thickness bin; male subjects are plotted in blue whereas women's data are colored in red. It is not obvious whether there is a trend between gender and CSF thickness but after calculating the statistical correlation, we found that gender and CSF thickness are uncorrelated.

### 2.3.4 Conclusion

This study shows that there is a relationship between subject's age and its CSF thickness. Therefore, it is possible to predict CSF thickness without obtaining the subject's anatomical MRI, which might not be available. The presence of outliers of a linear model fitting the data (see Figure 5-5) suggests that a more robust statistics can be achieved by increasing the dataset size. Furthermore, the relationship between age and CSF thickness can be further analyzed by measuring spinal fluid thickness using other techniques; for example, a study can be conducted to estimate CSF thickness from the number of detected photons by deriving from a physical subject head model a set of segmented heads with varying CSF thickness and finding the synthetic head model and associated CSF thickness that better describe the number of photons detected experimentally. By repeating the experiment on several subjects of several ages, it is possible to learn the relationship between number of photon detected on a specific probe and underlying CSF thickness and, consequently, estimating one from the other for a more accurate estimate of the subject CSF thickness.

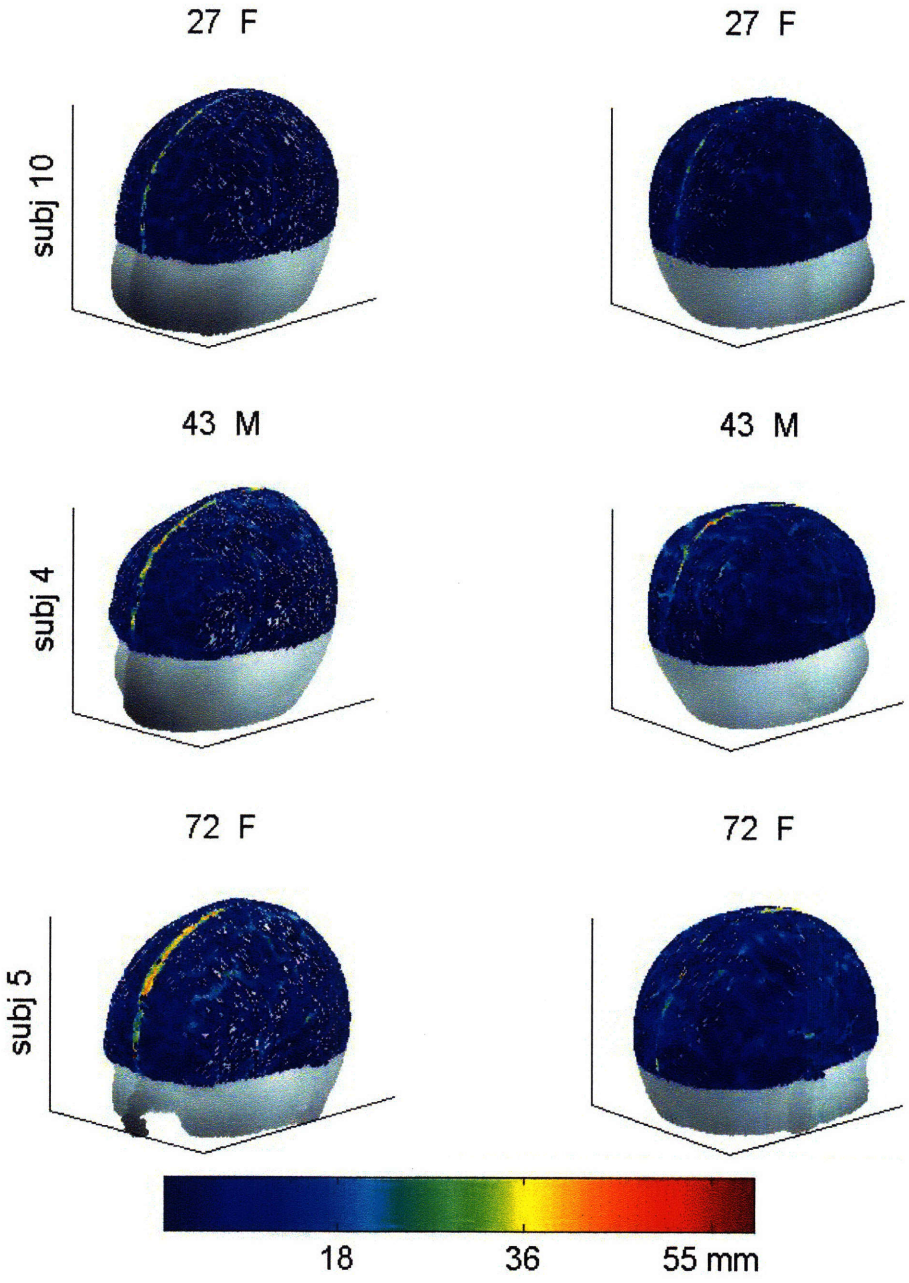


Figure 2-15: Qualitative plot of three selected subjects' CSF thickness. The subjects have been selected to represent three age ranges: under 35, between 35 and 60, and over 60, because we observed smaller variability of CSF thickness within each of these three age groups (see Figure 2-16 red, green and blue ellipsis). For each subject, two views (left and right temporal regions) are shown; each view presents the head scalp in light gray over plotted with the color corresponding to the value of the CSF thickness at each scalp voxel measured by projecting the voxel toward the AC point. The CSF thickness-age relationship is particularly visible on the central sulcus, as CSF in that area varies thickness from 20 mm (light blue) in the 27 year old subject up to 40 mm (yellow) in the 72 year old subject.

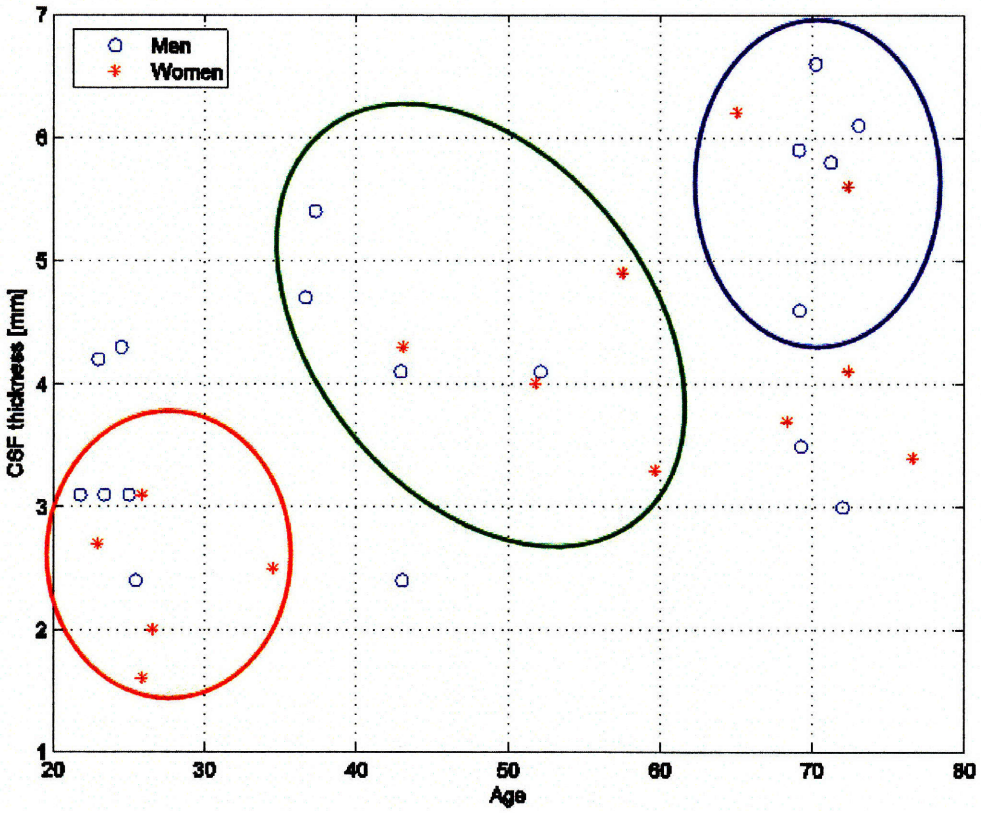


Figure 2-16: The CSF thickness (in mm) is shown as a function of age over our dataset of 32 healthy subjects. The CSF thickness is calculated by projecting each surface point above the ear-line toward the AC point while keeping score of the millimeters of CSF encountered along the surface voxel-AC point trajectory; then, we take the median of the calculated values to account less for the thickest CSF found on the main sulci. CSF thickness-age groups are highlighted with a red ellipse (subjects between 20 and 30 years old with CSF thickness between 1.5 and 3.2 mm), a green ellipse (subjects between 36 and 60 years old with CSF thickness between 3.3 and 5.5 mm), and a blue ellipse (subjects over 65 years old with CSF thickness over 4.5 mm). A high correlation has been found between age and CSF thickness ($p < 0.005$), suggesting that age could be a sufficient parameter to estimate CSF median thickness.

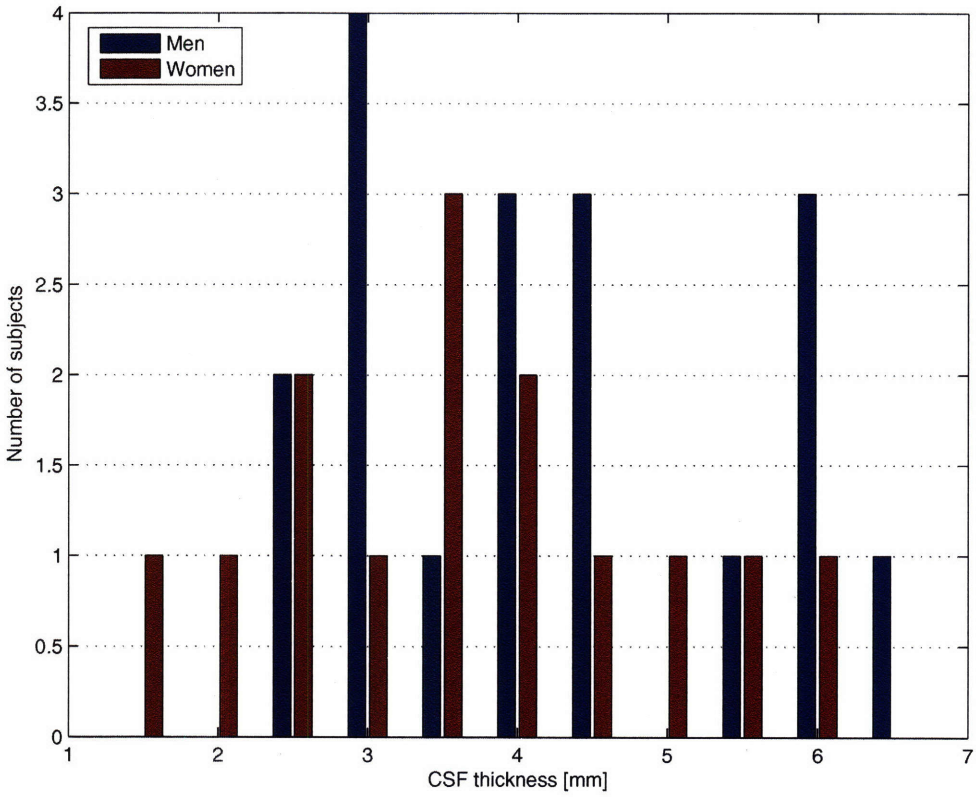


Figure 2-17: The histogram shows the distribution of CSF thickness across subjects as a function of gender. The highest median CSF thickness value (6.7 mm) is found in a man (70 years old) and it can be noticed that CSF thickness is less variable among men (higher subjects count, which is $y$ axis value, for fewer CSF values).

Our results show that a subject's CSF thickness can be inferred from his age and therefore a general head model's CSF layer can be customized to match the subject's estimated CSF thickness without the need of the subject's anatomical MRI, which is a key step to using an atlas' anatomy in place of a subject specific's to guide a purely optical tomography forward problem (see Chapter 5).

As CSF thickness is coupled with cortical thickness, interesting results published for cortical thickness can be extended to CSF thickness, provided the spinal fluid thickness is accurately measured (for example with the segmentor we propose in Section 2.3.2.1). In particular, changes in the gray matter have been reported to be related to normal aging [31, 73], Alzheimer's disease [31, 73, 4, 50, 58, 37, 107] and other dementias [78], Huntington's disease [117, 61], corticobasal degeneration [20], amyotrophic lateral sclerosis [79], and schizophrenia [124, 123, 104, 83]. Since the cortical thinning (and consequently the increase of CSF thickness) is often specific of certain regions, the progress of brain atrophy can be very informative on the evolution and causes of the disease. Moreover, CSF thickness can be used in longitudinal studies to assess the efficacy of various treatments to neurodegeneration.

# Chapter 3

# Fast simulation of photon migration

In order to achieve a reliable solution of the DOT inverse problem and therefore meaningful brain activation maps, it is necessary to have an accurate photon migration model. The most accurate mathematical model describing photon migration is the Radiative Transfer Equation (RTE) (see Equation 1.8), but unfortunately its analytical solution is not available and therefore the RTE is solved numerically by using accurate but computationally expensive Monte Carlo-based algorithms. In the literature are found several studies on less computationally expensive solutions of the optical imaging forward problem, exploiting sophisticated combinations of mathematical models and/or more realistic head models (see Section 3.1 for a review). Our approach is quite different, as we propose the use of a well known faster solver of the DOT forward model based on Diffusion Approximation (DA) (see Equation 1.14) in a realistic head model, made possible by approximating the spinal fluid scattering coefficient with the inverse of the average straight-line distance traveled by a photon through this tissue type (see Section 2.1).

For validation purposes, we compare the performances of the Monte Carlo (MC) simulator proposed by Boas et al. [16] with those of the Finite Difference (FD) algorithm presented by Barnett at al. [13] that solves the Diffusion Approximation analytically in time-domain and continuous wave. The continuous wave results show that the Finite Difference approach to the diffusion equation offers greater computational efficiency, but at the cost of modeling accuracy. The time-resolved data are more encouraging, though, suggesting that a Time Domain DOT instrument can successfully take advantage of a more efficient solution of the Diffusion Approximation of photon migration as long as the first few data points are discarded (considering data points after 1.4 ns) and the separation between source and detectors is sufficient to probe the brain (source-detector separation $> 28$ mm). Therefore, diffusion based methods can well predict photon scattering through the human head provided that a realistic head model is used and the probe is designed to maximize Contrast to Noise Ratio (CNR) in the brain.

## 3.1 Background

Several papers have been published by Okada et al. [98, 54, 62, 82], Arridge et al. [10, 11], Firbank et al. [39], and Hielscher et al. [63] exploring a variety of models of light propagation in highly scattering medium with properties similar to that found in the human head. The low scattering properties of the Cerebral Spinal Fluid (CSF) filling the space between the brain and the skull has been of particular concern in the development of an accurate photon migration forward problem for the human head as the diffusion equation is known to provide inaccurate solutions under such circumstances [63, 98, 65]. It remains to unequivocally establish whether this low scattering region (often called the void region) decreases [32] or increases [54, 95] sensitivity to the underlying brain tissue. As a result, several papers have been published exploring implementation of the transport equation [63] or hybrid combinations of the transport equation and the diffusion equation [62, 82].

A number of papers have shown that the transport equation is necessary to accurately describe photon migration in the presence of a low scattering region [63, 62, 95, 106, 34]. But recently, it has been suggested that the diffusion equation may be sufficiently accurate given the folding nature [98, 13] of the low scattering region between the brain and the skull and the fact that this space is filled with connective tissue and blood vessels [96]. The irregularity of this tissue type is of particular interest as it limits the average straight-line distance that a photon would travel in the "void" region (which is the Cerebral Spinal Fluid layer). Thus, even if the "void" region does not scatter light, we could treat it as if it had an effective scattering coefficient such that the typical scattering length is greater than the average straight-line distance through the "void" region. For example, if the average straight-line distance that a photon could travel through the "void" region is 3 mm, we could say that the effective scattering coefficient is $0.3\,\mathrm{mm}^{-1}$. The diffusion equation may be accurate under such conditions.

In Section 2.1 we measured the accuracy of approximating the CSF scattering coefficient with the inverse of the average straight-line distance traveled by a photon through this tissue type. Once we establish that such error is negligible, we can model the light propagation in the head with a diffusion equation based algorithm (such as Finite Difference [13]) and significantly decrease the forward model run time and consequently the time necessary to produce on-line measurements of human brain activation.

Finite Difference (FD) provides a solution to the diffusion equation; however, it relies on assumptions that break down at the early time steps of photon propagation and for very small scattering coefficients. Some of the Finite Difference approach's characteristics are the importance of boundary conditions for the accuracy of the model, and its extremely short run time (on the order of minutes instead of several hours of the Monte Carlo solver), which makes it computationally inexpensive to run multiple times the FD solver of DOT forward model on diverse probes and optical property configurations.

## 3.2 Diffusion theory vs. Transport theory

Once we show that increasing the scattering coefficient in the "void" space that is CSF does not significantly alter the detected photon fluence or the partial path-length within each tissue type until the inverse scattering coefficient (which is the scattering length) becomes comparable to and shorter than the typical path-length through the "void" space (see 2.1), we can proceed one step further and compare diffusion theory with transport theory. While diffusion theory is known to produce inaccurate and unphysical results for scattering coefficients near zero [63], diffusion theory is likely to produce accurate results for realistic head geometries with a scattering coefficient of $\sim 0.3$ mm$^{-1}$ for the CSF layer.

For a more comfortable reading, we repeat the expressions for the Radiative Transfer Equation (RTE), numerically solved by Monte Carlo [16], and for the Diffusion Approximation (DA), analytically solved by Finite Difference (FD) [13], as described in Equation 1.8 and 1.14 respectively:

*Radiative Transfer Equation:*

$$\frac{1}{\nu}\frac{\partial R(\mathbf{r},\hat{s},t)}{\partial t} = -\hat{s}\cdot\nabla R(\mathbf{r},\hat{s},t) - \mu_t R(\mathbf{r},\hat{s},t) + \mu_s H + R_o(\mathbf{r},\hat{s},t) \ ,$$

where $\nu$ is the speed of light in the tissue determined by the relative refractive index $n$, $\mu_t = \mu_a + \mu_s$ is the extinction coefficient, $R_o(\mathbf{r},\hat{s},t)$ is the radiance of the light source, $H$ accounts for the scattering effect and is equal to:

$$H = \int_{4\pi} R(\mathbf{r},\hat{s},t)\Theta(\hat{s}'\cdot\hat{s})d\Omega' \ ,$$

and $\Theta(\hat{s}'\cdot\hat{s})$ is the phase function, representing the probability of light with propagation direction $\hat{s}'$ being scattered into a solid angle $d\Omega$ around $\hat{s}$;

*Diffusion Approximation:*

$$\frac{1}{\nu}\frac{\partial\Phi(\mathbf{r},t)}{\partial t} + \mu_a\Phi(\mathbf{r},t) - \nabla\cdot(D\nabla\Phi(\mathbf{r},t)) = \Phi_o(\mathbf{r},t) \ ,$$

where $D$ is the diffusion coefficient:

$$D = \frac{\varepsilon}{3(\mu_a(r)+\mu_s'}.$$

## 3.3 Method

We use a 3D head model generated from a subject MRI scan; such head geometry allows us to specify up to five tissue types (scalp, skull, CSF, gray and white matter) but for most of our test we use three (as described in Table 2.2). The whole volume

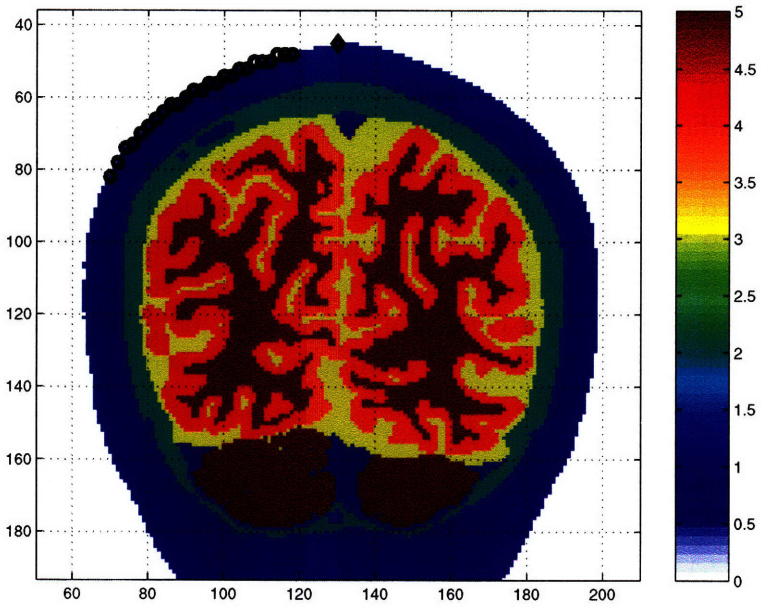


Figure 3-1: A coronal slice of the head model: the skin-muscle is colored in blue, skull is colored in light blue, CSF in yellow, gray matter in orange and white matter in maroon; the linear probe is plotted with black circles (the 25 detectors) and a black diamond (the single source). Each tissue type's optical properties are reported in Table 2.2; for the CSF scattering coefficient, the legends of the plotted results indicate when multiple values have been adopted.

is voxelized in a cube with 256 voxels on each side ($256^3$ voxel in total, 1 $mm^3$ each) or $128^3$ voxels, 2 $mm^3$ each: two different spatial resolutions are used to compare the forward model's performances. The head is surrounded by air (tissue type 0) and the five non-zero tissue types' optical properties are described in Table 2.2.

From this head volume, we define a sub-region of 81 $mm^3$ starting at the single source is cropped out of an air tissue type background in order to reduce the size of the head and reduce the computational cost. The single source and the 25 detectors are placed on the top-left corner of the head and the detectors placement follows a linear scheme (all detectors are placed on the same plane as the source). We use index of refraction $n = 1$ and scattering anisotropy $g = 0.01$.

We acquire several measurements, such as Partial Optical Path Length (PPL) in time domain and continuous wave, detected fluence rate, detected fluence, and Spatial Sensitivity Profile, using Finite Difference and Monte Carlo simulation of 11 independent run of $10^8$ photons each, to increase Monte Carlo SNR.

### 3.3.1 Solution of Diffusion Approximation

The diffusion approximation of the transport equation assumes isotropic scattering and therefore loses the scattering angle information simplifying greatly the equation modeling photon migration in highly scattering medium. The main reasons for de-

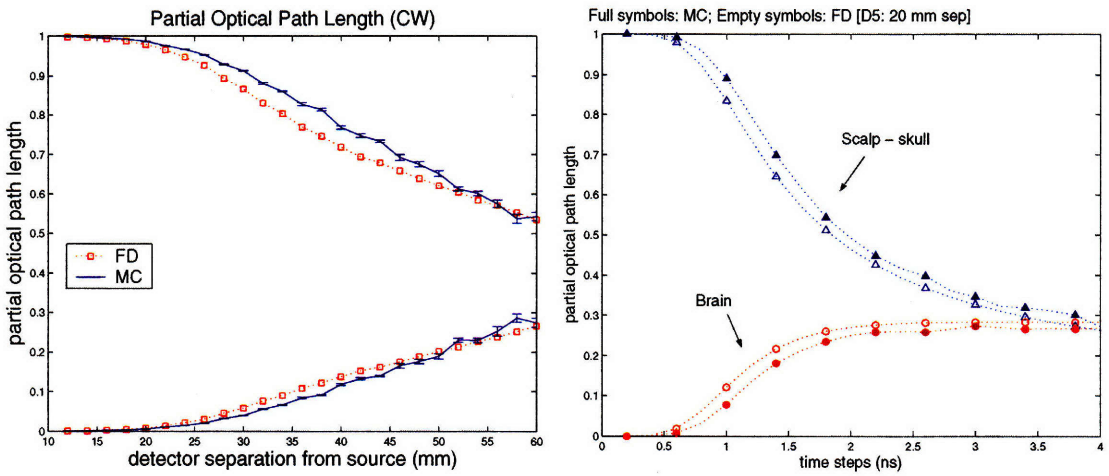


(a) (b)

Figure 3-2: Partial Path Length in continuous wave (a) and time-domain (b) for a source-detector separation of 20 mm: qualitatively the discrepancy between MC and FD appears small. PPL is calculated using $\Delta\mu_a$ 0.001 mm$^{-1}$.

veloping a reliable Finite Difference model are related to its simplicity, which is due to the simplified equation on which it is based: the consequent run time is reduced to a few minutes and the Signal to Noise Ratio (SNR) is generally higher because it does not closely model photons' paths outside the tissue (as does the Monte Carlo method).

However, Finite Difference programs are highly sensitive to Boundary Conditions (BC) accuracy [64] and introduces significant errors with segmented models with high absorption coefficients and/or weak or reduced scattering coefficients (as is the case with the clear CSF layer). The algorithm we use to implement Finite Difference is developed by Barnett et al. [13].

## 3.4 Results

We analyze fluence, fluence rate and partial path length predictions made by MC and FD, sometimes ranging CSF $\mu_s'$ value between 0.1 and 1.0 mm$^{-1}$ (see Figures 3-3a-b and Figure 3-4a-d). We compared FD measurements with MC using the formula (FD-MC)/MC, where MC is an optical measurement calculated solving the DOT forward model using Monte Carlo based algorithm [16], and FD is the same measurement obtained solving the Diffusion Approximation model of photon migration using Barnett et al.'s Finite Difference algorithm [13]. The qualitative analysis of PPL shown in Figure 3-2 suggests that MC and FD have quite similar sensitivity to absorption changes in the scalp-skull layer (top lines) and in the brain (bottom lines); we calculated the errorbars on Monte Carlo by estimating the standard deviation of the 11 Monte Carlo independent simulations.

The quantitative analysis of the total fluence (Figure 3-3a) and fluence rate (Fig-

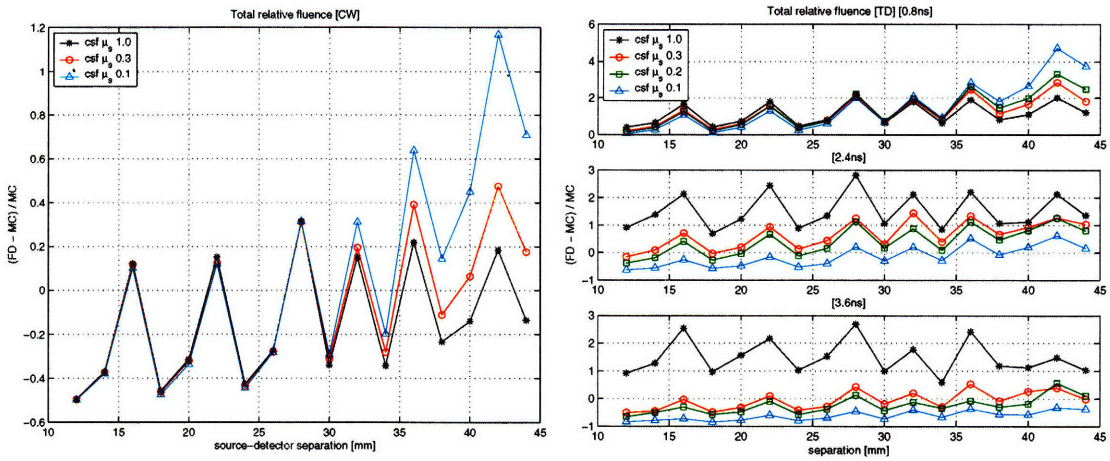


(a) (b)

Figure 3-3: Total fluence (a) and fluence rate (b) plots show a larger discrepancy between MC and FD, both in continuous wave and time-domain: deviation is within 40% in continuous wave for CSF $\mu_s'$ less than 0.3 mm$^{-1}$, whereas in time-domain the relative difference between the two DOT forward problem solvers is within 45% at a time delay of 2.4 ns and for source-detector separations up to 28 mm, but it becomes as large as 200% at earlier time steps and further source-detector separations.

ure 3-3b) show a larger discrepancy between MC and FD, both in continuous wave and time-domain: deviation is within 40% in continuous wave for CSF $\mu_s'$ less than 0.3 mm$^{-1}$, whereas in time-domain the relative difference between the two DOT forward problem solvers is within 45% at time delay of 2.4 ns and for source-detector separations up to 28 mm, but it becomes as large as 200% at earlier time steps and further source-detector separations. Note that for CSF scattering coefficient 1.0 mm$^{-1}$ the error increases, confirming our hypothesis that spinal fluid scattering coefficient can be approximated with the inverse of the straight line-of-sight through CSF (see Section 2.1).

The quantitative comparison of PPL predicted by FD and MC in continuous wave is shown in Figure 3-4a-b and in time-domain in Figure 3-4c-d for a head model with CSF $\mu_s'$ of 1.0 (model 1) and 0.1 mm$^{-1}$ (model 2). The figures present results similar to these reported in previous work [97, 98, 62, 54], but the discrepancy between FD and MC is smaller than previously stated. At the $14^{th}$ detector (36 mm from the source, the farthest reliable distance for a good SNR) we measure the largest difference (4.6%) on scalp-skull PPL for model 1 and 8.26% for model 2 using a $\Delta\mu_a$ increment of 0.001 mm$^{-1}$. In the brain, MC's and FD's largest discrepancies concentrate at smaller separation for model 1 (at 10 mm from the source the difference is 80%), whereas at 26 mm from the source we have the largest discrepancy for model 2 (where we calculate a difference of 50%). The discrepancy between MC and FD is greater in the brain than in the scalp-skull (max 80% versus max 8.3% in scalp-skull) due to the weaker SNR in the brain and perhaps also to the presence of CSF, and the discrepancy between models is also greater in the brain due to the presence of

the CSF transparent layer. Error bars shown in Figure 3-4a-d display the standard error calculated combining 11 independent MC run, each one simulating one hundred million photons.

The analysis of PPL in Time Domain (TD – DOT, Figure 3-4c-d) yields similar considerations: FD overestimates sensitivity to $\mu_a$changes in deeper tissues (CSF and brain) while it underestimates PPL in surface tissues (scalp and skull). However, we observe that MC and FD sensitivity to $\mu_a$ changes in the brain is relatively small in TD – DOT: from 80% discrepancy in scalp-skull at 0.8 ns, to 25% and smaller after 1.4 ns; in the brain, MC and FD never show discrepancies larger than 12% (mostly between 0% and 6%).

Observing the qualitative response of MC and FD in continuous-wave and time-domain we conclude that diffusion based methods can well predict photon scattering through biological tissues in a complex 3D geometry. We observe a 37.5% difference in PPL in continuous wave at a source-detector separation greater than 32 mm (which is a distance where light probes the brain layers) for a CSF $\mu_s'$ of 0.1 $mm^{-1}$ and an even smaller PPL difference in time-domain, between 28.4% and 13.3%, at source-detector separations between 12 and 35 mm and time steps later than 1.8 ns (source-detector separation of 12 mm shown in Figure 3-4d).

## 3.5 Conclusions

Through qualitative and quantitative studies we established the limits of Finite Difference predictions: when a tissue is too weakly scattering it becomes harder for Finite Difference to accurately predict photon's migration into the medium. Boundary conditions play an important role in diffusion based method's accuracy and they can still be improved to better approximate the effect of light scattered outside the medium. Testing Finite Difference with several lattice resolutions proved that a more accurate segmented head model, with a less rough surface, can greatly improve the data (increasing the algorithm computational cost with the risk of running out of memory). Time Domain data have the advantage of preserving explicitly the time and space dependency of the data. Therefore, when we lose the time dependency in continuous-wave data (obtained by integrating time-domain data over time) we are penalized by early times and late times outliers mostly due to poor SNR (signal detected at deep tissues like brain is weak) and diffusion inaccuracy at early times. Time-domain data give us the chance to select the data point more significant and less affected by artifacts. It remains to explore the effect that the measured discrepancy of the two forward models has on the inverse problem, which is, when restoring the optical properties of the head.

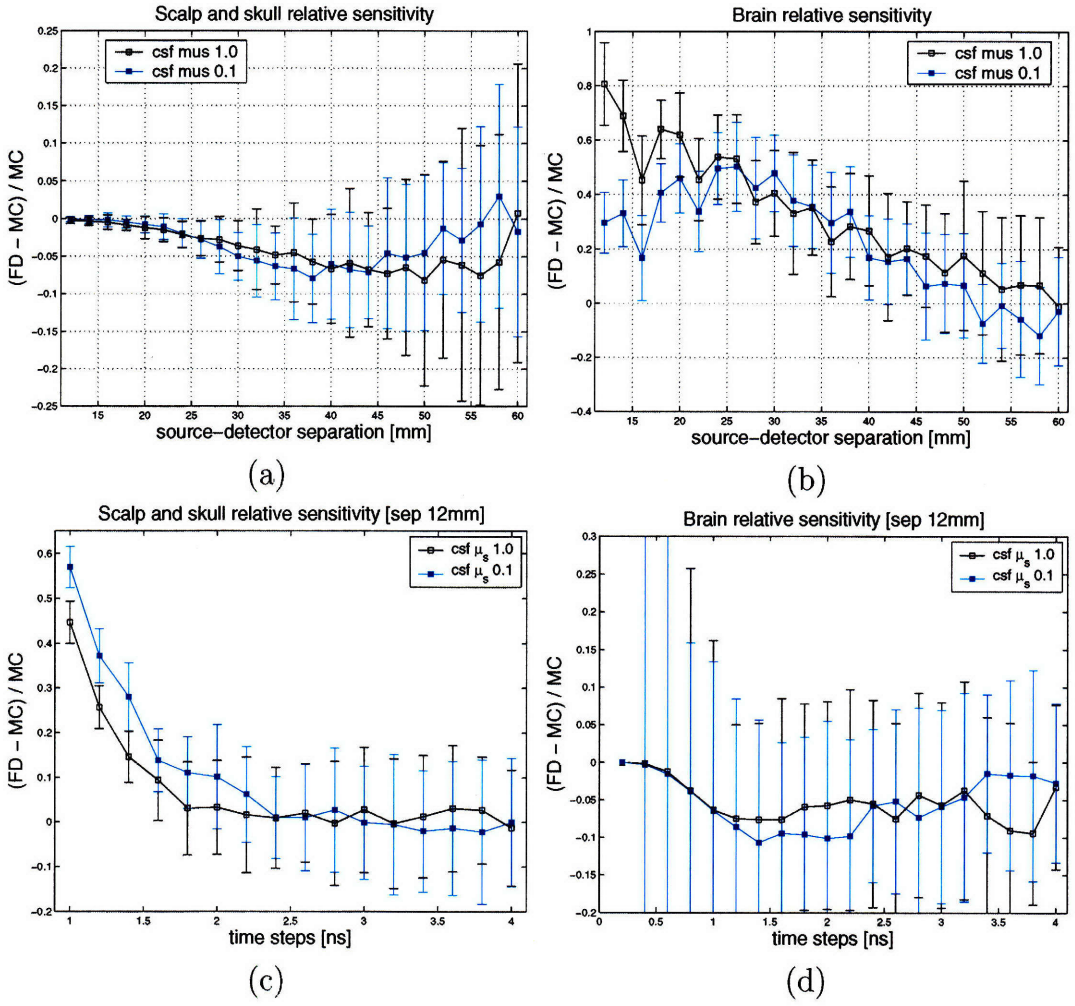


Figure 3-4: (a) Relative sensitivity to absorption changes in scalp and skull in continuous wave. The plot shows that where MC SNR is strong enough (small error-bars) the percentage discrepancy between MC and FD is very small. (b) Relative sensitivity to absorption changes in the brain in continuous wave. Larger error-bars due to weaker signal reaching deeper tissues. Larger discrepancy between MC and FD at small separation. (c) Quantitatively, MC and FD exhibit little disagreement in sensitivity to absorption changes in scalp and skull at later time. At early time sensitivity of the two methods is small due to weak signal. The discrepancy measured is almost always within the error bars. (d) FD is less sensitive to absorption changes in the brain than MC. In the brain FD and MC measure little disagreement at later time. At early time the signal is zero: no photons coming from the brain have been yet detected. Error bars display the standard error calculated combining 11 independent MC run, each one simulating one hundred million photons.

# Chapter 4

# Scalp Landmark based Registration using 10-20 coordinates ($\mathbf{SLR}_{10-20}$)

In this chapter we describe a method to register an atlas head to a specific subject's head based on scalp superficial landmarks, and we validate it against the subject's anatomical MRI (our ground truth) and against the commonly used Statistical Parametric Mapping (SPM) registration method [3], based on the analysis of the source's and target's anatomical MRIs.

Diffuse Optical Tomography images the change in blood oxygenation due to the increase of Cerebral Metabolic Rate of Oxygen ($CMRO_2$) coupled with the larger increase of Cerebral Blood Flow (CBF) [87]. The variation of oxygenation is a vascular side effect of increased neural activity, however the neurovascular coupling is still under investigation [36, 85, 116]. fMRI Blood Oxygen Level-Dependent (BOLD) signals also measure the magnetic effect of the increased level of oxygen in the brain capillaries, offering very accurate spatial maps of active cortical regions. Unfortunately, it is impossible to create detailed neural activation time-course maps because of BOLD's low temporal resolution (on the order of seconds) [52].

The main benefits of DOT are its high temporal resolution, its low cost and portability as well as good hemodynamic specificity as it offers the opportunity to quantitatively image three-dimensional spatial variations in total hemoglobin concentration (proportional to Cerebral Blood Volume by product of hematocrit, which is the proportion of blood volume that is occupied by red blood cells) and oxygen saturation. Optical tomography is well suited for monitoring brain activity for extended periods of time in unconstrained environments, making it a perfect tool for behavioral and brain development studies. Some of these benefits, though, can not be exploited because the MR subject's head anatomical scan is needed for solving the DOT forward model (see Section 1.1.4). One way to avoid this problem is to use a suitable anatomical head template (atlas) to approximate the subject's true anatomical model. The most relevant anatomical features affecting the photon migration forward model are the head size and orientation, the thickness of Cerebral Spinal Fluid (CSF) and skull (see Section 2.2), the cortical depth and the size and

orientation of cortical landmarks with respect to scalp landmarks. In order to ensure that the atlas matches these subject's anatomical features, we need to: (1) register the atlas to the subject using only the subject's head surface, while making sure that the registration does not impact significantly the correspondence of scalp and cortical landmarks, and (2), while not using the subject's anatomical MRI, infer the subject's CSF and skull thickness and modify the atlas accordingly. In Section 2.3 we address the problem of inferring CSF anatomical properties from personal information as one way to estimate CSF thickness.

Finally in Chapter 5 we integrate most of the results and methods described in previous chapters to achieve the ultimate goal of designing and testing an imaging protocol that uses solely Diffuse Optical Tomography to reconstruct brain activation. For this purpose we substitute the subject's specific anatomical model used in the DOT forward model with a general anatomical model (atlas) with a modified CSF thickness to best represent the subject's (see Chapter 2), and we use the $SLR_{10-20}$ algorithm described in this chapter to register the atlas to the subject's head. We complete our validation by presenting preliminary results on three experimental subjects.

## 4.1 The EEG 10-20 international system

In order to consistently record electroencephalographic (EEG) signals, a system was developed to describe the location of the electrodes on the human scalp in relation to the underlying corresponding cortical anatomical structures. For this purpose, the head was divided in regions: occipital (O), parietal (P), temporal (T), central (C), frontal (F) and frontal pole (Fp) (see Figure 4-1) and each point defined in this system was identified with the letter of the region to which it belongs followed by a number corresponding to the hemisphere location (even numbers for the right hemisphere and odd numbers for the left one, the smaller the number the closer the position of the point to the midline of the skull) or followed by the letter "z" when the point is on the midline. Historically, cadavers were used for testing, to ensure consistency and anatomical accuracy in defining the 10-20 points' locations.

### 4.1.1 10-20 system definition

A set of four main reference points is defined using known skull and visual landmarks; these points are: the bridge of the nose (called Nasion or Nz), the highest point of the external occipital protuberance at the lower rear part of the skull to which the ligamentum nuchae and trapezius muscle are attached (called Inion or Iz), the left and right pre-auricular points, sometime defined as the center of the lobe or as the center of the tragus or as the point of intersection between the helix and the tragus (see [77] for more details): these points are called A1 and A2 (or LPA and RPA). The rest of the points are defined in relationship of these four, as shown in Figure 4-2: each point is located at 10% or 20% of the distances between the four initial points or 10% or 20% of the circumference distances calculated measuring the skull circumference passing

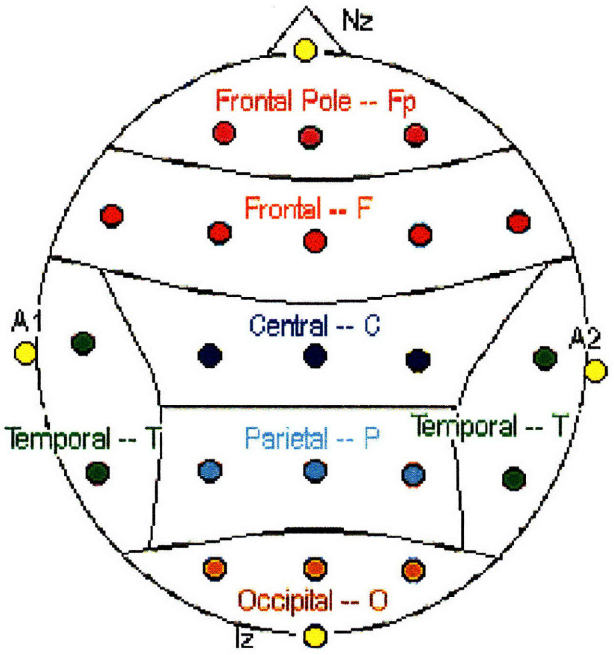


Figure 4-1: Division and naming of seven main head regions; typically the names given to scalp superficial landmarks (such as the EEG electrode systems), some cortical landmarks, cortical functional regions, and cortical parcellations relate to these seven regions for a clearer indication of their location on the human head. The colored circles mark the position of the 10-20 international system; in particular, the yellow circles indicate the locations of the four anchor points used to define the whole system (see Figure 4-2).

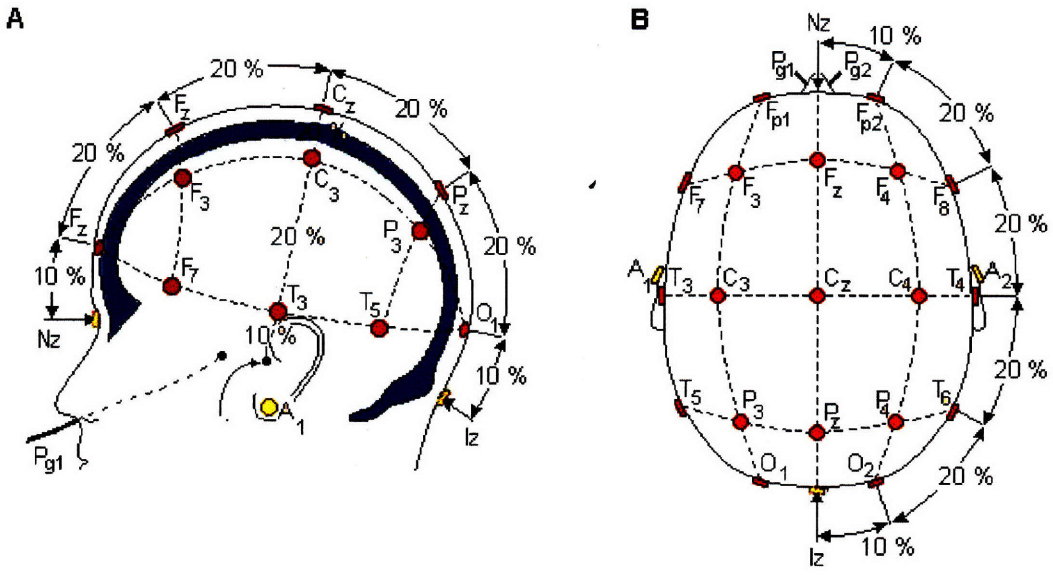


Figure 4-2: Pictorial description of the procedure to locate the points of the EEG 10-20 international system. The skull is shown in blue, as the Inion (Iz) point is defined as the highest point of the external occipital protuberance at the lower rear part of the skull. The red circles indicate the location of the 10-20 points, whereas the yellow circles are the locations of the four reference points (Nz, Iz, A1 and A2) in relation to which the reminder 21 points are calculated.

by previously located points (hence the name *10-20 system*). A percentage system allows flexibility over different head sizes and shapes while keeping the relationship between distances and landmarks on the scalp and on the cortical surface.

### 4.1.2 Virtual 10-20 system

The *International 10-20 Electrode Placement System* has the advantage of defining a standard terminology and measurement format as well as anatomically dependent electrode locations. Another advantage of using the 10-20 international system is that a subject can be tested in different facilities and using different measurement systems, and the measurements can be easily co-registered as long as they are expressed as a function of the 10-20 reference points. The 10-20 point locations are calculated on a physical head using a measuring tape or a 3D digitizer; however, when the anatomical MRI of a subject is the only data available, it is possible to find the 10-20 locations using a geometric algorithm developed by Prof. Ippeita Dan's group [76]. The algorithm extracts the scalp mesh from the MRI intensity image and uses the Nz, Iz, A1 and A2 as input points (see Section 4.1.1) to calculate the remaining 10-20 locations. The four initial points are manually found on the anatomical MRI using the definition and guidelines from [77]. This algorithm can be used to calculate the 10-20 markers' locations as long as a scalp mesh and the Nz, Iz, A1, A2 points are specified. The electrode system and the virtual algorithm can be modified to include

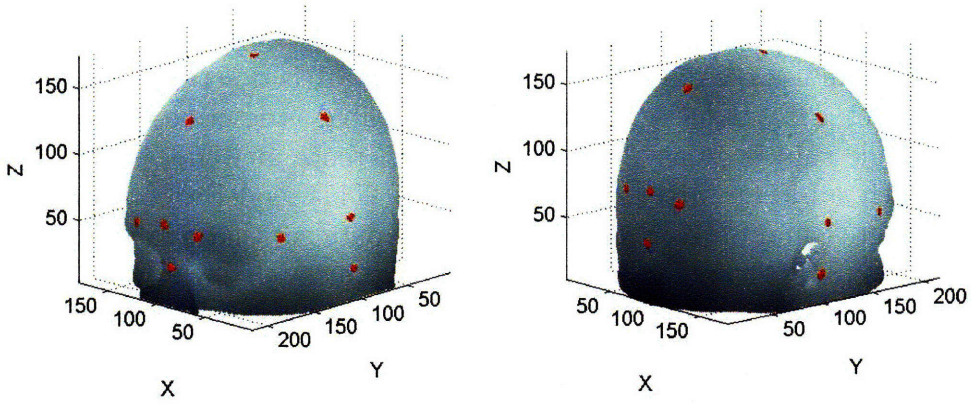


Figure 4-3: The locations (red dots) of 19 of the 21 10-20 points (two are discarded for lack of reproducibility) as calculated by the virtual 10-20 algorithm [76] on the MNI single subject atlas (gray surface). Similarly to the manual procedure to define the 10-20 system, the virtual 10-20 algorithm uses 4 initial points (Nz, Iz, A1, A2) manually defined on a subject's head surface (in our case we located these points on the surface of the subject's anatomical MRI) to determine the distance-curves connecting them and the 10 and 20% of these distance-curves. For this purpose, a plane is defined using three landmark positions at a time, extracting head surface points which comprise a crossection between the plane and the head surface, and drawing a distance-curve utilizing the extracted points (see Jurcak et al. [76] for more details).

additional electrodes (5% increments) [77, 101].

For our studies we use a modified version of the standard 10-20 system (see Figure 4-3). We selected the 19 points that best cover the functional regions we are interested in imaging. We needed at least 12 points to estimate the 12 parameters of our registration algorithm, and we selected the 19 most stable points of the 21 provided by Jurcak's algorithm [76]. This landmark system was also used to find anchor points to define the optical virtual probe used to simulate photon migration on our subjects' dataset (see Section 5.2.2 and Figure 5-6).

## 4.2 Methods

The methods (described in details below) can be summarized as follows: the dataset comprising of 32 healthy subjects' MRIs and the MNI single subject atlas is used to generate our measurements, and two registration methods are used for comparison. The criteria used to validate the registration methods are based on their intended application, which is that of projecting the physical probe from the subject scalp to the atlas synthetic scalp and then simulating photon migration on the atlas anatomical model.

### 4.2.1 Dataset

For this study we use the dataset of 32 anatomical MRIs described in Section 2.3.1. For each subject, a five tissue segmentation is calculated as described in Section 2.3.2.1. The MNI single subject atlas [25] is used as a reference anatomical MRI to be registered to each subject's MRI (same as in 2.2.1). This model is constructed from a high-resolution (1 mm isotropic voxels) low-noise data set that was created by registering 27 scans (T1-weighted gradient echo acquisitions with TR/TE/FA = 18 ms/10 ms/30 deg) of the same individual in stereotactic space where they were sub-sampled and intensity averaged [66]. The volume contains 181x217x181 voxels and covers the brain completely, extending from the top of the scalp to the base of foramen magnum. A five tissue labeled model was derived from the nine tissue types model available form BrainWeb [2, 25] by re-labeling connective tissue, fat, muscle/skin as skin, and glial matter as white matter (brain). The resulting discreet model is a volume of 181x217x181 $mm^3$ voxels.

### 4.2.2 Scalp mesh extraction

For each subject MRI and the atlas MRI we transform the intensity volume (3D array of integers indicating the intensity threshold of each spatial volumetric unit, or voxel) into a binary volume (air labeled 0 and non-air labeled 1). We then identify the boundary voxels by shifting the binary volume up-down and right-left on each plane $xy$, $yz$ and $xz$ and subtracting the shifted and the un-shifted volumes. Thus, we obtain a list of boundary voxels that we transform into a list of 3D coordinates by expressing each $(i, j, k)$ matrix-coordinate into Cartesian $(x, y, z)$ coordinates where the origin is the voxel $(1, 1, 1)$ and the axis are positively oriented.

### 4.2.3 10-20 based transformation

In order to estimate the 12 parameters of the 3x4 affine transformation we proceed as follows:

1. manually find the four anchor points, Nz, Iz, A1 and A2 (see Section 4.1.1) on each subject and the atlas MRIs;

2. apply the virtual 10-20 algorithm [76] to each mesh and relative four anchor points and obtain the 19 locations of the 10-20 points for each subject ($P_{rw}$, which is a [4x19] matrix, as the points are expressed in the homogeneous coordinate system) in the subject's real world coordinate system, as well as for the atlas ($P_{mni}$) in MNI space (which is the atlas space); $P_{mni}$ is a [3x19] matrix and each row $i$ represents the 3D coordinates of the $i^{th}$ 10-20 point on the atlas;

3. given that $P_{mni} = T * P_{rw}$, we estimate $T = P_{mni}/P_{rw}$, where the 3x4 transformation matrix $T$ is the least square solution of the overdetermined linear system.

### 4.2.4 Volume-based affine transformation

We use the Statistical Parametric Mapping (SPM5) normalization toolbox [3, 51] to estimate the volume-based affine transformation between the subject MRI and the atlas MRI. We use SPM5's well known registration method for validation purposes as SPM5 is broadly used in the MRI community as a reliable and accurate registration tool. The SPM5 affine normalizer estimates the affine transformation parameters using a MAP (Maximum A Posteriori) Bayesian approach [51] that converges to a mean square error of less than 0.2 in typically less than 70 iterations (run time is approximately 2 minutes). SPM5 outputs the estimated volumetric affine transformation matrix $M$.

### 4.2.5 Data generation

After estimating the two affine transformation matrices, $T$ and $M$, we proceed by applying the matrices to the subjects' meshes and volumes. Note that our ultimate goal is to register, using $\text{SLR}_{10-20}$, the atlas anatomical MR to a given subject scalp; however, for this study, we focus on validating our registration method against the SPM5 registration method [3] and for the most part we do so by expressing our measurements in the standard MNI space. For this reason, most of our validations refer to the registration applied to the subjects' MR and mapping them into atlas/MNI space. However, for our last validation point, the cortical landmarks preservation (Section 4.3.5), we measure agreement in subject space, using $T^{-1}$ to map the atlas into subject's space.

The subject's mesh is registered to the atlas simply by applying the transformation matrices to the subject mesh points: $\text{mesh}_{mni,spm} = \text{mesh}_{rw} * M$ to transform the subject's mesh ($\text{mesh}_{rw}$) to atlas/MNI space using the SPM5 method; $\text{mesh}_{mni,slr} = \text{mesh}_{rw} * T$ to transform the mesh using the parameters estimated from the 10-20 points. The subject's volume is registered to the atlas by applying the SPM5 re-slicer tool and using either the $M$ or $T$ matrix as input: $\text{vol}_{mni,spm} = \text{reslice}(\text{vol}_{rw}, M)$ and $\text{vol}_{mni,slr} = \text{reslice}(\text{vol}_{rw}, T)$ respectively. The method used to re-sample the output MRI image (or volumes) in the new stereotactic (or MNI) space is trilinear interpolation (which is a 3D tensor B-spline interpolation of order 1), which is the most accurate but slower interpolation method offered by the SPM5 toolbox [3]. The nearest neighbor interpolation is used for the segmented images (which are volumes of integer labels). We also transform the 19 10-20 locations found on each subject into the MNI coordinate system: $P_{mni,spm} = P_{rw} * M$ and $P_{mni,slr} = P_{rw} * T$.
For the data shown in Section 4.3.5, instead, these equations are applied: $\text{mesh}_{rw,slr} = \text{mesh}_{mni} * T^{-1}$ for the meshes, and $\text{vol}_{rw,slr} = \text{reslice}(\text{vol}_{mni}, T^{-1})$ for the volumes, using $\text{SLR}_{10-20}$.

## 4.3 Validation of $SLR_{10-20}$ method

To best guarantee the successful substitution of head models in the forward process, we measure the performance of our registration algorithm and compare it to that of the well known, MRI-volume-based algorithm available in the SPM5 toolbox [3]. The most relevant measures of accuracy are: (A) displacement of scalp landmarks (Section 4.3.2); (B) change of cortical depth (Section 4.3.3); (C) change of CSF thickness (Section 4.3.4) and (D) displacement of cortical landmarks (Section 4.3.5). We compare measures A-C against the well known and widely used SPM5 volumetric registration algorithm, and we validate D measures against the same measurements on the unregistered subjects (our ground truth).

### 4.3.1 Mesh and volumes comparison

#### 4.3.1.1 Meshes

In Figure 4-4 we show the scalp meshes of one subject head registered to the MNI atlas using superficial landmarks (in blue) and the full volumetric data (using SPM5 toolbox) (in the orange shade). The atlas scalp is outlined in gray. The plot shows two different views (top and bottom) to highlight the differences of the scalp shapes. In general, both registration methods minimize the differences in the upper part of the scalp whereas more discrepancies are found below the plane where the nose bridge and the ears lay. It is possible to notice that the volumetric registration is less accurate in matching scalp size and shape in the frontal region, generating a wider head. This is expected since the SPM5 toolbox affine registration algorithm starts by minimizing differences in overall head size, orientation and shape, and then focuses on minimizing differences between brains.

#### 4.3.1.2 Volumes

A single subject's registered head volume is compared in Figures 4-5a-d. In Figure 4-5a are shown coronal, sagittal and transverse slices passing through the Anterior Commissure (AC) point (see Section 2.3.2.2 and Figure 2-14) of the subject head registered to the MNI atlas using scalp landmarks ($SLR_{10-20}$). The AC point falls in the intersection of the crossbars. Figure 4-5b shows the corresponding slices of the subject head registered using SPM5 volumetric affine registration tool. Another two transverse slices (35 and 19) are shown in Figure 4-5c and Figure 4-5d for $SLR_{10-20}$ and SPM5 registration respectively. The red crossbars intersection points in these figures highlight the differences between the two registration algorithms: in the SPM5 registered head, the red lines junctions fall on top of the scalp, whereas in the $SLR_{10-20}$ registered head the crossbars intersections fall few millimeters outside the scalp, suggesting that the volumetric-based registration results in a slightly larger head size than the $SLR_{10-20}$ registration. We will show further evidence that the overall head size is best preserved by $SLR_{10-20}$ (see also the mesh plots in Figure 4-4), whereas the brain size is more accurately represented using SPM5.

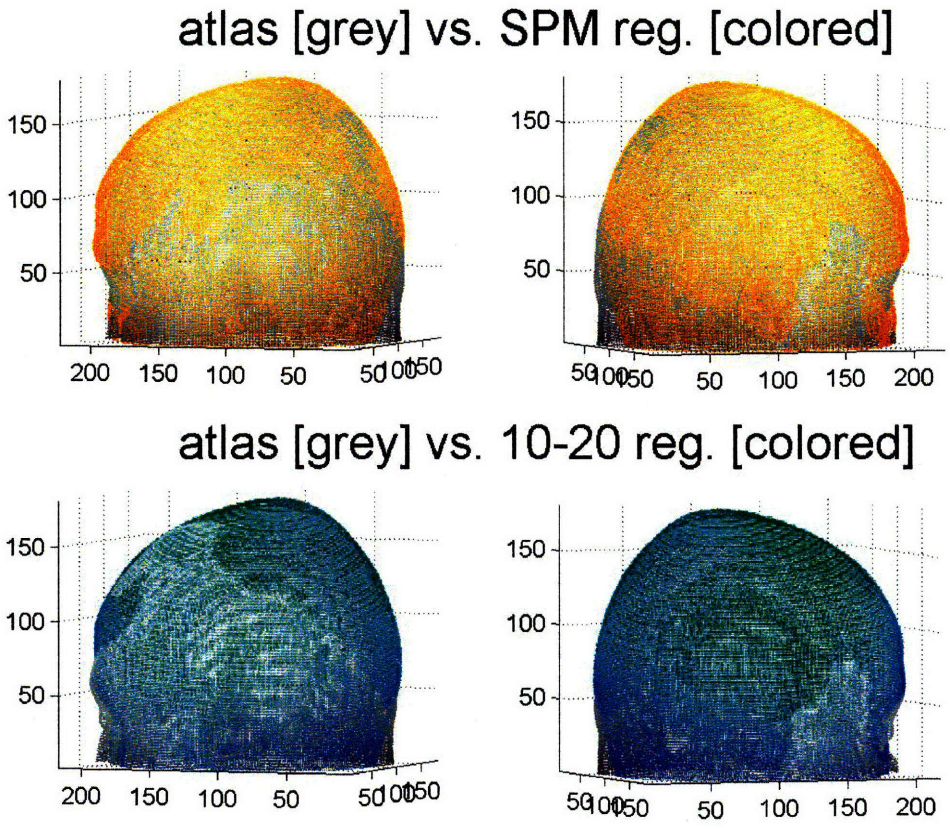


Figure 4-4: Comparison of $SLR_1$0-20 (blue) and SPM5 (yellow) registrations of a subject's scalp points to the MNI atlas scalp (gray). The plot shows two different views (top and bottom rows) to highlight the differences in scalp shapes. In general, both registration methods minimize the differences in the upper part of the scalp whereas more discrepancies are found below the plane containing the bridge of the nose and the ears. One may notice that the volumetric registration is less accurate in matching scalp size and shape in the frontal region, generating a wider head.

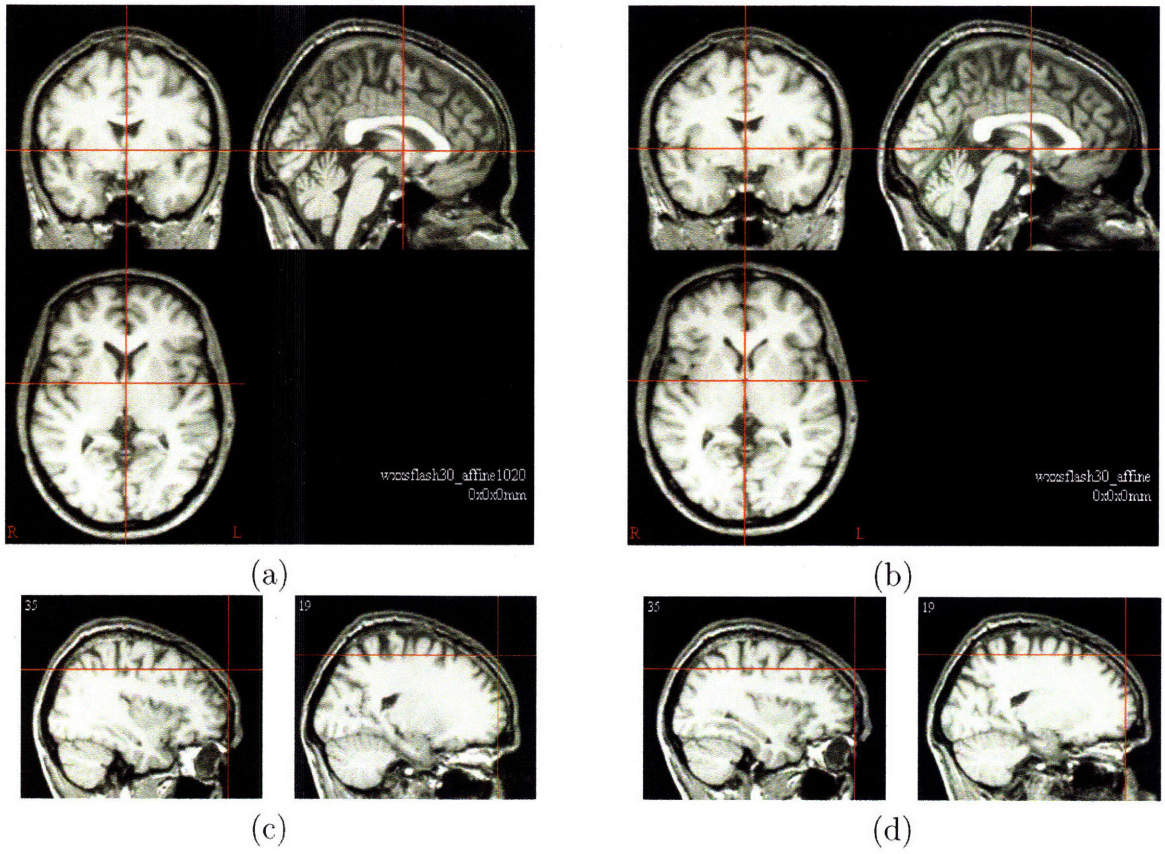


Figure 4-5: (a) Three slices, coronal, sagittal and axial (or transversal), of a subject's MRI volume registered to the MNI atlas using $SLR_{10-20}$; (b) corresponding three slices from (a) but here SPM5 is used to register the subject's head to the atlas'. The intersection of the red crossbars indicates the location of the Anterior Commissure (AC) point on the two registered volumes. (c) Two other sagittal slices ($x = 35$ and $x = 19$) for the $SLR_{10-20}$ and (d) for the SPM5 registration algorithm. The red crossbars intersection points in these figures highlight the differences between the two registration algorithms: in the SPM5 registered head, the red lines junctions fall on top of the scalp, whereas in the $SLR_{10-20}$ registered head the crossbars intersections fall few millimeters outside the scalp, suggesting that the volumetric-based registration results in a slightly larger head size than the $SLR_{10-20}$ registration.

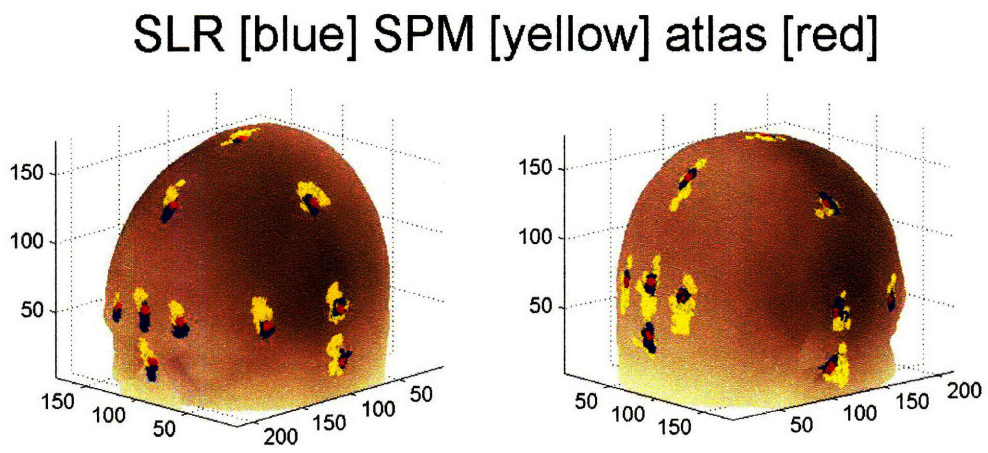


Figure 4-6: Over the atlas head surface mesh are plotted the locations of the atlas' 10-20 landmarks (red) as calculated by the virtual 10-20 algorithm [76]. In yellow are marked the locations (for all subjects) of the same 10-20 points as calculated by mapping the red points into MNI space using SPM5 affine transformation; in blue the 10-20 points locations as found on the 32 subjects registered to the atlas using $SLR_{10-20}$. It is easy to note that the yellow points are generally farther from the red points, suggesting that SPM5 does not preserve scalp landmarks as well as $SLR_{10-20}$.

### 4.3.2 Probe placement preservation

If the registration algorithm preserves scalp landmarks we are guaranteed to minimize probe misplacement when we map the optode's physical coordinates on the subject's scalp to their virtual locations on the atlas.

We transform the 10-20 points using the affine transformations $T$ and $M$ as described in Section 4.2.5 to calculate the misplacement of the 10-20 reference points due to the application of a registration algorithm ($SLR_{10-20}$ and SPM). Figure 4-6 shows the misplacement of the 10-20 location as a result of the two different registration techniques. In pink is displayed the MNI atlas mesh (front view and back) and the position of the 10-20 points are plotted over it. Our reference is the location of the 10-20 points as calculated by the virtual algorithm [76] on the MNI atlas; the yellow dots represent the location of the 10-20 points in each subject mapped into MNI space using the SPM volumetric algorithm, whereas in blue are shown the locations of the 10-20 points on the subjects registered using $SLR_{10\text{-}20}$. Both registrations are transforming the subjects' heads into MNI space but it appears that $SLR_{10\text{-}20}$ more accurately maps scalp mesh points from subject space to MNI space.

In Figure 4-7 the numerical representation of the mean Euclidean distances between the 10-20 location on the registered subjects and the corresponding reference locations on the atlas is shown: blue circles for the $T$-transformed points and red stars for the $M$-transformed points. In the plot is also shown the max, mean and standard deviation of the population mean distances over all the 10-20 points. As expected, the 10-20 based registration algorithm generates a much smaller landmark displacement

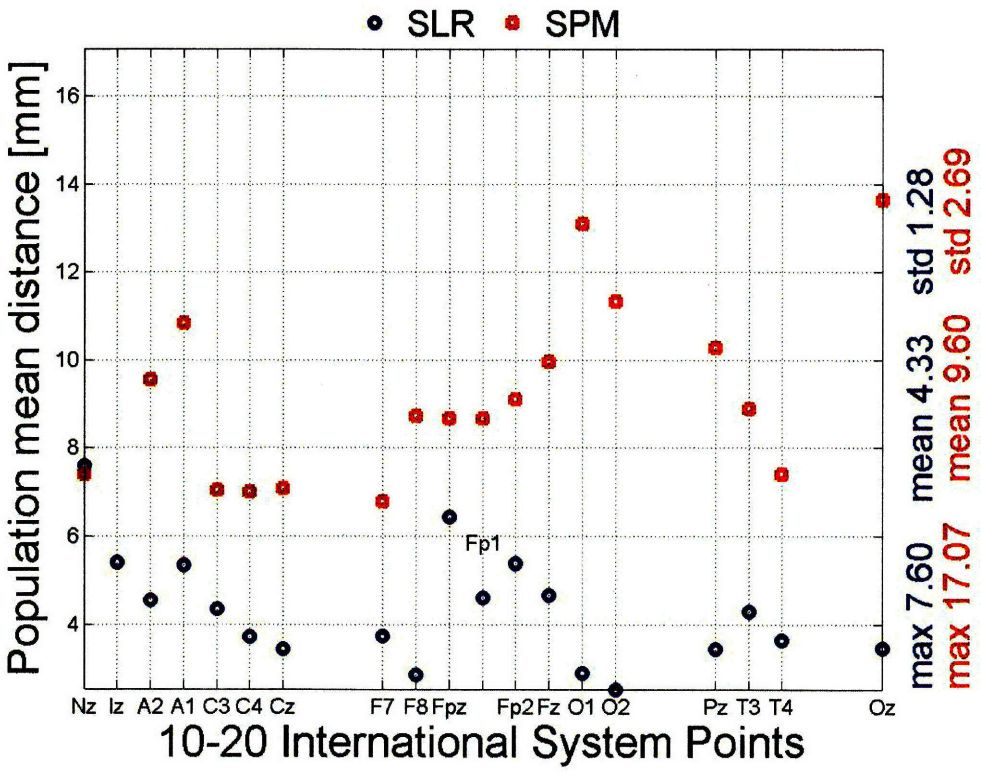


Figure 4-7: Population mean Euclidean distance between the 10-20 locations on the registered subjects and the corresponding "true" locations on the atlas (the red dots of Figure 4-6). The distances calculated for the subjects registered to the atlas using SPM5 are plotted in red, and the blue circles are used for $SLR_{10\text{-}20}$. On the right side of the plot are reported the max, mean and standard deviations over all the 10-20 points (red text for SPM5 and blue text for $SLR_{10\text{-}20}$). Our surface-based registration algorithm performs better than SPM, with displacement errors less than 5.8 mm (except for Nz and Fpz that suffer from across-subjects frontal pole anatomical variability), as oppose to SPM errors of over 7 mm. The results are not surprising since $SLR_{10\text{-}20}$ minimizes the alignment of the 10-20 locations on a source and target's scalp meshes.

(mean distance over 32 subjects is not greater than 7.6 mm, averaging 4.33, whereas the volumetric registration gives rise to mean distances as large as 17.07 mm, averaging 9.6 mm). This is because the 10-20 based registration estimates the transform $T$ by minimizing the distance of the 10-20 points on the registered subject's heads and their correspondent points on the MNI atlas (see Section 4.2.3); therefore, the mean Euclidean distance figure plots the residual error, which is small.

### 4.3.3 Cortical depth

The cortical sensitivity of DOT measurements is strongly sensitive to the cortical depth beneath the scalp surface. Here we estimate the variation in this depth between the atlas and the subject's head registered to the atlas. In Figure 4-8a-b we show the variation of cortical depth due to the landmark and volumetric registrations. Figure 4-8a displays the cortical depth maps for one subject: the colors and associated Matlab colorbars indicate the scalp-cortex Euclidean distances in mm sampled at each mesh point. The difference seems negligible, as confirmed in Figure 4-8b, where the difference between the registered subject's and the atlas cortical depths are displayed as function of subject's age (blue circles for subjects registered to the atlas using $\text{SLR}_{\text{10-20}}$ and red stars for SPM5). In other words, these differences are calculated as: $(\text{MedianCD}_{slr} - \text{MedianCD}_{\text{atlas}})$, where $\text{MedianCD}_{slr}$ is calculated on each registered subject by projecting each surface mesh point toward the AC point (roughly the center of mass of the brain, see Section 2.3.2.2) and tracking the distance traveled until encountering the first cortical voxel and finally taking the median of the calculated distances from all the surface mesh points. Similarly, $\text{MedianCD}_{\text{atlas}}$ is the median of the cortical depths measured on the atlas. Likewise for SPM5 registration (red stars) is used the formula: $(\text{MedianCD}_{spm} - \text{MedianCD}_{\text{atlas}})$, where $\text{MedianCD}_{spm}$ is the median depth calculated on subjects registered using SPM5. Mean, max and standard deviation of these differences are reported on the right side of the plot. In average both registration methods perform well ($-0.01$ mm average difference when using landmark registration and 0.5 mm when using volumetric registration); the $\text{SLR}_{\text{10-20}}$ algorithm has a slightly better score (smaller mean and max difference and smaller data spread).

### 4.3.4 CSF thickness

Photon migration is particularly sensitive to CSF thickness [29]; therefore is important that the head model used in the photon migration simulation accurately represents the subject's CSF thickness. The CSF thickness differences are calculated analogously to the cortical depth difference (see Section 4.3.3) with CSF thickness instead of cortical depth: $(\text{MedianCSF}_{slr} - \text{MedianCSF}_{\text{atlas}})$, where $\text{MedianCSF}_{slr}$ is calculated by taking the median over the sampled mesh points of the number of millimeters traveled in CSF in the direction of the Anterior Commissure and similarly for the differences relative to SPM5 registration measurements. In addition, at each data point the subject's age is shown. In Figure 4-9a the CSF thickness map of a subject is displayed. The colors and associated Matlab colorbars indicate CSF thickness

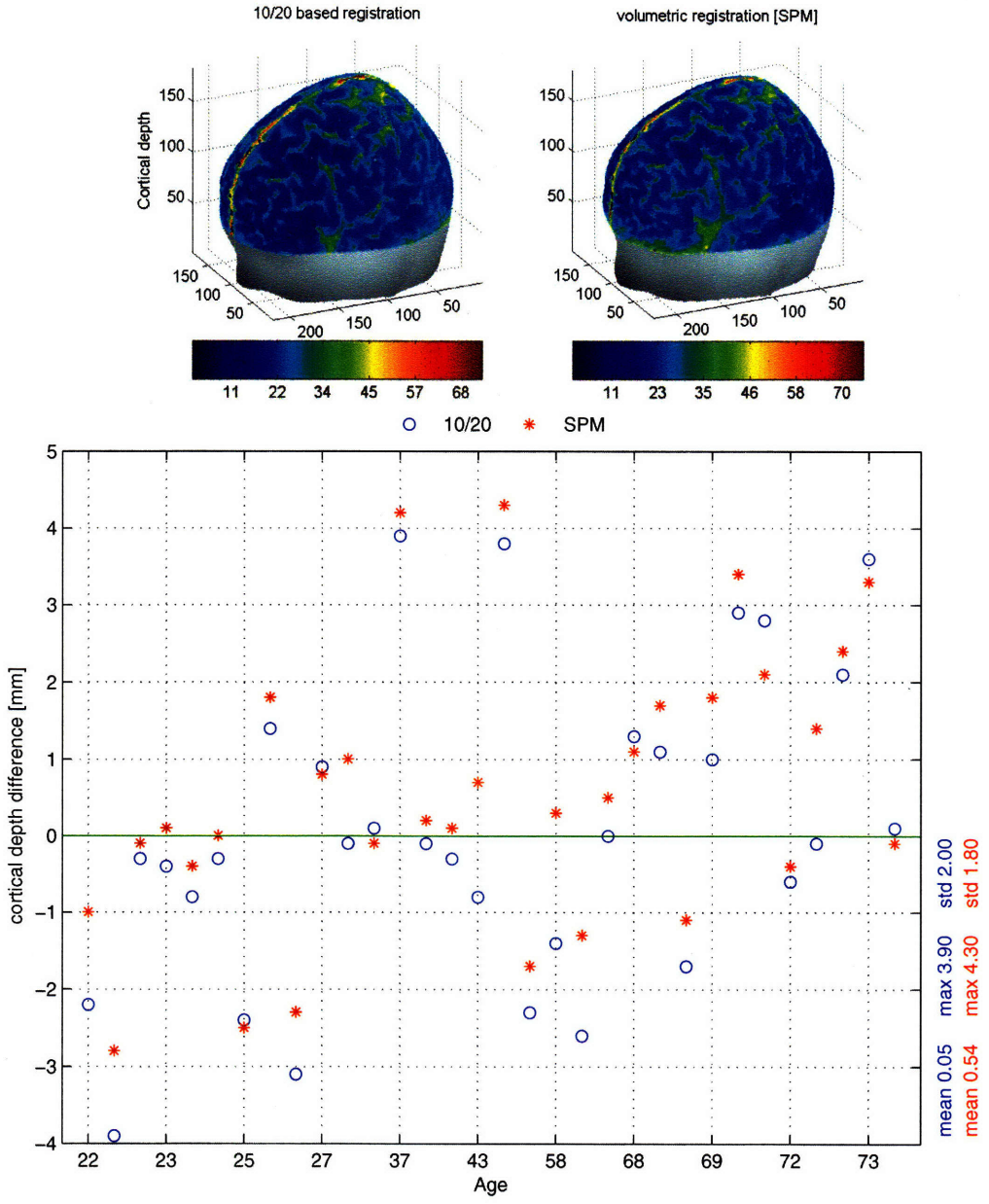


(a)

(b)

Figure 4-8: (a) Cortical depth maps on one subject: the colors and associated colorbars indicate the scalp-cortex Euclidean distances in mm sampled at each mesh point. The difference seems negligible, as confirmed plot (b), where the difference between the registered subject's and the atlas cortical depths are displayed as function of subject's age (blue circles for subjects registered to the atlas using $SLR_{10\text{-}20}$ and red stars for SPM5). Mean, max and standard deviation of these differences over all the subjects are reported on the right side of the plot (red text for SPM5 and blue for $SLR_{10\text{-}20}$). In average both registration methods perform well ($-0.01$ mm average difference when using landmark registration and 0.5 mm when using volumetric registration); the $SLR_{10\text{-}20}$ algorithm has a slightly better score (smaller mean and max difference and smaller data spread).

in mm. Little differences are noticeable from these maps which suggests that the two registration methods have similar performances. Only by looking at the CSF thickness difference plot of Figure 4-9b do we realize how poor this performance is: the differences are as great as 4 mm (which is 190% of the atlas median CSF thickness, 2.2 mm) with oscillations of 1.3 mm (or 60% of the atlas median CSF thickness). This result, although not encouraging, is not at all unexpected: as shown in Section 2.3, CSF thickness varies significantly across population as a function of age (60% CSF thickness changes between subjects under 30 and subjects over 65 years old from Figure 2-16 and 5-5) and Figure 4-9b confirms these findings (75% of the subjects within $\pm 50\%$ error are between 22 and 43 years old; note that the atlas is a 37 year old male). Therefore, it is important to take into account the CSF thickness and modify the atlas based on the subject's age by dilating CSF into brain before proceeding with the registration.

### 4.3.5 Cortical landmark preservation

Substituting the subject's anatomy with an atlas' in the DOT forward model entails (1) mapping the physical probe from the subject's world to the registered atlas' (as done in Section 5.2.2); (2) and modifying the registered atlas' CSF thickness to match that of the subject. This is because light propagation depends on the tissue types traversed, especially the amount of CSF (see Sections 4.3.4) and the distance between optodes and cortex (see Sections 4.3.3): our results show that scalp-cortical distance does not vary significantly across population (see Sections 4.3.3) but CSF thickness does; therefore, we need to modify the registered atlas' CSF thickness by dilating or eroding the spinal fluid layer (as done in Section 5.2.1). Another as important factor influencing the forward model is the cortical region probed by the injected light: we need to ensure that the regions of the physical brain reached by photons are matched by the virtual regions probed by the photons simulated on the atlas general head. To verify this, we calculate the location of 24 functional Region Of Interests (fROI) on each subject and compare them to these calculated on the atlas registered to each subject using $SLR_{10\text{-}20}$ (hence the measurements are in subject space).

#### 4.3.5.1 Cortical ROI calculation

The FreeSurfer toolbox [1] offers a series of routines for extracting 12 Region Of Interests per hemisphere on any given MRI [42, 47, 43]. The regions are: Brodmann Areas (or BA) 1, 2, 3a, 3b, 4a, 4p, 6, 44 and 45, V1 (or Brodmann area 17), V2 (or Brodmann area 18) and MT (or V5, which is part of Brodmann area 19) [22]. These areas (see Figure 4-10) cover most of the visual cortex (primary visual cortex V1, visual association cortex V2, middle temporal area, or MT), the pre-motor and motor cortex (BA6 and BA4a and BA4p), the primary somatosensory cortex (BA1, BA2, BA3a and BA3b) and the Broca's area (BA44 and BA45), responsible for speech and language [67, 93, 89, 103, 22].

In order to calculate the functional ROIs for each subject and registered atlas we need to warp the cortical surface [46] to a reference sphere on which these functional

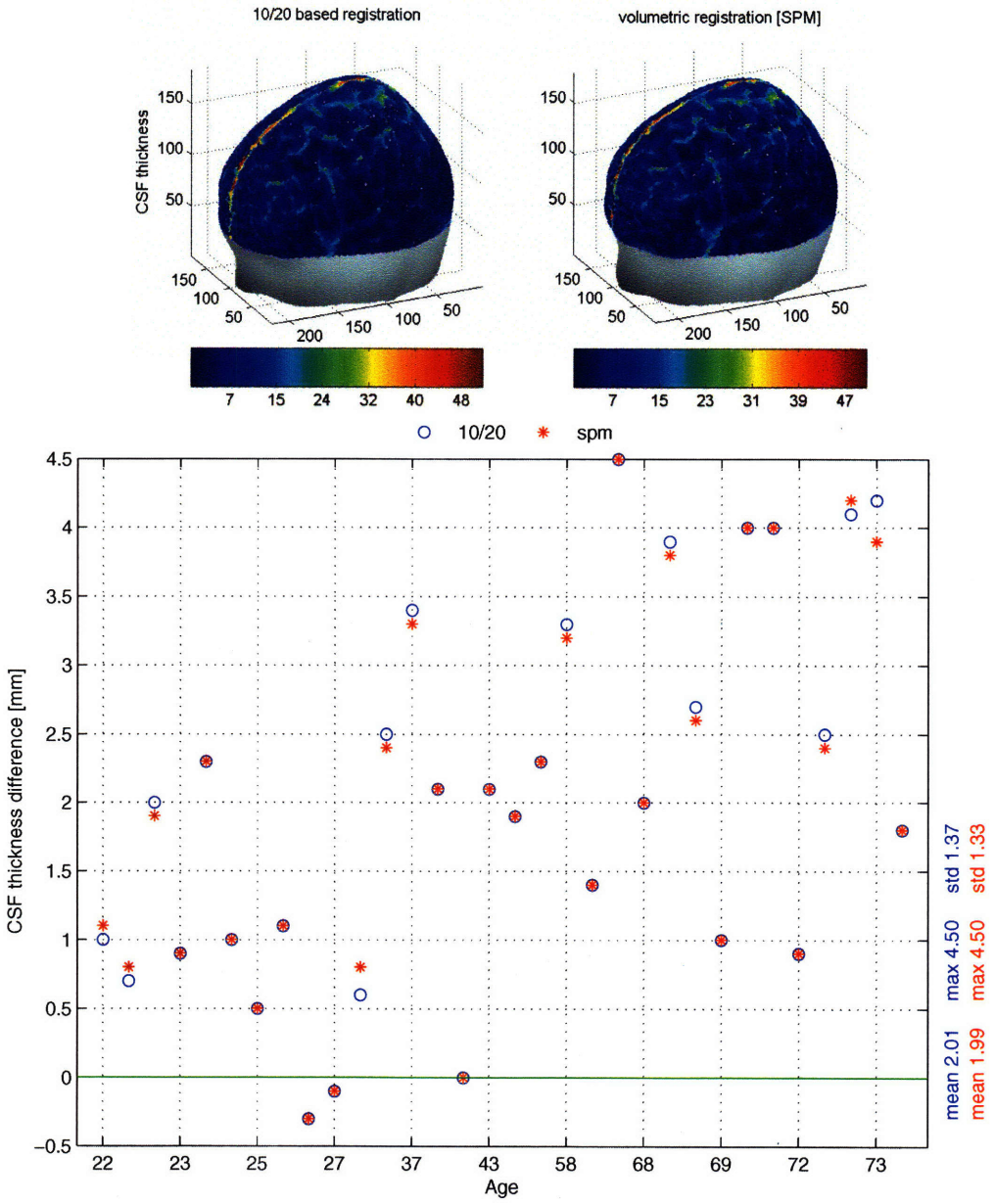


(a)

(b)

Figure 4-9: (a) CSF thickness map of a single subject; the colors and associated colorbars indicate CSF thickness in mm. Little differences are noticeable from these maps which suggests that the two registration methods have similar performances. However, from plot (b) we realize how poor this performance is: the differences are as great as 4 mm (which is 190% of the atlas median CSF thickness, 2.2 mm) with oscillations of 1.3 mm (or 60% of the atlas median CSF thickness). Mean, max and standard deviation of these differences over all the subjects are reported on the right side of the plot (red text for SPM5 and blue for $SLR_{10\text{-}20}$). These results, although not encouraging, were expected (see Section 2.3) as CSF thickness varies significantly across population as a function of age and plot (b) simply confirms this trend (75% of the subjects within $\pm 50\%$ error are between 22 and 43 years old; note that the atlas is a 37 year old male).

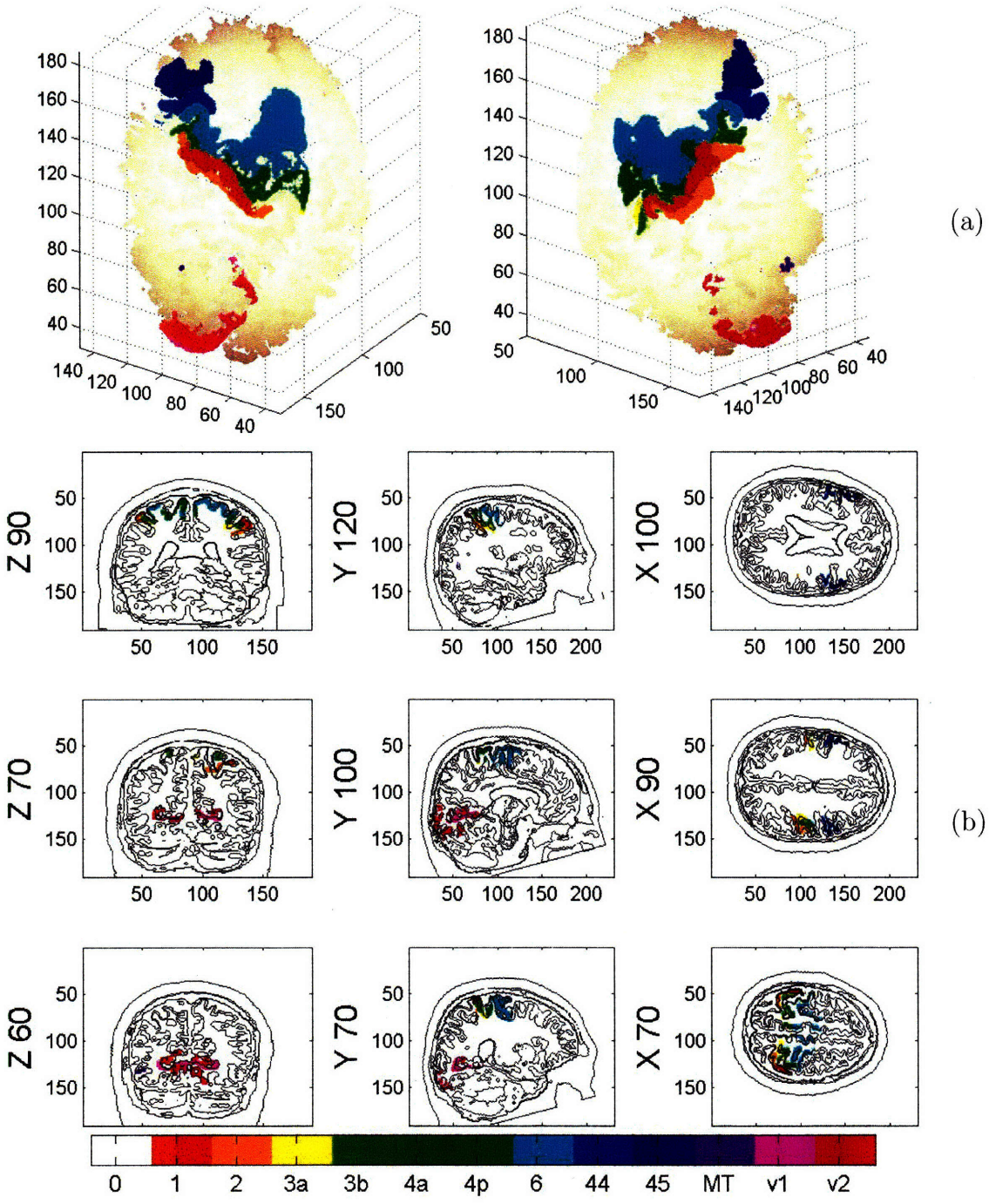


Figure 4-10: (a) Two views of the 24 functional ROIs (color) overplotted on the cortical surface mesh (light pink) of the MNI atlas registered to subject number 4 using $SLR_{10\text{-}20}$; note how small region MT is (dark purple) and how area 3a (yellow) is partially hidden under area 1 (red) and 2 (orange). (b) Coronal, sagittal and axial slices of the registered atlas from (a): the five tissue types (scalp, skull, CSF, gray and white matters) are contoured in black and the 24 ROIs are colored as indicated in the colorbar. Note in coronal slice Z = 60 and sagittal slice Y = 100 how ventral the visual cortex V1 and V2 go; since optical measurements are more sensitive to superficial layers, we expect weak signal from ROIs that extend so deep in the cortical sulci.

ROIs are already defined. Hence, we map the functional ROI locations back to the original space, obtaining the cortical regions in subject space. The following steps are applied to each subject and each registered atlas:

1. The subject anatomical MRI is analyzed by FreeSurfer [1] and its cortical and subcortical surfaces are extracted and divided in right and left hemisphere,

2. The extracted cortical surface is warped to the spherical cortical surface of a reference average subject *fsaverage* [1], using a surface-based averaging technique that aligns cortical folding patterns [47, 46], over which are automatically labeled 12 gyral based functional regions per hemisphere [42]. These regions are transfered to the warped surface and then transformed back into the subject's space. At the end of this process for each ROI a text file is generated, listing the coordinates of the voxels belonging to the ROI and their assignment probability. The region of interests found are overlapping,

3. The lists of voxels are processed to eliminate repetition and overlapping. We developed an algorithm to merge the regions where voxels have probability values over 70% and select the voxels with the highest probability in the case of overlap. The resulting list of voxels is in the subject's brain coordinates and needs yet another transformation to be in subject space,

4. The ROIs defined so far are a list of the voxels belonging to each ROI of the cortical surface. Because our ultimate goal is to calculate how sensitivity to absorption changes varies across population, we increase SNR by expanding the ROI's surfaces into ROI cortical regions (a few millimeters deep) by dilating them by 4 units (see Figure 4-11). In this study we use these fROIs to validate our scalp landmark-based registration algorithm: we find these 24 fROIs in each subject (which is our "ground truth") and its corresponding registered atlas (using $SLR_{10\text{-}20}$) and calculate the misplacement between corresponding regions. Furthermore, these functional areas will be used in Chapter 5 to calculate variability across population of sensitivity to absorption changes in each ROI, finding differences specific to each region or hemisphere.

#### 4.3.5.2 Results

To validate our registration algorithm accuracy we need to analyze the effect it has on cortical landmarks. With that goal in mind, we selected 24 cortical areas (of interest for functional studies), find their location on each subject of our dataset as well as on each atlas registered to it using $SLR_{10\text{-}20}$. Then we used these corresponding areas to measure the misplacement caused by $SLR_{10\text{-}20}$. We used Dice's coefficient to compare each pair of corresponding areas (viewed as set of voxels, $X$ and $Y$). Dice's coefficients are calculated with the formula:

$$\frac{2 * |X \cap Y|}{|X| + |Y|} \tag{4.1}$$

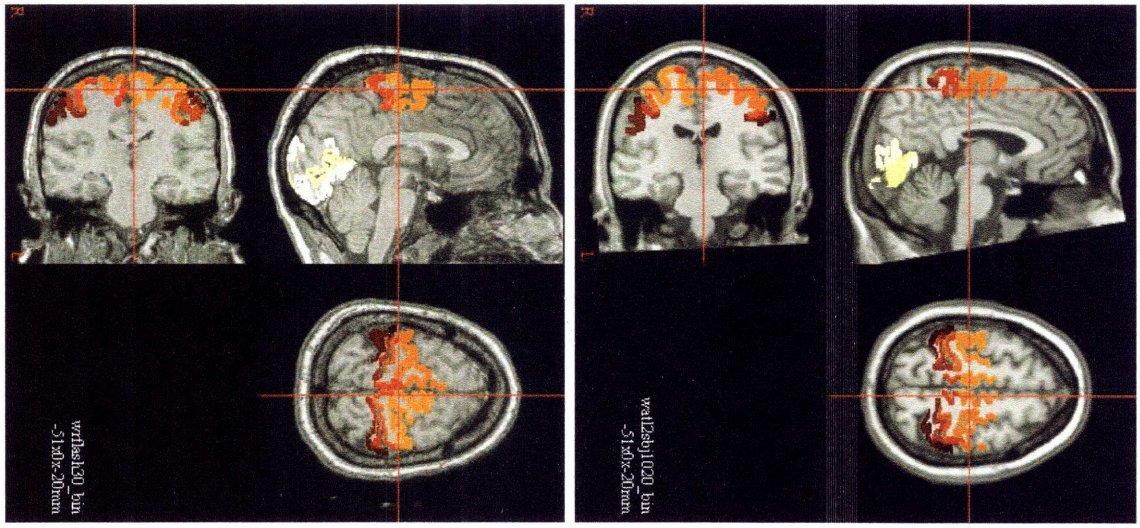

(a) (b)

Figure 4-11: (a) A single subject anatomical MRI (black and white) and overimposed the 24 cortical regions of interest (color). (b) The atlas registered to the subject from (a) and its corresponding ROIs. The red crossbars junction indicates a point of BA6 (pre-motor cortex, the largest region colored in light blue in Figure 4-10) on the subject (a) and its corresponding location on the registered atlas (b). The white and yellow ROIs on the occipital lobe are V1 and V2. At first glance the two anatomical MRI, (a) and (b), seem well aligned, but further analysis will show how little most correspondent areas overlap (see Figure 4-12). The reason of this misalignment lays on the intrinsic variability of the cortical folding patters across population [40]: the functional ROIs have been determined based on the macroanatomical structures (sulci and gyri), rather then being calculated by a trained neuroanatomist analyzing the cytoarchitecture of the cortical folds [42] and therefore they suffer from the same limitations of the anatomical parcellation is based on [47, 43].

where |...| indicates the size of the set. Dice's coefficient is a popular measure of set overlap: a Dice coefficient value of 0 indicates no overlap, which means that the two sets are disjoint; a value of 1 indicates full overlap, which indicates that the two sets are identical.

In Figure 4-12 we show a box plot of Dice's coefficients for each hemisphere (top figure for the right hemisphere and bottom for the left one) for each of the 12 regions of interest (the ROI short name is reported on the $x$ axis, for example, Brodmann area 3a is noted as 3a). We plot lines at the lower quartile, median (in red), and upper quartile values. The whiskers are lines extending from each end of the box to show the extent of the rest of the data and outliers are data with values beyond the ends of the whiskers and they are displayed with a red dot.

The results show quite a variability across the population of the ROI misplacement (note the spread of the Dice's coefficients along the $y$ axis) and a consistently high median error (above 82% in the sematosensory areas and motor cortex in both hemispheres; between 82% and 75% in the visual cortex and Broca's areas). Note that the functional region with less variability across population is BA6, which corresponds to the pre-motor cortex: BA6 is also the region with the smallest error (median error is 63% in the left hemisphere and 66% in the right hemisphere). This is because area 6 is the largest of the selected regions, extending onto the caudal portions of the superior frontal and middle frontal gyri. Because of its location and extension, its localization is overall more consistant, even though the variability across subjects of the curvature of the frontal lobe causes a significant misplacement. Also to note the error for the middle temporal area (MT): this area is thought to play a major role in the perception of motion, the integration of local motion signals into global percepts and the guidance of some eye movements [21]. Its small size and embedded position make it difficult to localize it consistantly over the dataset, resulting in a large spread of the Dice coefficient and lack of data points for a useful statistic. Our results confirm the inter-subject variability of Brodmann areas when subjects are registered using an affine transformation [5] or a non-linear warp aligning cortical folds [42].

## 4.4 Conclusions

Designing a registration algorithm that is not based on the anatomical MRs but still preserves key measurements is essential for a purely optical tomographic imaging of brain activation. We based our registration algorithm ($SLR_{10\text{-}20}$) on scalp landmarks alignment, using the well known EEG 10-20 electrodes system to define a set of points with specific and well documented anatomical features. We tested our registration method on a dataset of 32 healthy subjects and we employed the MNI single subject atlas as the target anatomical model to which we registered the subjects. We validated $SLR_{10\text{-}20}$ against the popular volumetric-based registration algorithm included in the SPM5 toolbox; we compared the two algorithm's performances in preserving scalp landmarks, Cerebral Spinal Fluid thickness, cortical depth. Finally we quantified the localization inaccuracy of a set of 24 cortical functional region of interests on

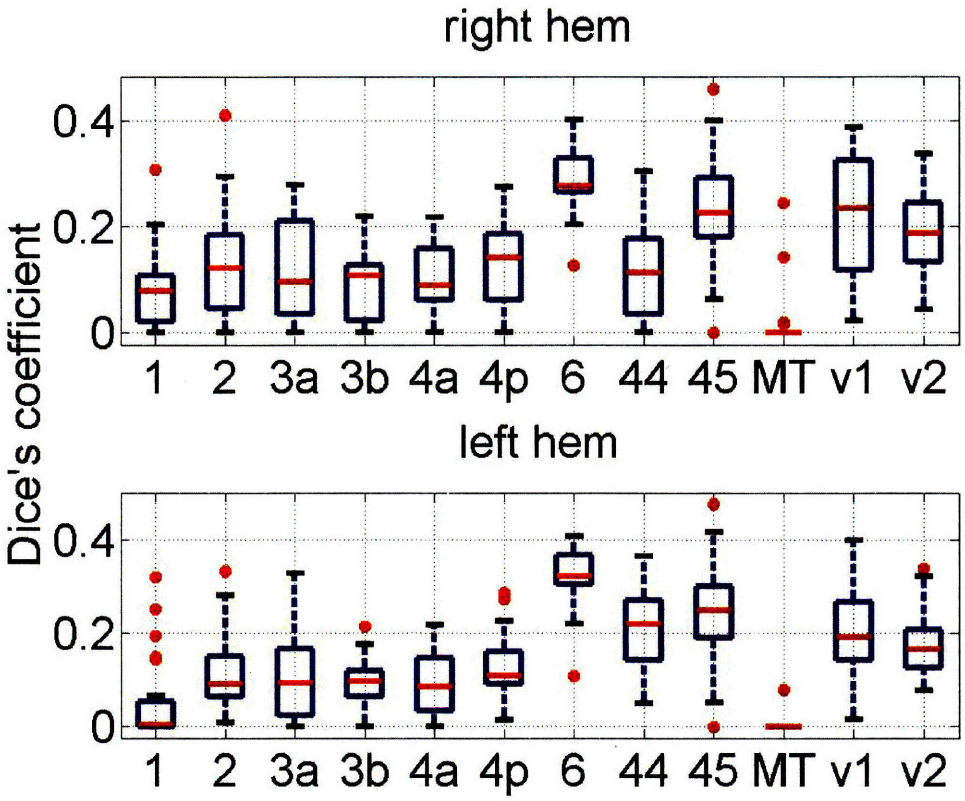


Figure 4-12: Box plot of Dice's coefficients for each hemisphere (top figure for the right hemisphere and bottom for the left one) for each of the 12 region of interest (the ROI short name is reported on the $x$ axis: for example, Brodmann area 3a is noted as 3a). We plot lines at the lower quartile, median (in red), and upper quartile values. The whiskers are lines extending from each end of the box to show the extent of the rest of the data and outliers are data with values beyond the ends of the whiskers, they are displayed with a red dot. The plot show quite a variability across population of the ROI misplacement (note the spread of the Dice's coefficients along the $y$ axis) and a consistently high median error; fortunately, this anatomical inaccuracy does not significantly affect the Partial Path Length measured on the ROIs in the subject and registered atlas because it falls within the limited spatial accuracy of DOT (see Section 5.2.5.3).

the atlas registered to each subject using $SLR_{10\text{-}20}$.

The results support our claim that $SLR_{10\text{-}20}$ is a valid registration algorithm in the sense that the atlas anatomical inaccuracies become irrelevant compared to the low spatial resolution of Diffuse Optical Tomography. The tests performed on the two registration algorithms showed that $SLR_{10\text{-}20}$ is a better candidate than SPM5 for our application because:

1. It better preserves probe placement (max and mean landmark localization errors are 7.6 mm and 4.33 mm for $SLR_{10\text{-}20}$ versus 17.07 mm and 9.6 mm for SPM5 respectively),

2. It has a smaller impact on cortical depth (max and mean cortical depth difference are 3.9 mm and 0.05 mm for $SLR_{10\text{-}20}$, whereas SPM5 max difference is 4.3 mm and mean is 0.54 mm),

3. Comparably to SPM5, it does not affect CSF thickness; for both SPM5 and $SLR_{10\text{-}20}$ registered subjects we observe the intrinsic large difference of CSF thickness across subjects (up to 190%), mostly due to aging (which can be corrected by using an age/CSF thickness model, as shown in Section 5.2.1).

When testing $SLR_{10\text{-}20}$ on ROI identification accuracy, the registration algorithm preserved the general anatomical location of the largest regions (see Figure 4-11) but, due to the often small size of the regions and their location embedded in deeper cortical structures, a strict measure of corresponding regions overlap gave low scores (see Figure 4-12). Fortunately, this inaccuracy does not significantly affect the Partial Path Length measured on the ROIs in the subject and registered atlas because it falls within the limited spatial accuracy of DOT (see Section 5.2.5.3).

Our non-volumetric registration algorithm can be used for longitudinal 3D EEG and MEG studies when an anatomical MR of the subject is not advisable or available; typically the positions of the 10-20 scalp landmarks are acquired in most EEG studies, making the application of $SLR_{10\text{-}20}$ particularly suitable. Scalp-landmark based affine registrations have been successfully used to map 2D EEG sources in stereotactic space (solving the inverse problem in subject space and then mapping the solution in atlas space): Darvas et al. [30] compares source localization accuracy using a rigid transformation [53], an affine transformation [30] and a non-linear transformation (Thin Plate Spline, TPS) [30]; their results show that a non-linear registration is more accurate in identifying the position of the dipoles when using the direct TPS transformation, mapping measurements in subject space (8.1 mm mean error), whereas accuracy decreases (15.2 mm mean error) when expressing results in atlas space (using the inverse transform), performing similarly to the affine transformation described in the paper (mean errors = 22.3 mm in subject space and 19.5 mm in atlas space). The rigid [53] and affine [30] transformations described in these papers use procedures similar to the virtual 10-20 algorithm we use [76], but with a more limited head-modeling accuracy because the 9 or 12 transformation parameters (for the rigid and affine registration

respectively) are estimated using only 3 or 4 of the EEG 10-20 points (Nz, A1, A2 and Cz), lacking information on the frontal pole and occipital regions.

Since affine registrations preserve relative distances (modulo a scaling factor), the cortical depth measurements in MNI space (see Figure 4-8) also confirm the observations reported for the CSF population study (see Figure 2-16), that is, decrease of cortical thickness and consequently increase of CSF thickness are effects of normal aging [31, 73, 108] as well as neurodegeneration due to various diseases [4, 50, 58, 37, 107, 78, 117, 61, 20, 79, 124, 123, 104, 83]; therefore, studying cortical thickness can be another non-invasive effective way to investigate neurodegeneration and its treatment.

In summary, we proposed an alternative non-volumetric registration algorithm based on the alignment of scalp landmarks (the EEG 10-20 electrodes system), the Scalp Landmark based Registration ($SLR_{10\text{-}20}$). We validated the algorithm against the well known volumetric affine registration method available in the Statistical Parametric Mapping toolbox, SPM5 [3], and found that $SLR_{10\text{-}20}$ performs better than SPM5 in preserving scalp landmarks and its accuracy in mapping cortical landmarks is not worse than the intrinsic variability of macroanatomical and cytoarchitettonical structures across subjects [40] (see Table B.3), suggesting that $SLR_{10\text{-}20}$ is well suited to register a general anatomical head model to a subject's head which is then used to guide DOT forward problem (see Chapter 5), provided that the atlas CSF thickness is modified accordingly (see Section 5.2.1).

# Chapter 5

# Purely optical tomography

Currently the most successful method of solving the DOT inverse problem is to use subject-specific anatomical information which is derived from an MR anatomical scan. The head model is generated by segmenting a subject specific 3D anatomical MRI scan. Such model creation requires the availability of an MRI scan, along with a careful analysis of the MRI data to compute the four tissue types' segmentation. Here, we explore substituting a generic head model, or atlas, in place of the MRI-based anatomically correct 3D head model. Our hypothesis is that such a generic anatomical model might be sufficient for solving the optical forward and inverse model and hence localize brain activation with acceptable spatial accuracy. In order to validate our claim, we first simulate measurements of total detected fluence as well as sensitivity to absorption changes in the brain of an atlas and we calculate the deviation of such measurements against those simulated in the true subject head model registered to the atlas using the volumetric-based algorithm from SPM toolbox. The results indicate that it is possible to simulate photon migration on an atlas instead of the specific subject's anatomy introducing an error of 10% in sensitivity to absorption changes in the brain. Encouraged by these observations, we then show the results of an analogous population study, where 31 atlases are generated by registering an atlas (with a modified CSF layer to match that of the corresponding subject) to one of the 31 subjects (see Section 2.3.1) using our superficial landmark based registration algorithm, $SLR_1$0-20 (see Chapter 4). We conclude our validation with a demonstration of the purely optical tomographic protocol on three experimental subjects on which are acquired functional optical measurements.

## 5.1 Atlas vs. subject: SPM5-registered subject

We compare the measurements obtained using a linear probe to simulate photon migration on two anatomical human head models, a reference head, or atlas, and a subject head. We registered the subject head to the atlas' using the volumetric registration algorithm available in the SPM5 toolbox (Wellcome Department of Cognitive Neurology, University College, London) [3].

The most salient measurement of DOT forward model accuracy is the sensitivity to absorption changes in the brain (or Partial Path Length, PPL) [99, 27, 115], which is a good indicator of accuracy of the reconstructed hemodynamic changes associated with neuron activation [27]. The PPL results shown support our hypothesis that an atlas anatomy can be used instead of the subject-specific anatomy with only 10% difference in brain sensitivity.

### 5.1.1 The linear probe

The probe consists of one single source and twenty five detectors placed on the same coronal slice on the right side of the head in the area corresponding to the precentral gyrus (see Fig. 5-1a-b). The single source is placed near the intersection of the precentral gyrus, the frontal superior gyrus and the frontal middle gyrus and the detectors are evenly spaced 2 mm apart starting from 10 mm away from the source to 58 mm. This particular probe proved useful for describing the measurements as a function of source-detector separation and depth probed by the injected photons [27, 98].

### 5.1.2 The atlas

The general human head model used is the single subject MNI atlas [25]. This model is constructed from a high-resolution (1 mm isotropic voxels) low-noise data set that was created by registering 27 scans (T1-weighted gradient echo acquisitions with TR/TE/FA = 18 ms/10 ms/30 deg) of the same individual in stereotactic space where they were sub-sampled and intensity averaged [66]. The volume contains 181x217x181 voxels and covers the brain completely, extending from the top of the scalp to the base of the foramen magnum.

A model with four tissue types was derived from the nine tissue types segmentation of the MNI single-subject atlas available from BrainWeb [2], by re-labeling optically similar tissue types: connective tissue, fat and muscle/skin are labeled as skin; glial matter is labeled as white matter (brain). The resulting discrete model is a volume of 181x217x181 $mm^3$ voxels. The optical properties of each tissue type are reported in Table 2.2 as they appear in [111, 112].

### 5.1.3 The subject

The subject head model was provided by Angelone and Bonmassar. The subject head is a high resolution model generated from MRI data of a healthy adult human subject and developed by collaboration between the Analog Brain Imaging Laboratory at the Athinoula A. Martinos Center and the Center for Morphometric Analysis at Massachusetts General Hospital [7, 86]. Quantitative volumetric segmentation was performed using T1-weighted MRI of a 37 year old healthy male adult subject (1.5 T scanner (General Electric, Milwaukee, WI, USA), birdcage transmit/receive head coil, TR/TE = 24 ms/8 ms with 124 slices, 1.3 mm thick, matrix size 256192, FOV 256 mm). The volume data were resampled to obtain isotropic voxels with dimensions

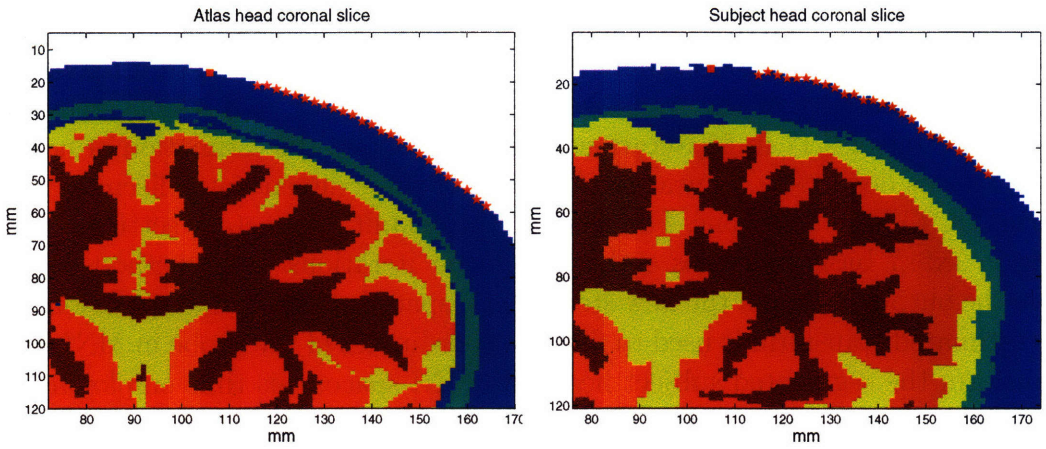


(a) (b)

Figure 5-1: A coronal slice of the segmented MNI single-subject head model (a) and the segmented subject head model (b) are shown. Voxel size is 1x1x1 $mm^3$. The probe (in red) consists of one single source (red square) and twenty five detectors (red stars) placed on the same coronal slice on the right side of the head in the area corresponding to the precentral gyrus. The single source is placed near the intersection of the precentral gyrus, the frontal superior gyrus and the frontal middle gyrus and the detectors are evenly spaced 2 mm apart starting from 10 mm away from the source to 58 mm. This particular probe proved useful for describing the measurements as a function of source-detector separation and depth probed by the injected photons [27].

of 1x1x1 $mm^3$. This MGH-CMA head model was re-labeled into four tissue types (see Table 2.2).

We use the MGH-CMA head model (further referred as subject head) as the reference model. The segmentation of the CSF layer was further improved by dilating it using a 3x3 box structural element. In Fig. 5-1a and Fig. 5-1b a coronal slice of the two head models and the optical probe is shown.

## 5.1.4 Methods

In order to compare the measurements that would be obtained by simulating photon migration in the subject head with those calculated using the atlas instead, we need to bring our head structures into the same coordinate system. We can then proceed to analyze the simulated measurements and quantify their deviation.

### 5.1.4.1 Warping the subject into MNI stereotactic space

After excluding unnecessary parts of the subject head (like neck and air voxels around the head) and determining the new origin of the subject head at the anterior commissure location, the subject MRI is registered to the MNI single subject atlas. For the task, we use the normalization procedure available in the SPM5 toolbox. The de-

fault parameters are used in both the linear and nonlinear iterations. First, the affine transformation parameters are estimated using a Bayesian framework that maximizes the posterior probability of the transformation being correct, and it converges to a mean square error of 0.17 in 55 iterations. Then, it follows the estimation of nonlinear deformations defined by a linear combination of three dimensional discrete cosine transform (DCT) basis functions. For this step the default parameters' setting is used, resulting in 7x9x7 basis functions and 16 nonlinear iterations. The method used to resample the output image in the new stereotactic space is trilinear interpolation [51].

The estimated transform is used to find the coordinates of the probe in MNI space and transform the segmented subject head into MNI space, this time employing the nearest neighbor interpolation to resample the voxels' labels in the new space. The resulting subject head is a 184x216x184 $mm^3$ voxel volume. Minor adjustments were required to ensure that the new optodes coordinates corresponded to outermost scalp voxels.

#### 5.1.4.2 Monte Carlo simulation

We use a Monte Carlo solution of the RTE [16] to simulate photon migration in highly scattering tissues. The method models photon trajectories through heterogeneous tissues, reproducing the randomness of each scattering event in a stochastic fashion (a random seed is employed). When a photon is detected, its partial optical path length for each of the tissue types through which it passed are recorded in a history file. We ran eight hundred million photons and recorded the number of exiting photons at the twenty five detectors' locations. We used scattering anisotropy $g = 0.01$, and refractive index for all tissues is assumed to be 1.

#### 5.1.4.3 Calculation of total fluence

After simulating photon migration with Monte Carlo, the detected light intensity thus obtained is used to calculate the total fluence in continuous-wave (CW) (see definition in Equation 1.6) by summing over the time index $i$ the fluence rate in time-domain from Equation 1.19, resulting in the expression from Equation 2.1, which is repeated here:

$$\Phi_j = \sum_{\tau=t_o}^{T} \left( \frac{1}{N_j(\tau)\Delta t} \sum_{l=1}^{N_j(\tau)} \prod_{m=1}^{N_R} \exp(-\mu_{a,m} L_{j,l,m}) \right) , \tag{5.1}$$

where $\Phi_j$ is the measured photon fluence at detector $j$, $N_j(\tau)$ is the number of photons collected at detector $j$ in a time-gate of width $\Delta t$ centered at time $\tau$, $T$ is the total time elapsed (4 ns in our study), $\exp(-\mu_{a,m} L_{j,l,m})$ describes the effects of absorption in each region $m$. $L_{j,l,m}$ is the path length of photon $l$ through region $m$, and the photon migration time is related to the photon path length by the speed of light in the medium. $N_R$ is the number of regions through which the photons migrate.

The total fluence relative error is computed by calculating the difference between the total fluence measured on the atlas head and that detected on the subject head, relative to the reference measurement (i.e. the subject-based fluence) as follows:

$$\Phi_{j,\text{relative}} = \frac{\Phi_{j,\text{atlas}} - \Phi_{j,\text{subject}}}{\Phi_{j,\text{subject}}} * 100 \ , \tag{5.2}$$

where $\Phi_{j,\text{atlas}}$ is the fluence measured at detector $j$ defined in Equation 5.1, using the atlas anatomical model.

#### 5.1.4.4 Calculation of Partial Path Length (PPL)

Tissue scattering causes the photons to travel a greater distance than the geometric distance between the source and detector. The partial path length of light through each of the tissue types $m$ is defined as [99, 27, 115] as

$$\text{PPL}_m = \frac{\partial \text{OD}}{\partial \mu_{a,m}} \ , \tag{5.3}$$

where $\text{OD} = -\log(\Phi/\Phi_\tau)$, $\Phi$ is given by (5.1) and $\Phi_\tau$ is the incident number of photons. The partial path length at each detector $j$ is thus easily derived from (5.1) and the definition of $\text{PPL}_m$ from above as:

$$\text{PPL}_{j,m} = \frac{\sum_{l=1}^{N_j(t_i)} \prod_{m=1}^{N_R} L_{j,l,m} \exp(-\mu_{a,m} L_{j,l,m})}{\sum_{l=1}^{N_j(t_i)} \prod_{m=1}^{N_R} \exp(-\mu_{a,m} L_{j,l,m})} \ . \tag{5.4}$$

The PPL relative error is calculated from (5.4) as the percent relative deviation between the atlas-based PPL and the subject-specific PPL in each tissue type as follows:

$$\text{PPL}_{\text{relative}} = \frac{\text{PPL}_{\text{atlas}} - \text{PPL}_{\text{subject}}}{\text{PPL}_{\text{subject}}} * 100 \ . \tag{5.5}$$

The PPL relative error measures the sensitivity to absorption changes in each tissue type, and, because the brain PPL is central to the optical observation of brain activity, we expect that it will provide a good estimate of how accurately we will solve the inverse problem by reconstructing hemodynamic changes and thus localize activated brain regions.

### 5.1.5 Results

#### 5.1.5.1 Total and relative fluence

Figure 5-2a shows the total fluence simulated at the detectors' locations in the subject head (in red) and in the atlas (black); in Fig. 5-2b is plotted the relative error, which is the atlas fluence relative to the subject-specific detected fluence as a function of source-detector separation.

The deviation in total fluence, quantified in Fig. 5-2b, is very likely due to the roughness of the surface on the subject head at small separations. At distances greater than 25 mm the cumulative effect of the different CSF and bone thickness and

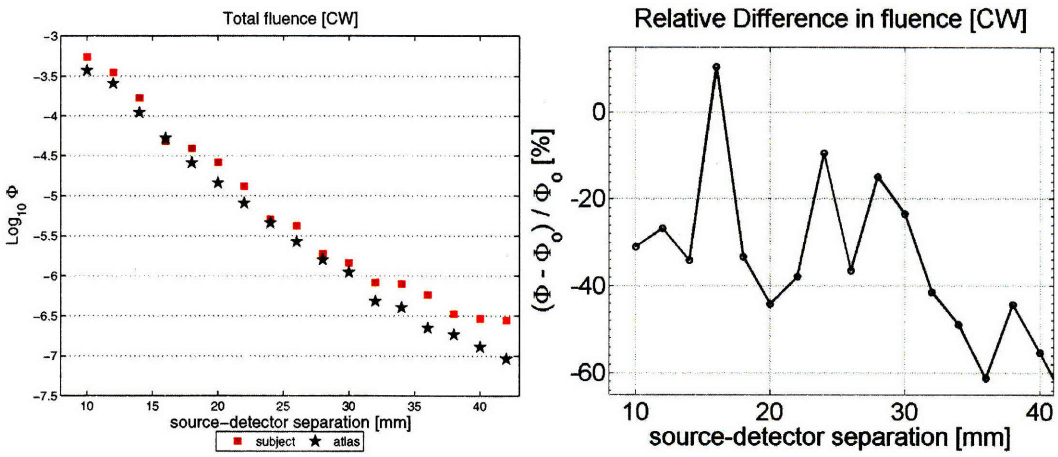


(a) (b)

Figure 5-2: (a) Total detected fluence simulated with Monte Carlo in continuous-wave (CW) versus source-detector separation when using the subject-specific anatomical model (red squares) and the atlas anatomical model (black stars). (b) Percent relative fluence error in continuous-wave calculated with respect to $\Phi_o$, which is the Monte Carlo predicted fluence exiting the subject head.

therefore the total number of photons reaching further detectors is the main cause of the relative error (between 15% and 60%). We believe that the discontinuous nature of the error function is due to the roughness of each tissue type contour which is partially due to the warping effect of the normalization algorithm. Such discontinuity can be decreased by smoothing the normalized image, minding not to lose spatial resolution. As stated previously, deviation in total fluence does not have a strong bearing on localizing brain activation, whereas the brain partial path length is directly connected to the observation of hemodynamic changes and thus neural activity.

#### 5.1.5.2 Total and relative PPL

The sensitivity to absorption changes in scalp-skull and brain as a function of source-detector separation is shown in Fig. 5-3a and Fig. 5-3b respectively. Figure 5-3a displays the PPL in the subject (dotted line) and the atlas (continuous line) for $\mu_a$ changes in scalp-skull (red lines) and in brain (blue lines) whereas in Fig. 5-3b the difference between the dotted and the continuous lines is quantified.

When we look at the relative error plot (Fig. 5-3b), we observe that the sensitivity to $\mu_a$ changes in scalp-skull varies only slightly between the two head models (error less than 4%), in agreement with [29], whereas the path length in the brain varies more, in agreement with the sensitivity to CSF thickness described in [27, 29]. However, the PPL relative error is no larger than 10% at separations greater than 25 mm (which is where the photons start to probe the cortex). The error reduces significantly at larger distances due to the longer photon path length in the brain and therefore smaller effect of the clear CSF layer (at 36 mm separation PPL relative error approximately equals zero).

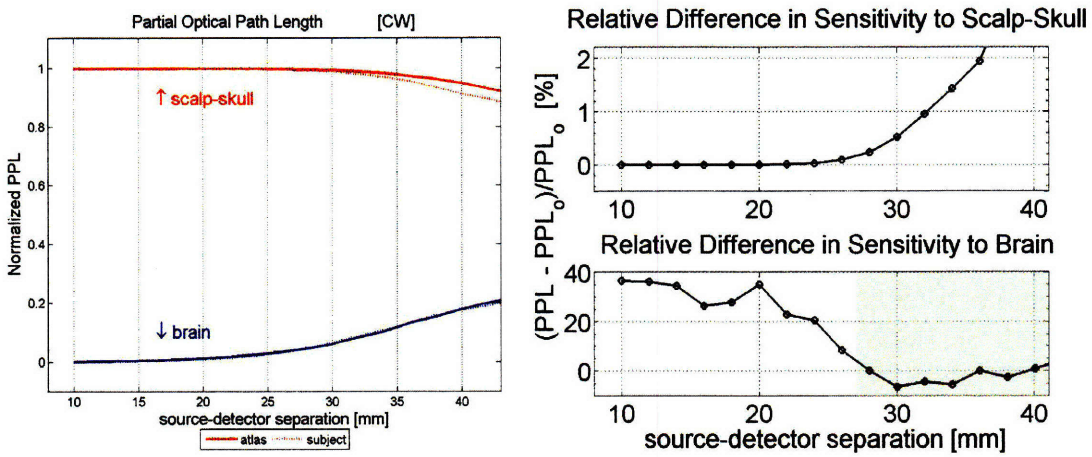


(a) (b)

Figure 5-3: (a) Monte Carlo normalized partial path length calculated versus source-detector separation in continuous-wave (CW) when using the subject-specific anatomical model (dotted line) and the atlas anatomical model (continuous line). In red is plotted the PPL in scalp-skull, in blue the PPL in the brain. The PPL is normalized by the total sensitivity to all tissue types. (b) Monte Carlo measure of percent relative sensitivity to scalp-skull layer (top) and brain (bottom) versus separation with respect to $PPL_o$, which is the Monte Carlo prediction of PPL of the subject-specific head model.

### 5.1.6 Conclusions

As Fig. 5-3 clearly shows, the results thus far are encouraging. In the case that a suitable atlas is selected and the variation of CSF thickness between head models is not significant, the sensitivity to absorption changes in the brain is well modeled by atlas-based measurements (with error less than 10%). A mechanism for proper atlas selection is not yet established. So far, there has been little investigation of the variability of CSF across a population as a function of age, gender and race. The general consensus seems to be that the CSF layer increases with age, but we are not aware of any study validating or quantifying this claim. Our next goal is to conduct a study across a large population to characterize CSF variation factors.

Thus far, we successfully substitute the subject anatomical information with those of an atlas in the simulation of light propagation with Monte Carlo algorithm. However, currently we still need the subject MRI to estimate the registration parameters to bring the optodes coordinates from subject space to MNI-atlas space. As demonstrated in our follow up study (Section 5.2.5), we developed an algorithm for non-MRI based registration described in Chapter 4 that uses a set of superficial landmarks as correspondence points to estimate the twelve parameters of the affine transformation. As superficial landmarks we employed the virtual 10-20 electrode system created by Jurcak et al. [76] that automatically generates the locations of the EEG 10-20 standard points on a given surface.

## 5.2 Atlas vs. subject: $SLR_{10\text{-}20}$-registered atlas

Optical tomography comprises two steps: in the forward model ($y = Ax$) photon migration is simulated in a segmented head calculated from the subject anatomical MRI; the simulation results in a map ($A$) of the head volume indicating each voxel sensitivity to absorption changes; the second step is the solution of the inverse problem ($x = A^{\dagger}y$): the sensitivity map $A$ is used in the DOT inverse problem along with simulated or experimental measurements ($y$) to generate the vascular activity map $x$ (see Sections 1.1.2.1 and 1.1.2.2). We would like to eliminate the role of MRI in the DOT process, which means performing the forward process without using the subject's anatomical MRI, while still measuring the vascular effect of neural activation on the subject head. With this goal in mind, we propose the use of a reference head (an atlas, see Figure 5-4C) in the Monte Carlo simulation of photon migration that generates the sensitivity map (solution of the forward model), as described in Figure 5-4. The atlas is registered to the subject head via a non-MRI-based registration algorithm (the Superficial Landmark-based Registration method proposed in Chapter 4); the registration algorithm outputs an affine transformation that maps points in atlas space to correspondent points on subject space (see Figure 5-4). A probe is designed and placed on the physical subject during optical measurements of brain activity (see Figure 5-4b) and the estimated affine transformation is used to map that probe to the synthetic scalp of the registered atlas (see Figure 5-4B). On the atlas is simulated the photon migration process using Monte Carlo [16] which results in a volumetric map of sensitivity to absorption changes (which, for each head voxel, is calculated as its sensitive to $\mu_a$ changes as a function of the fraction of injected photons traversing that voxel (see Equation 1.17)). The inverse of the affine transformation is then used to transform the sensitivity map obtained by simulating photon migration on the registered atlas into the subject on which the actual optical measurements have been taken. Once we have obtained measurements ($y$) and forward model ($A$) on the subject's coordinate system, we could proceed by solving the inverse problem ($x = A^{\dagger}y$), as done for the experimental dataset (see Section 5.2.5).

On the larger population MRI dataset, we focus on the forward model, measuring protocol accuracy as a function of the Partial Path Length calculated on a set of functional regions of interest (see Section 4.3.5.1 for details on the calculation of these regions). We conclude our validation by considering results on three experimental subjects on which functional optical measurements have been acquired.

### 5.2.1 Atlas selection

Atlas selection is the first step of a purely optical approach to functional brain imaging. The atlas substitutes the subject anatomical information and the photon migration process is simulated on it; therefore, it is important that the chosen atlas preserves at best the features to which DOT is most sensitive. We use these principles to select the atlas:

1. We select an atlas with a provided accurate segmentation; we have shown how

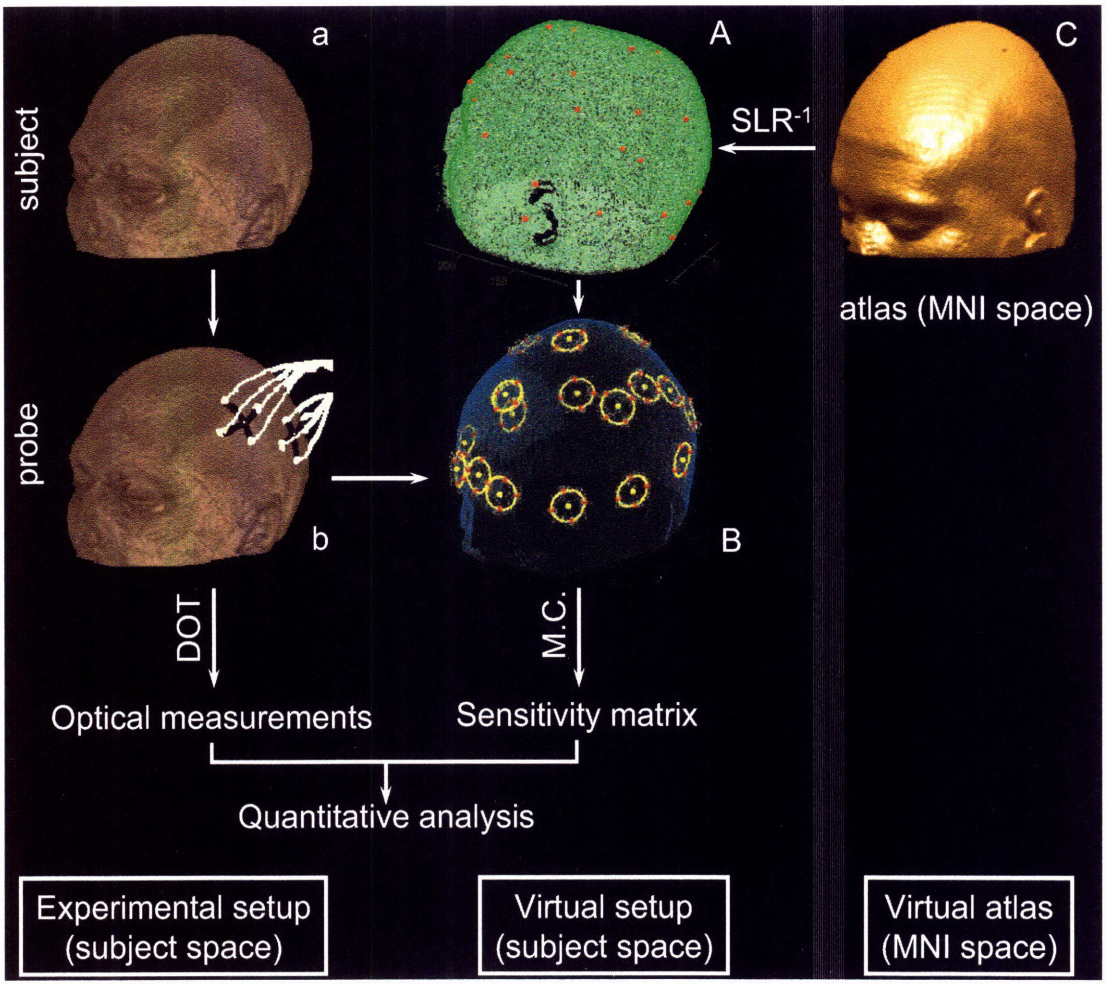


Figure 5-4: On the physical subject head (a) we place the physical probe (b) and we acquire optical measurements; then we register the MNI atlas (C) to the subject's scalp using $SLR_{10\text{-}20}$ (A) and: (1) if we use our 10-20 based probe, we find the virtual probe location on the registered atlas by transforming the 10-20 locations calculated on the atlas into subject space by applying $SLR_{10\text{-}20}$ (B), or (2) if we use any other physical probe, then we simply project the locations of the physical probe onto the registered atlas scalp; having defined the virtual probe on the registered atlas, we simulate photon migration on the registered atlas using Monte Carlo, producing the sensitivity matrix which, combined with the optical measurements, forms the parameters of the DOT inverse problem.

critical is an accurate labeling of the Cerebral Spinal Fluid for the forward model [29] and even though we were able to significantly improve CSF segmentation with our semi-supervised segmentor (see Section 2.3.2.1), the ambiguity of the typical CSF magnetic intensity values makes a perfect segmentation of CSF intrinsically difficult; the most effective way of separating CSF from gray matter and skin-like tissues (such as muscles, fat, bone marrow, skin, dura) is to combine anatomical data from various sources (such as manual labeling of T1 and T2 weighted MR scans, and Proton Density data) as done for the MNI single subject atlas [25].

2. Selecting a standard and well documented atlas has its advantages: expressing measurements in MNI space makes it easier to compare results with other's findings and it provides a familiar framework in which to present results.

3. Once the atlas to use is decided, we need to minimize its differences with the subject for which it will be substituting. We do so by adjusting the atlas CSF median thickness to the subject's; at this stage of our work, we defined a good metric to determine someone's CSF thickness without using the anatomical MRI: we simply use age as a function of CSF thickness. We estimated the linear model best representing the relationship between age and CSF thickness by fitting the data extracted from a CSF study performed on 32 healthy subjects (see Section 2.3.3.1 and Table 2.3 for more details). In Figure 5-5 we show the linear fitting of the data points from that study (shown in Figure 2-16): the black circles represent the CSF thickness median over the sampled scalp points. Given a subject's age, we thus estimate its median CSF thickness and then dilate or erode the registered atlas' CSF layer to match the subject's estimated value.

### 5.2.2 Probe and atlas registration

In order to generate Partial Path Length maps on the registered atlas and the subject and thereto compare them, we need to design a set of optodes (the "probe") to virtually place on the registered atlas' and on the subject's heads. The probe has to be designed to cover the functional regions we are interested in imaging; it also needs to preserve the spacing of about 30-40 mm between optodes in order to allow light to penetrate the superficial tissues, probe the cortical surface and travel back to the detecting optical fibers. We decided to use the already available superficial landmarks from the EEG 10-20 international system as "place holders" for the optodes locations because they cover the cortical surface and they are evenly distributed. Each 10-20 point localizes a *mini-probe* of four optodes that we place at 15 mm distance from each 10-20 point and we maximize the distance between each of the four optodes (i.e., the inter-optode distance ranges between 21 mm and 30 mm), as shown in Figure 5-6. We calculated the positions of the optodes on the scalp mesh by calculating the 15 mm radius circles centered on each 10-20 location (the yellow circles on Figure 5-7) and then defining the north-south and east-west planes at which intersections with

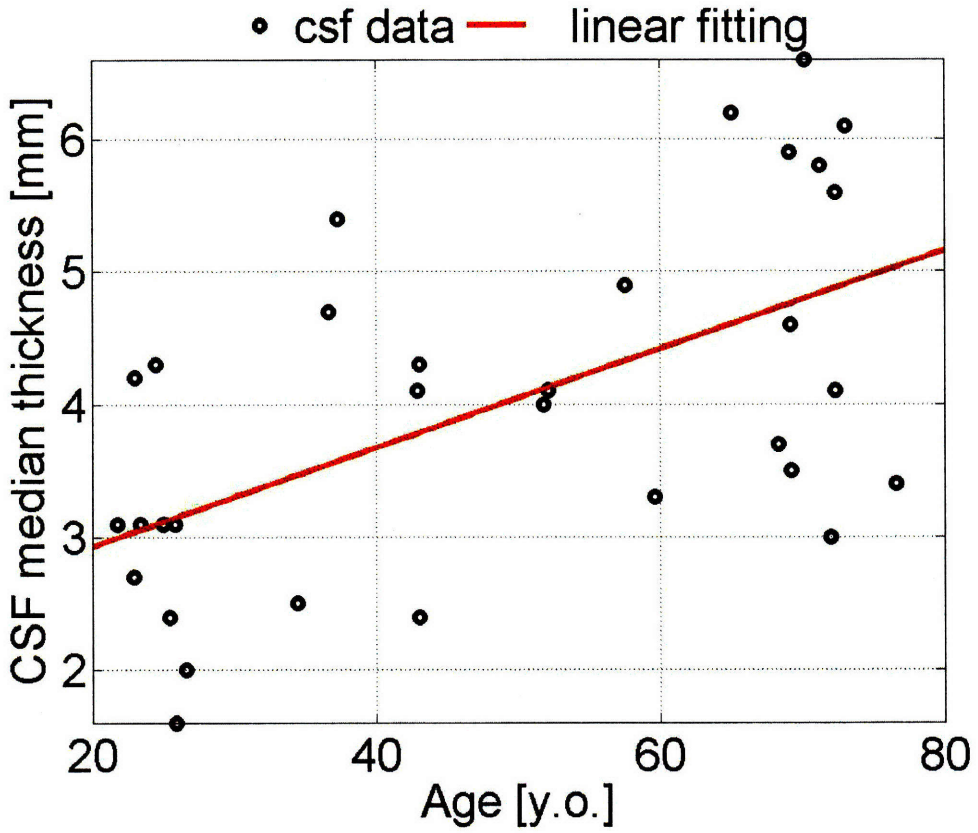


Figure 5-5: Linear fitting of the data points from the CSF-age study of Section 2.3.3.1 (data shown in Figure 2-16): the black circles represent the CSF thickness median over the sampled scalp points. To customize the atlas to the target subject, we estimate the subject's median CSF thickness given its age from this linear model; then we dilate or erode the registered atlas' CSF layer to match the subject's estimated value.

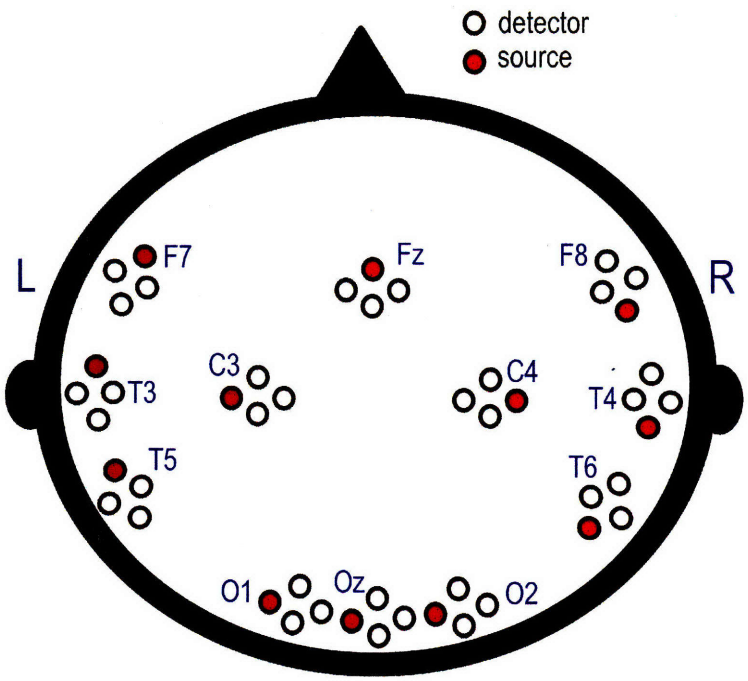


Figure 5-6: The probe has to be designed to cover the functional regions we are interested in imaging; it also needs to preserve the spacing of about 30-40 mm between optodes in order to allow light to penetrate the superficial tissues, probe the cortical surface and travel back to the detecting optical fibers. We decided to use the already available superficial landmarks from the EEG 10-20 international system as "place holders" for the optodes locations because they cover the cortical surface and they are evenly distributed. Each 10-20 point localizes a *mini-probe* of four optodes that we place at 15 mm distance from each 10-20 point and we maximize the distance between each of the four optodes (which is, the inter-optode distance ranges between 21 mm and 30 mm). Because we do not have functional regions of interest in the frontal pole and the parietal regions (see Figures 4-1 and 4-10), we eliminate the *mini-probe* centered on Fp1, Fp2, Fpz, P3, P4, Pz, and Cz.

the circles we determine the four optodes' locations. These are the two planes on which the curves connecting C3-Cz-C4 (for the east-west plane) and Fz-Cz-Pz (for the north-south plane) lie and contain Cz. For the 10-20 points located on the scalp surface orthogonal to the top of the head (such as Oz, O1, O2, for example) we define the companion plane orthogonal to the other two. Using these three planes and the 15 mm radius circles we are able to define uniquely and automatically all the optodes locations (red points in Figure 5-7), provided we have the location of the 10-20 points (yellow dots in Figure 5-7).

We designed a customized registration method that does not use anatomical information other than the scalp surface of the two heads to be registered. The registration algorithm is based on the alignment of superficial landmarks (from which the name

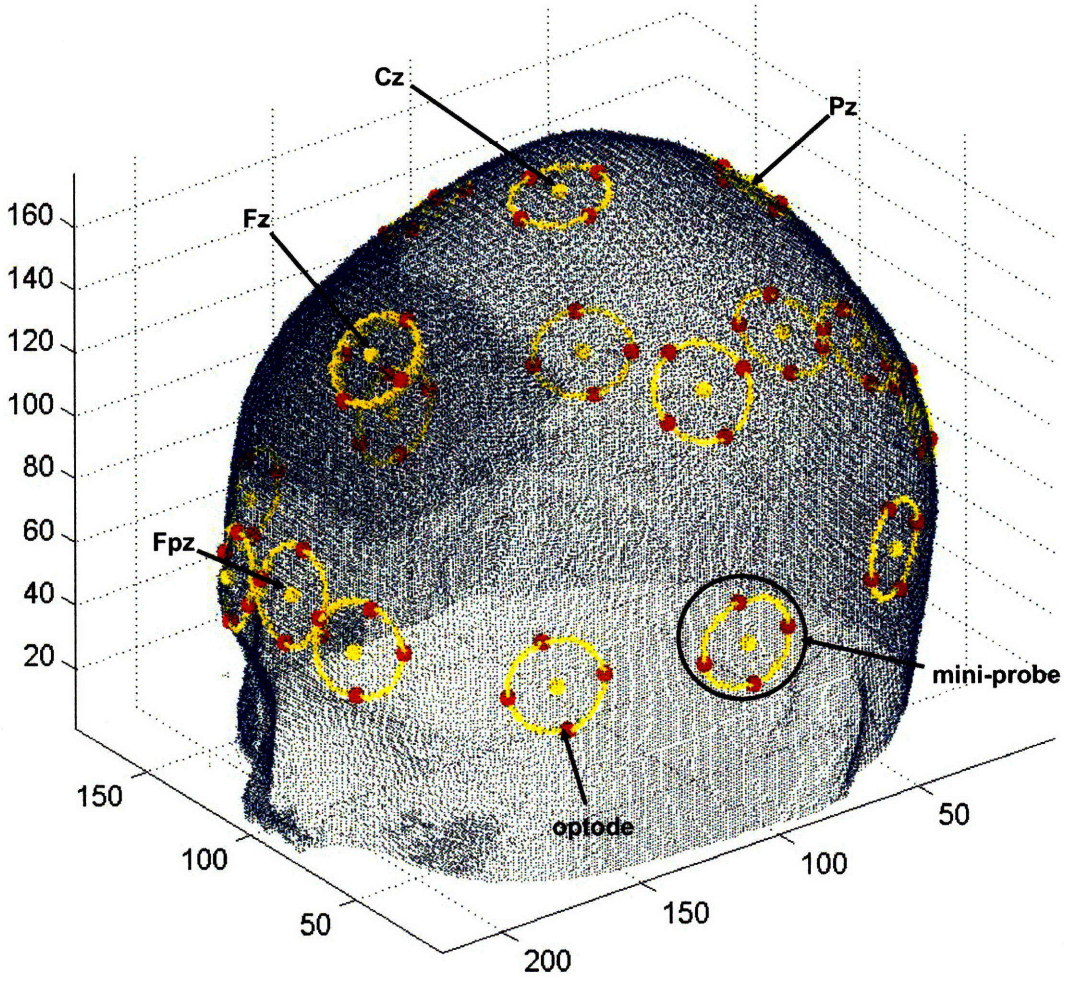


Figure 5-7: Result of the probe placement algorithm: we calculate the positions of the optodes on the scalp mesh by calculating the 15 mm radius circles centered on each 10-20 location (yellow circles) and then defining the north-south and east-west planes at which intersections with the circles we determine the four optodes' locations. These are the two planes on which the curves connecting C3-Cz-C4 (for the east-west plane) and Fz-Cz-Pz (for the north-south plane) lie and contain Cz. For the 10-20 points located on the scalp surface orthogonal to the top of the head (such as Oz, O1, O2, for example) we define the companion plane orthogonal to the other two. Using these three planes and the 15 mm radius circles we are able to define uniquely and automatically all the optodes locations (red points in the figure), provided we have the location of the 10-20 points (yellow dots).

Superficial Landmark-based Registration, or $SLR_{10\text{-}20}$) and extensive testing showed it to be well suited for our application (see Section 4.3). The $SLR_{10\text{-}20}$ algorithm performs especially well in mapping scalp locations from atlas space to subject space or vice versa (see Figures 4-6 and 4-7) and thus we map the designed probe locations from the subject scalp to the atlas' by transforming the coordinates of the 10-20 positions calculated on the MNI atlas (see Section 4.2.3) into subject space. The probe location on the registered atlas is thus derived from the newly found 10-20 landmarks positions. We reduce the total number of optodes from 19 groups of 4 each, down to 12 groups of 4 optodes to minimize Monte Carlo simulation run time and disk space complexity (for each optode, Monte Carlo outputs a file of the size of the number of voxels times the number of source-detector pairs). We selected the optodes to eliminate based on the functional regions covered by each mini-probe of four optodes: as shown in Figure 5-6, the mini-probes centered on P1, P2, Fpz, Fp1 and Fp2 were eliminated because of lack of ROIs on the parietal region and frontal pole; probes centered on Cz and Pz were eliminated because they are too far from the somatosensory and motor areas of interests and also because they are situated on the central sulcus and therefore more susceptible to variability of CSF thickness; finally, probes relative to P3 and P4 were excluded because they fall between two cortical areas of interest but typically are more than 5 mm away from either of them. Similarly to the probe, the atlas segmented MR is registered to the subject using the affine transformation estimated by $SLR_{10\text{-}20}$.

### 5.2.3 Solving the forward model on the registered atlas

Using the same dataset described in Section 2.3.1 of 32 healthy subjects, we generate two sets: in one are 31 of the 32 subjects anatomical MRI (one subject was discarded because it was not possible to extract the right hemisphere cortical surfaces using Freesurfer [1, 45, 46, 41, 43]), they are segmented as described in Section 2.3.2.1 and cropped and translated to the same format to simplify data analysis (190x230x190 mm centered on the anterior commissure at voxel 97 $x$, 126 $y$ and 77 $z$). The second set of data comprises the corresponding 31 atlases registered to the subjects using $SLR_{10\text{-}20}$, their segmentations with adjusted CSF thickness as described in Section 5.2.1 and also re-formatted in the same size and origin as the subjects.

The probe location is calculated on each subject and atlas following the steps described in 5.2.2 and the optodes locations along with the segmented heads are used to generate the input of the Monte Carlo algorithm simulating $3x10^8$ photons propagating on each head. The sensitivity matrix thus generated for each subject and atlas is used to calculate the Partial Path Length (see 1.1.3.3) relative to each of the 24 functional region of interest described in 4.3.5.1.

### 5.2.4 Validation: characterizing accuracy

We claim that under certain circumstances and with some limitations it is possible to use a general anatomical model to substitute the subject specific anatomy and still

quite accurately retrieve the location of the neural activation from the optical measurements. An effective way of validating such a claim, is to solve the forward problem on the subjects' dataset as well as on the registered atlases and from it calculate the Partial Path Length (PPL) that is a measure of sensitivity to absorption changes and, therefore, a good indicator of accuracy in reconstructing neural activation via hemodynamic changes.

#### 5.2.4.1 Measurements

These data are calculated as follows: the PPL is generated applying Equation 1.21 from the fluence recorded at the detectors (OD): $L_{i,j,m} = \partial \mathrm{OD}/\partial \mu_{a,m}$; as a result, we obtain the length photons traveled through each voxel $m$ for any given source-detector pair $(i, j)$ (each mini-probe of four optodes is made of one source and three detectors, hence, 3 measurements, or source-detector pairs); the PPL of an ROI is calculated by adding up the lengths traveled on the voxels belonging to the ROI with respect to a given mini-probe. Intuitively, some mini-probe contributes to the total path length of a cortical region and others do not or contributes in a smaller capacity; therefore, we select and plot the highest PPL calculated for each region, which corresponds to the mini-probe with the highest contribution to the total photon length traveled in the region.

#### 5.2.4.2 Results

We measure the PPL in each functional Region Of Interest (fROI) on each subject and compare it to the PPL of the same region measured on the registered atlas. These results are shown in Figures 5-10 and 5-11: we do not display the PPL measured on the MT region (which is the visual area V5) because of its low Signal to Noise Ratio (SNR) due to the typically large distance between the region and the closest optode. In Figure 5-10 we show the box plot of the PPL measured on each cortical region, displaying the right hemisphere on the top and the left one on the bottom; the data relative to the registered atlases are shown in red, whereas the PPL measured on the subjects is displayed in blue. We use the box plot to show the spread of the PPL over the population: the mid line indicates the median value, the bottom and top lines are at the lower quartile and upper quartile values respectively. The whiskers are lines extending from each end of the box to show the extent of the rest of the data. Outliers are data with values beyond the ends of the whiskers and they are displayed as red crosses. Note that in most cases the registered atlases PPL is within the subjects' limits, suggesting that the registered atlas preserves a measure of the spatial relationship between optodes and ROIs, even within a large anatomical variability across the population. A noticeable exception is V1: as shown in Figure 5-9b, V1 is significantly smaller in the atlas than in the subject, resulting in an inaccurate partial pathlength within the region.

We plot the distribution of each mini-probe source over the scalp (black dots) and their projection on the cortex (gray dots) in Figure 5-8 and 5-9, to show their

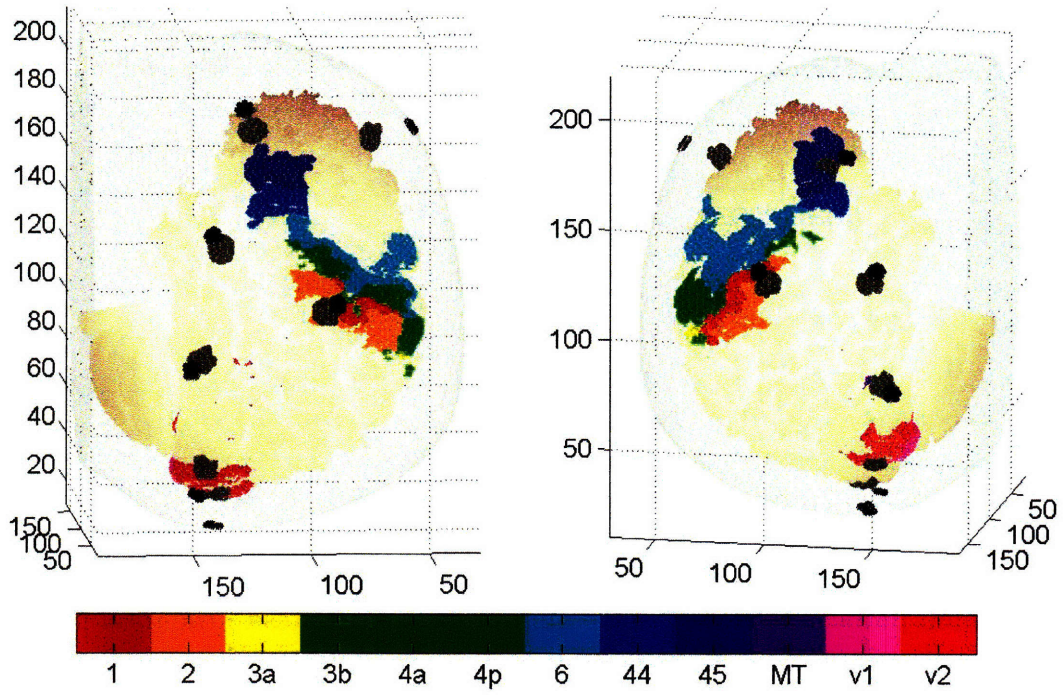


(a)

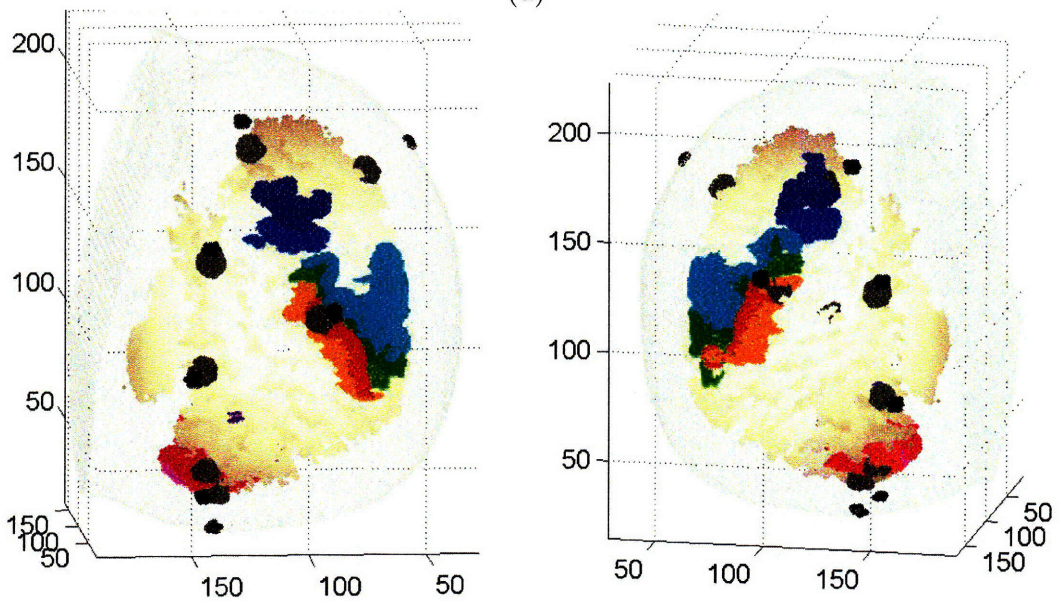


(b)

Figure 5-8: (a) Scalp surface mesh (light gray), cortical surface mesh (pink), functional ROIs (colored according to the colorbar), mini-probes sources (black) and their cortical projections (dark gray) for subject number 4. The left/right side figure favors the lateral view of the left/right hemisphere; (b) similarly, the same views and color-code for the atlas registered to subject number 4. Note the different position of the optodes with respect to the ROIs in each hemisphere: for example area 45 is closer to the optical range of a source in the right hemisphere than in the left one; furthermore, the optodes-ROI distances vary between subject and atlas (see area 45 and MT, for example).

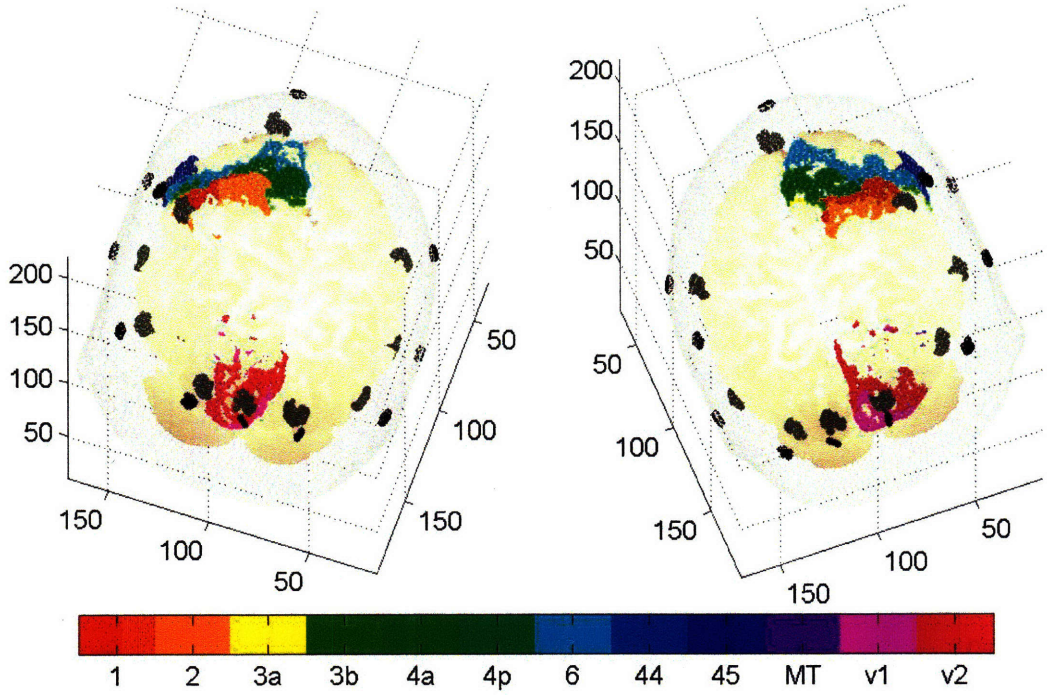


(a)

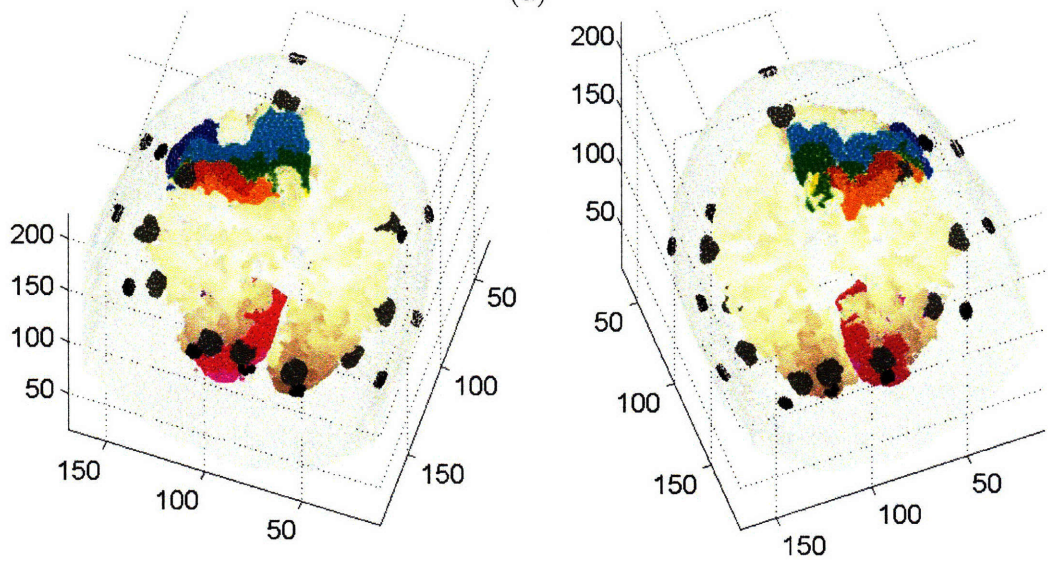


(b)

Figure 5-9: (a) Subject 4 head/cortex/ROI/probe visualization: the scalp surface mesh is plotted in light gray, the cortical surface mesh in pink shades, the 12 functional ROIs are colored according to the colorbar, the mini-probes sources are the black circles and their cortical projections are plotted in dark gray. The left/right side figure shows the occipital view of the left/right hemisphere; (b) similarly, the same views and color-code for the atlas registered to subject number 4. Note how different areas V1 and V2 appear on the subject and registered atlas, especially V1 is significantly smaller on the atlas right hemisphere compared to the subject's.

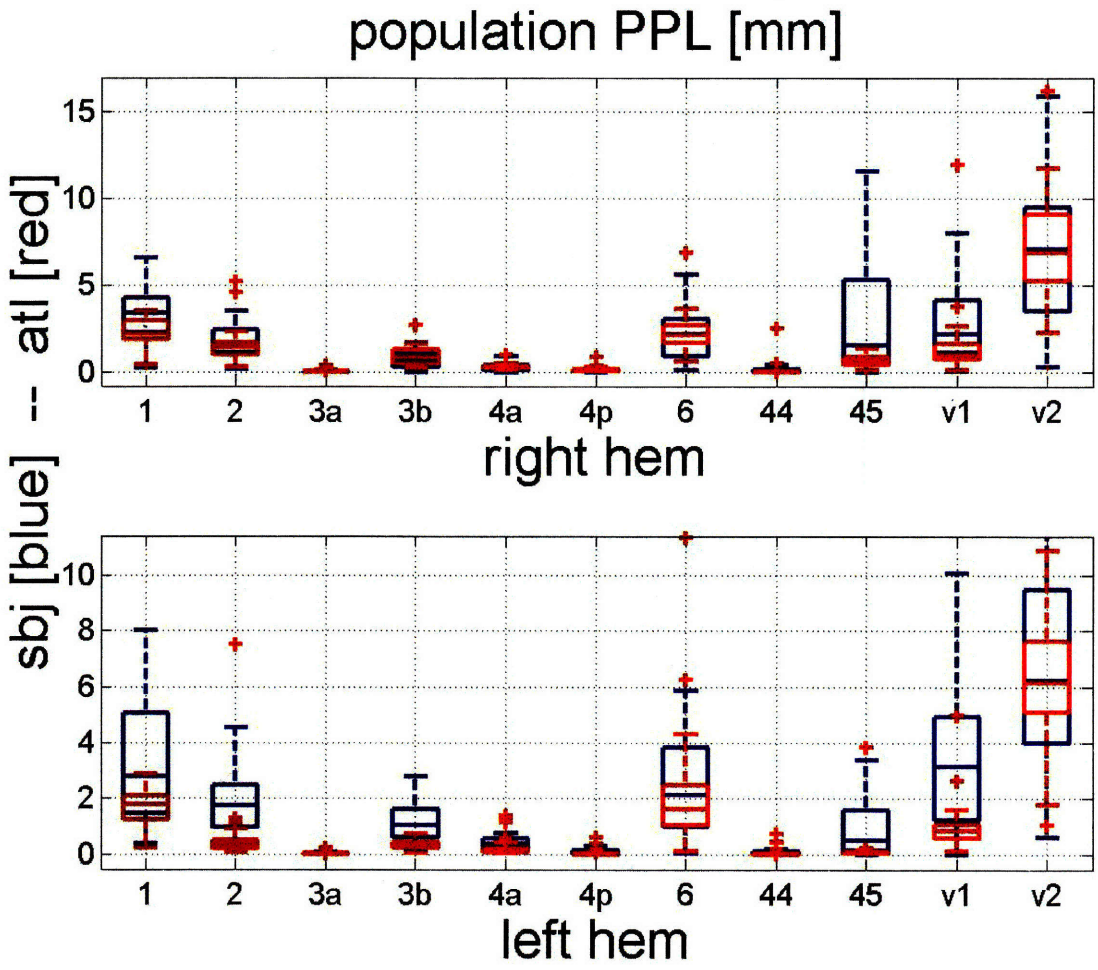


Figure 5-10: Box plot of the PPL measured on each cortical region, displaying the right hemisphere on the top and the left one on the bottom; the data relative to the registered atlases are shown in red, whereas the PPL measured on the subjects is displayed in blue. We use the box plot to show the spread of the PPL over the population: the mid line indicates the median value, the bottom and top lines are at the lower quartile and upper quartile values respectively. The whiskers are lines extending from each end of the box to show the extent of the rest of the data. Outliers are data with values beyond the ends of the whiskers and they are displayed as red crosses. Note that in most cases the registered atlases PPL is within the subjects' limits, suggesting that the registered atlas preserves a measure of the spatial relationship between optodes and ROIs, even within a large anatomical variability across the population. A noticeable exception is V1: as shown in Figure 5-9b, V1 is significantly smaller in the atlas than in the subject, resulting in an inaccurate partial pathlength within the region.

locations relative to the regions of interest (colored) in a subject (Figure 5-8a and Figure 5-9a) and the corresponding atlas registered to it with $SLR_{10\text{-}20}$ (Figure 5-8b and Figure 5-9b).

In Figure 5-11 we plot the relative difference in Partial Path Length measured on the subjects and the atlases. The relative error for each region of interest is calculated using the formula:

$$\frac{(\mathrm{PPL}_{m,subj} - \mathrm{PPL}_{m,reg.atlas}) * 100}{\mathrm{PPL}_{m,subj}} \ , \tag{5.6}$$

where

$$\mathrm{PPL}_{m,subj} = \max_{k=[1,2,3...12]} (\mathrm{PPL}_{k,m,subj}) \ , \tag{5.7}$$

and $k$ is the index of the 12 mini probes (see Figure 5-6) and $\mathrm{PPL}_{k,m,subj}$ is the Partial Path Length measured by the $k^{th}$ mini-probe of subject *subj* in region $m$ (similarly for the registered atlas' dataset). The percentile relative differences plotted are a good measure of the sensitivity inaccuracy introduced by the generic atlas anatomy. Once again, the box plot shows the variability of PPL across the population (horizontal lines at the lower quartile, median (in red), and upper quartile values); the light gray boxes highlight errors between -40% and 40% for the right hemisphere (top row) and between -20% and 40% for the left hemisphere (bottom row).

In Figures 5-12 is shown the population median partial pathlength deviation (corresponding to the red line of Figure 5-11). The median PPL in each ROI $m$ is calculated as follows:

$$\mathrm{median}_{r=[1,2,3...31]} \left( \frac{\mathrm{PPL}_{m,subj_r} - \mathrm{PPL}_{m,reg.atlas_r}}{\mathrm{PPL}_{m,subj_r}} \right) \ , \tag{5.8}$$

where $\mathrm{PPL}_{m,subj_r}$ is the partial pathlength calculated using subject $r$ anatomy to guide photon migration in region $m$ (similarly for the registered atlas $reg.atlas_r$), as described in Equation 5.7. The ROIs colors ranging between light orange and light blue correspond to relative errors $< 45\%$; note that most of the ROIs relative errors fall in this range. A larger error is observed for Brodmann area 3a, 3b, and area MT, due to their small size and high localization variability [42, 5]; furthermore, errors $> 50\%$ are measured in regions 44 and 45 becuase of their large distance from the optodes (see Figure 5-8); the PPL error in the somatosensory Brodmann area 2 shows the same hemisphere localization asymmetry presented in Fischl et al. [42]; finally, area V1 deviation of 80% in the left hemisphere bank of the occipital lobe is due to the peculiar asymmetry of V1 in the MNI single subject atlas: the specific atlas anatomical asymmetries can be reduced by considering an average atlas for further studies.

In Figures 5-13 and 5-14 we show the population PPL means and standard deviations respectively; on the $x$ axis we indicate the center of each mini-probe (i.e., one of the 12 10-20 points, as shown in the probe design, Figure 5-6) and on the $y$

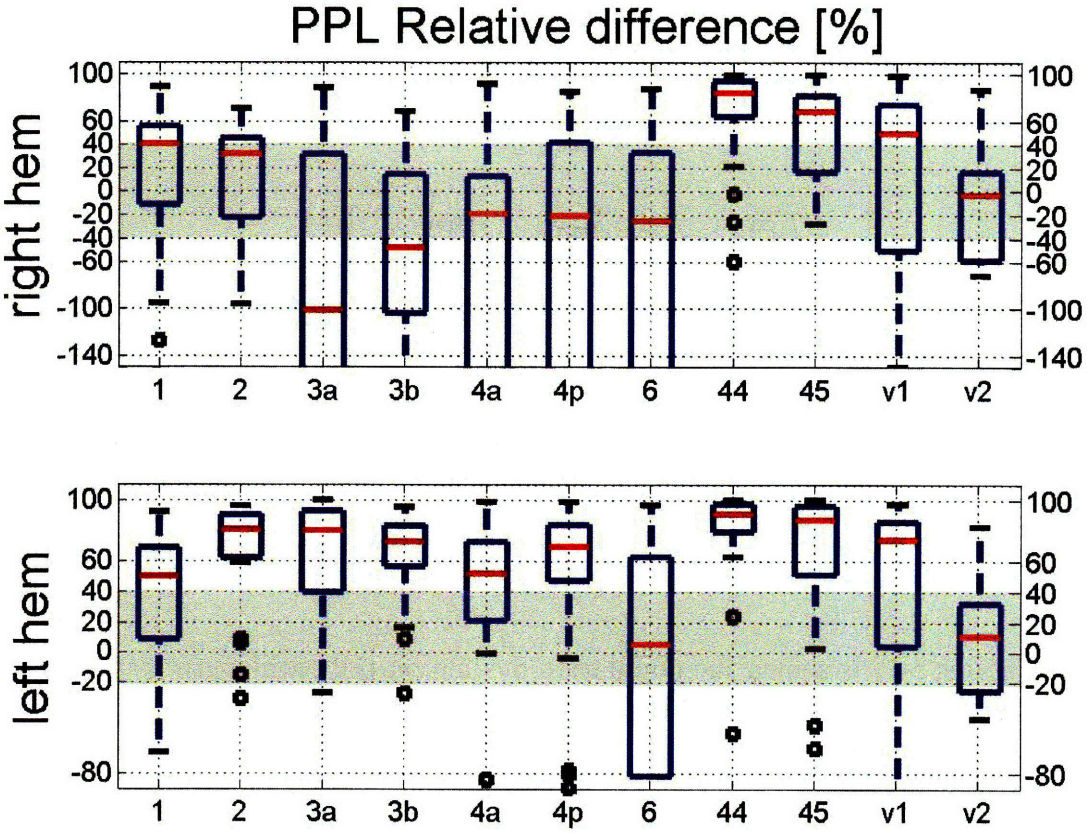


Figure 5-11: Box plot of the variability of PPL across the population (horizontal lines at the lower quartile, median (in red), and upper quartile values); the light gray boxes highlight errors between -40% and 40% for the right hemisphere (top row) and between -20% and 40% for the left hemisphere (bottom row). It is encouraging to notice that the median errors in the right hemisphere are less than 25% for the largest and best covered functional regions: motor (BA4) and pre-motor cortex (BA6) and the largest of the visual areas (V2); on the other hand, smaller, less visible regions (such as BA3b, BA44, and BA45 as shown in Figure 5-8, where we also see how far the optodes are from regions BA44, BA45, part of BA3b and V1) show an error of over 40%. Similarly for the left hemisphere, the smallest regions present errors between 45% and 87%, whereas the largest regions and the closest to the optodes, BA6 and V2, show errors smaller than 20%.

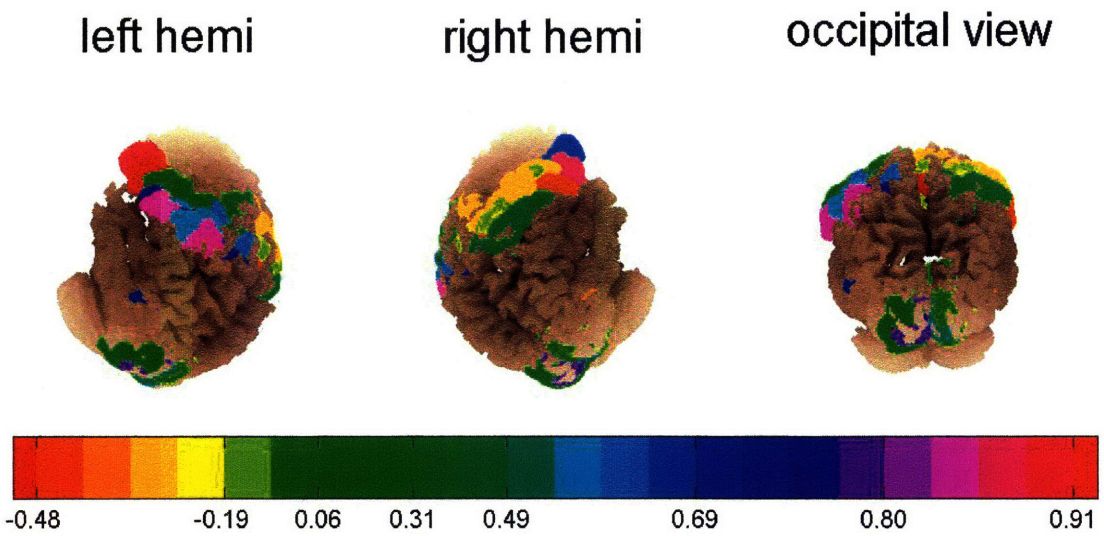


Figure 5-12: For each functional ROI are plotted three views of the population median of the relative difference between PPL measured on the subject anatomy and the PPL calculated using the registered atlas anatomy (see Equation 5.8). The ROIs colors ranging between light orange and light blue correspond to relative errors $< 45\%$; note that most of the ROIs are in this range, with the exception of the small Brodmann area 3b and MT, the small and ventral Brodmann area 3a, the regions 44 and 45 (that are too far from any optodes), area 2 (which displays the same hemisphere localization asymmetry shown in Fischl et al. [42]), and area V1 (whose deviation is due to the particular asymmetry of V1 in the MNI single subject atlas).

axis we report the names of the functional regions for which each mini-probe could provide PPL data. Note that for the other figures we have shown the PPL and PPL-related data from the mini-probe with the highest contribution to the measurement (see Equation 5.7); on the other hand, in Figures 5-13 and 5-14 we show the full spectrum of the data; it is interesting to notice that only the visual cortex (V1 and V2) has overlapping measurements (coming from mini-probe centered on O1/O2 and Oz, as is clearly visible from Figure 5-9). An extension of these plots is Table 5.1: here we list the means and standard deviations of population pathlength within each region of interest but we consider only the mini-probe with the highest PPL (for example, for region V2, right hemisphere, the subjects PPL mean value 6.78 mm comes from O2 and not Oz, whereas in Figure 5-13 the bottom right plot at the row for V2 reports the PPL mean calculated from both O1 and Oz). Analogous observations can be made for the standard deviation plot of Figure 5-14.

Table 5.1: Population PPL mean and standard deviation [mm]

| ROI | hem | Sbj PPL mean | Atl PPL mean | Sbj PPL std | Atl PPL std |
|---|---|---|---|---|---|
| 1 | R | 3.37 | 2.23 | 1.78 | 0.80 |
| 1 | L | 3.29 | 1.65 | 2.11 | 0.66 |
| 2 | R | 1.81 | 1.33 | 1.20 | 0.49 |
| 2 | L | 1.95 | 0.40 | 1.48 | 0.30 |
| 3a | R | 0.03 | 0.04 | 0.06 | 0.05 |
| 3a | L | 0.02 | 0.01 | 0.04 | 0.03 |
| 3b | R | 0.71 | 0.88 | 0.57 | 0.45 |
| 3b | L | 1.15 | 0.33 | 0.66 | 0.17 |
| 4a | R | 0.30 | 0.30 | 0.27 | 0.09 |
| 4a | L | 0.48 | 0.18 | 0.40 | 0.15 |
| 4p | R | 0.12 | 0.12 | 0.15 | 0.11 |
| 4p | L | 0.12 | 0.04 | 0.13 | 0.05 |
| 6 | R | 2.21 | 2.13 | 1.70 | 0.68 |
| 6 | L | 2.66 | 1.95 | 2.30 | 1.31 |
| 44 | R | 0.21 | 0.02 | 0.44 | 0.02 |
| 44 | L | 0.09 | 0.01 | 0.16 | 0.03 |
| 45 | R | 3.09 | 0.67 | 3.39 | 0.32 |
| 45 | L | 0.99 | 0.07 | 1.13 | 0.05 |
| MT | R | 0.04 | 0.06 | 0.07 | 0.05 |
| MT | L | 0.00 | 0.00 | 0.01 | 0.00 |
| V1 | R | 2.87 | 1.24 | 2.58 | 0.82 |
| V1 | L | 3.78 | 0.97 | 3.49 | 0.88 |
| V2 | R | 6.78 | 7.20 | 3.92 | 2.96 |
| V2 | L | 7.67 | 6.20 | 5.71 | 2.30 |

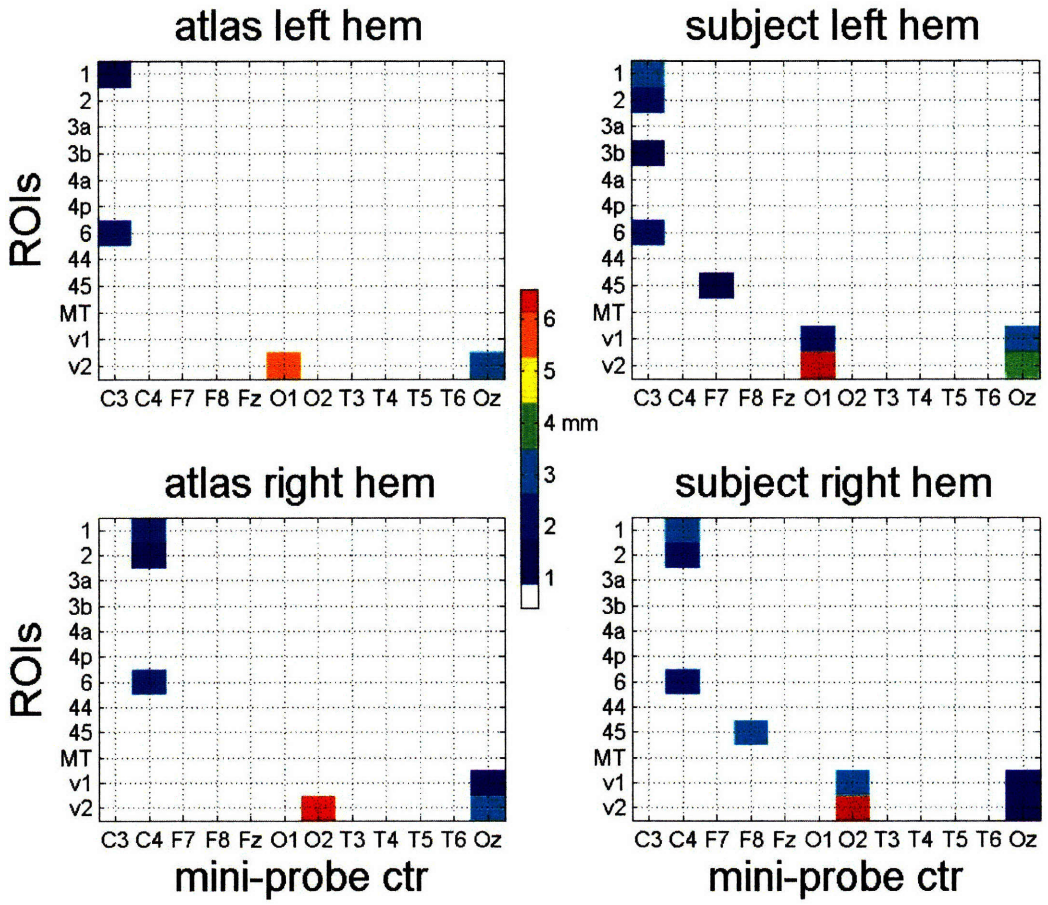


Figure 5-13: Population PPL means: on the $x$ axis we indicate the center of each mini-probe (i.e., one of the 12 10-20 points, as shown in the probe design, Figure 5-6) and on the $y$ axis we report the names of the functional regions for which each mini-probe could provide PPL data. Most mini-probes do not contribute to the PPL because they are too far from any ROI (note sparsity of the data).

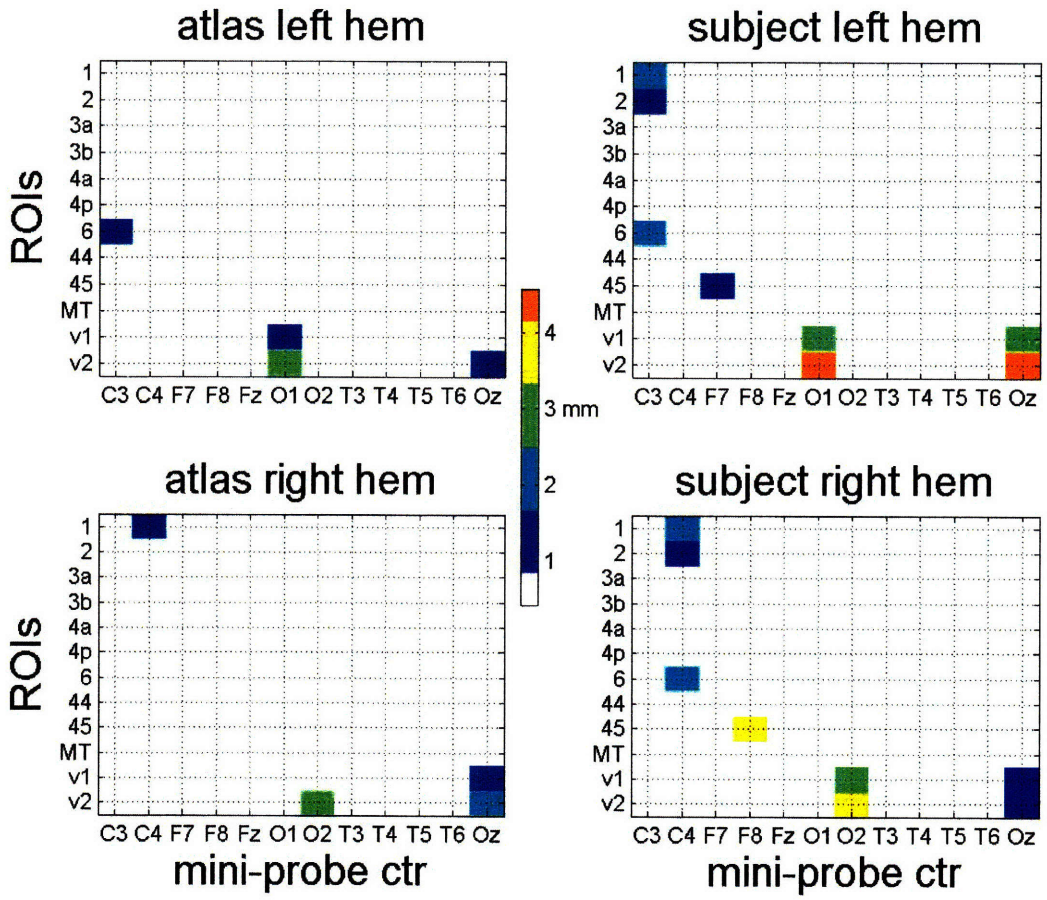


Figure 5-14: Population PPL standard deviations. Note that variation of PPL across the population of registered atlases is considerably smaller than that of the subjects, not surprisingly, because the atlas cortical anatomy is not locally changed by the affine transformation and therefore the measured PPL is quite similar for every registered atlas.

#### 5.2.4.3 Discussion

It is encouraging to notice that in Figure 5-11 the median errors in the right hemisphere are less than 25% for the largest and best covered functional regions: motor (Brodmann Area 4, or BA4) and pre-motor cortex (BA6) and the largest of the visual areas (V2), although the spread (hence variability across the population) of the PPL for BA6 is quite large; on the other hand, smaller, less visible regions (such as BA3b, BA44, and BA45 as shown in Figure 5-8, where we also see how far the optodes are from regions BA44, BA45, part of BA3b and V1) show an error of over 40%. Similarly for the left hemisphere, the smallest regions present errors between 45% and 87%, whereas the largest regions and the closest to the optodes, BA6 and V2, show errors smaller than 20%. The asymmetry of the two hemispheres is well explained by Figure 5-8: each subject's (here we show one, subject number 4) somatosensory areas are not symmetrically distributed and often times in (only) one hemisphere a region falls behind a cortical fold belonging to another region; an example is shown in the subject described in Figure 5-8a, the ventral region BA3a (in yellow) is mostly visible in the right hemisphere (right side of Figure 5-8), but in the left hemisphere is barely showing under the gyri where BA1, BA2, BA3b and BA6 lie. However, for the two largest regions (pre-motor cortex, BA6, and visual area V2), the two hemispheres consistantly show good agreement and an encouraging small median difference between subject's and atlas' PPL. Moreover, as shown in Figure 5-10, in most regions the wide spread of the PPL data (elongated rectangles in the box plots) is less emphasized in the registered atlas, where the PPL fluctuations within regions are smaller. Moreover, at least two ROIs, BA1 and V2, showed good agreement in both hemispheres in spatial distribution, median and mean values across the population, and spatial spread, between the subject-guided and registered atlas-guided PPL measurements; not coincidentally, these two regions are the most consistently closer to a mini-probe (see Figure 5-8, the red and dark magenta regions).

The hemisphere asymmetry is confirmed by the data shown in Tables B.1 and B.3: for example the PPL of BA45 and V2 are higher in the right hemisphere (top row) than the left hemisphere (7.60 mm and 9.02 mm for BA45 and V2 in the right hemisphere respectively, versus 2.42 mm and 5.43 mm in the left one): in Figure 5-8 it is clearly visible that these regions (BA45 in blue and V1 in magenta) are closer to an optode (black dots) in the right hemisphere than in the left one. Therefore, the hemisphere asymmetries present in the subjects' anatomies affect the PPL relative differences because they do not appear as significant on the registered atlases (they are mostly local asymmetries, not captured by the global cortical affine transformation used for registration). Therefore, we believe a further improvement in a purely optical imaging protocol will come from the employment of an average atlas (which is, generated from population MRI averaging) as opposed to a single subject atlas.

The PPL plots (Figure 5-10 and 5-11) emphasize the intrinsic variability across the population of the spatial distribution of the region of interests (as discussed in Section 4.3.5.2 and shown in Table B.3), in agreement with the findings of Fischl et al. [42]; Figure 5-12 highlights the impact on optical measurements (such as PPL) of

the optodes location relative to the functional regions we are interested in imaging. Our results suggest that a more careful design of a probe and probe placement (not constrained by the locations of the EEG 10-20 landmarks) with respect to the type of functional experiments performed will significantly improve stability and repeatability of the optical measurements acquired with the use of a general anatomical model. However, even the current optodes setup provides a sufficiently accurate spatial distribution of sensitivity to absorption changes within most of the regions of interest, as shown in Figures 5-10 (note that the red boxes are mostly contained within the blue ones), 5-13 and 5-14 (note that the colored points on the subjects plots – right top and right bottom plots – are a super set of these on the atlases': they do not match the PPL mean and standard deviation amplitude but they have a larger spatial distribution than the atlases).

An interesting result from this study is the analysis of the population variability of optical path length on a functional area. We analyzed our database of 31 healthy subjects and measured the PPL on each of our selected 24 functional regions and compiled Table B.1 with these findings. The first column of the table identifies the subject by number followed by an "R" or an "L" for right or left hemisphere respectively. The remaining eleven columns refer to 11 of the 12 regions of interest we investigated (region MT has been omitted because of lack of signal). The data filling the table are the PPL in millimeters as measured by the highest contributer mini probe (see Equation 5.7), and the 10-20 point center of such mini probe is specified in the table. This table is complemented by Table B.3, where are listed the anatomical structures underlying each optode position; the data shown in the table are obtained by projecting each optode scalp-location onto the cortex using the algorithm described in Okamoto et al. [100]; the anatomical structures are calculated as described in Desikan et al. [35]; the first and second columns of the table indicate the 10-20 point center of the mini-probe analyzed and its general location (left-hemisphere/right-hemisphere/central sulcus); the third column reports the anatomical structure onto which the four optodes forming the mini-probe project; the last four columns show each mini-probe optode frequency count (which is, the number of subjects (out of the 26 analyzed) for which that optode projects onto the structure specified in the third column). The tables show the variability across the population of the PPL (Table B.1) mostly due to the intrinsic variability of the ROIs locations, which are identified by specific anatomical structures [42, 35] (Table B.3), in agreement with the findings of Amunts et al. [5] and Fischl et al. [42].

### 5.2.5 Experimental results

We complete the validation of our atlas-based brain imaging protocol by presenting the reconstructed activation maps (solution of the DOT inverse problem) on three experimental subjects. For these physical subjects we acquired anatomical MRI, personal information and optical measurements of the motor cortex during event-related median-nerve stimulations. The physical probe designed for this experiment (see Figure 5-15), visible on the MRI, was mapped onto the synthetic atlas scalp using

the $SLR_{10\text{-}20}$ registration algorithm (see Chapter 4). We then proceed by simulating photon migration (solution of DOT forward model) on the registered atlas and use the sensitivity matrix thus obtained to solve the DOT inverse problem and compare the calculated brain activation map with that measured using the subject specific anatomical model. These experiments are used for validation purposes; in a truly experimental setup as we envision it, acquiring the subject's anatomical MRI will not be necessary, as the probe location and the 10-20 points locations used in $SLR_{10-20}$ will be calculated using a 3D digitizer (as commonly done in EEG).

#### 5.2.5.1 Dataset

For this study, we measured simultaneous recordings of DOT and pulsed Arterial Spin-Labeling MRI (pASL) during somatosensory cortex stimulation in humans. Optical tomography was performed using a continuous wave system (CW4, TechEn Inc.), with 8 source-positions (2 wavelengths each, 690 and 830 nm) and 10 detectors in an array of 2 columns of light sources interleaved with 2 columns of light detectors. For analysis, data was downsampled to 10 Hz, band-pass filtered between 0.01 and 0.5 Hz and the optical intensity was converted to chromophore concentration changes using the modified Beer-Lambert law. pASL data was acquired with a 3T Siemens Allegra MR scanner (Siemens Medical Systems) using PICORE labeling geometry with Q2TIPS saturation to impose a controlled label duration (700 ms). This scheme also allowed us to estimate BOLD from the ASL. We collected 10 slices with repetition and echo times at 2 s and 20 ms, respectively. Anatomical scans were also obtained using a T2-weighted MPRAGE sequence (1 x 1 x 1 mm resolution, TR/TE/$\alpha$ = 2.53 s/1.64 ms/7$^o$).

The stimulation protocol consisted of event-related median-nerve stimulation, at motor threshold of the right thumb movement, in 7 healthy right-handed subjects (28 $\pm$ 4 years old). The duration of the stimulus varied from 1 to 4 seconds, always at 3 Hz. Acquisition was divided into 5 runs of 6 minutes each, representing a total of 50 trials per condition for each subject (ISI varied from 6.6 to 10.8 seconds). Of these seven subjects, the three with highest Contrast to Noise Ratio (CNR) were selected for validation of the purely optical imaging protocol here proposed; the selected subjects' age and gender are shown on Table 5.2.

We use the MNI single subject atlas as our general anatomical model and we create a database of 3 atlases registered to each subject with our $SLR_{10\text{-}20}$ algorithm and with a modified CSF thickness to match that of the subject to which they are registered; for a detailed description of the atlas see Section 4.2.1.

Table 5.2: Experimental subjects' Dataset

| **Sbj** | age | gnd |
|---|---|---|
| 34 | 24.89 | M |
| 36 | 34.53 | M |
| 37 | 30.79 | M |

#### 5.2.5.2 Methods

The experimental probe is designed to cover the left hemisphere motor and pre-motor cortex. The probe comprises eight sources (red) and eight detectors (white) in a 4x4 grid. Each detector/source is 2 mm apart from the closest detector/source and 3 mm apart from the closest source/detector, as shown in Figure 5-15a. We extract the approximate locations of the physical optodes from the anatomical MR scan and then we project these locations onto the surface of the head toward the Anterior Commissure point (see Figure 5-15b: the locations of the eight sources in shown in red, whereas the blue circles indicates the detectors locations). We then proceed similarly for the registered atlases, starting with the same approximated locations of the optodes showing on the subjects' MR scans and proceeding by projecting them onto the registered atlases scalp surfaces; the source-detector distance of 3 mm is chosen to maximize SNR while still probing the cortical surface.

The atlases are registered to the subjects using our $SLR_{10\text{-}20}$ algorithm which entails the manual extraction of the four initial anchor points, Nz, Iz, A1 and A2 from the MNI atlas and the subjects MRIs. Alternatively, the subjects' four anchor points locations could be acquired using a commercially available 3D digitizer and therefore the use of the subjects anatomical MRIs could be completely avoided. Using the four initial points we proceed by calculating the locations of the other 10-20 points locations on the subjects and the atlas using Jurcak et al. virtual 10-20 algorithm [76]; this step also could be performed on the subjects using a 3D digitizer instead of the subject scalp mesh extracted from the anatomical MRIs. From the set of 10-20 points on the subjects and the atlas, we can estimate the affine transformation $T$ as described in details in Section 4.2.3. The follow up steps are similar to these performed for the study of Section 5.2 and they are described in Figure 5-4:

1. We apply $T$ to the atlas meshes and volumes to obtain three registered atlases (Figure 5-4A);

2. We modify the registered atlases CSF thickness using dilation/erosion to match the corresponding subject median CSF thickness as estimated from the subject's age according to the linear model shown in Figure 5-5);

3. We map the physical probe on the registered atlases as described previously in this section (Figure 5-4B);

4. We simulate photon migration on the registered atlases (and on the subjects, for validation purposes) using a Monte Carlo based algorithm [16] (Figure 5-4: B connecting to the "Sensitivity matrix" box via the M.C., Monte Carlo, arrow);

5. We acquire baseline (rest state) and activation (median-nerve stimulation) optical measurements on the subjects (Figure 5-4: b connecting to the "Optical measurements" box via the DOT arrow);

6. We solve the DOT inverse problem (ill posed because underdetermined) by solving the regularized least square solution of minimum norm which is given by the expression:

$$\hat{x} = min \left\| B_{atl} x - y \right\|^2 + \tau \left\| x \right\|^2 \ ,$$

where $B_{atl}$ is the sensitivity matrix from the solution of the DOT forward problem (which is, the Monte Carlo simulation of photon migration) using the registered atlas and multiplied by a binary map of the brain voxels giving the following result:

$$b_{i,j} = \begin{cases} a_{i,j} & \text{when voxel } (i,j) \text{ is labeled gray or white matter} \\ 0 & \text{otherwise} \end{cases} \ ,$$

$a_{i,j}$ are the elements of the sensitivity matrix $A_{atl}$ (see Equation 1.17), $\tau$ is the scalar Tikhonov regularization parameter [14, 9] and $\tau = \alpha * \max(B_{atl_{i,i}} B^T_{atl_{j,j}})$, for $\alpha = 0.01$ [19], $y$ is the detected fluence vector normalized by each source-detector gain (to eliminate the bias due to detectors gain adjustments to maximize SNR) and minus the baseline fluence, and $x$ is the activation map, which is, a voxel-size vector of changes in absorption coefficient. We calculate the numerical expression for $\hat{x}$ as follows [9, 19]:

$$\hat{x} = B^T_{atl}(B_{atl} B^T_{atl} + \tau \sigma_y^2)^{-1} y \ ,$$

where $\sigma_y^2$ is the measurement covariance matrix (assumed to be diagonal) [19]. For validation purposes, we solved $\hat{x}$ also for $B_{sbj}$, which is the sensitivity matrix calculated using the subject anatomy to guide the photon migration simulation.

#### 5.2.5.3 Results and Considerations

We calculated the changes to absorption coefficient $\mu_a$ due to the vascular effect of neural activity in a sub-volume of the subject and registered atlas' heads and we show the results in Figure 5-18 for one subject, and Figures 5-17, 5-19, and 5-20 for another experimental subject. In Figure 5-16 we show a visual representation of the results for one subject: the subject (left image) and corresponding registered atlas (right image) activation maps are overplotted the cortical surfaces (pink shade), the scalp surfaces are colored in light gray and the sources (blue) and detectors (black) locations are also shown; the darker gray sections indicate the relative location of the sub-volumes in which the heads have been cropped for a more efficient computation.

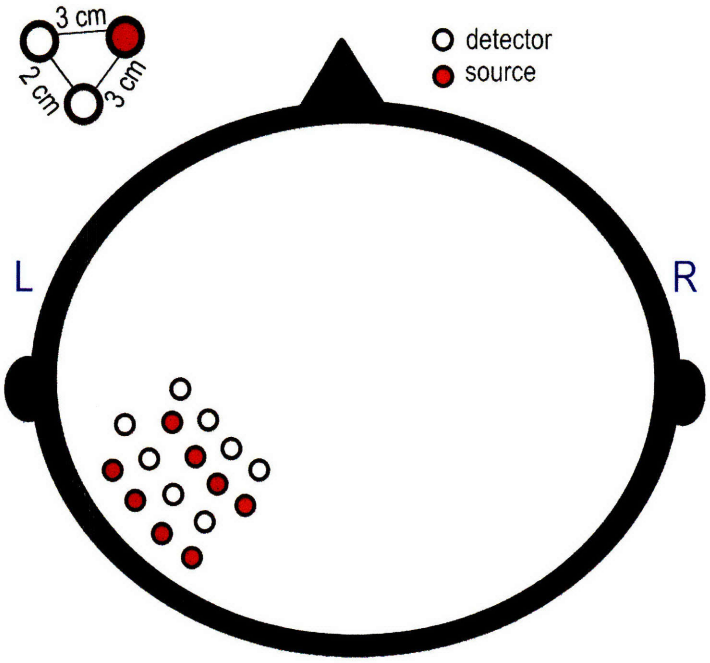


(a)

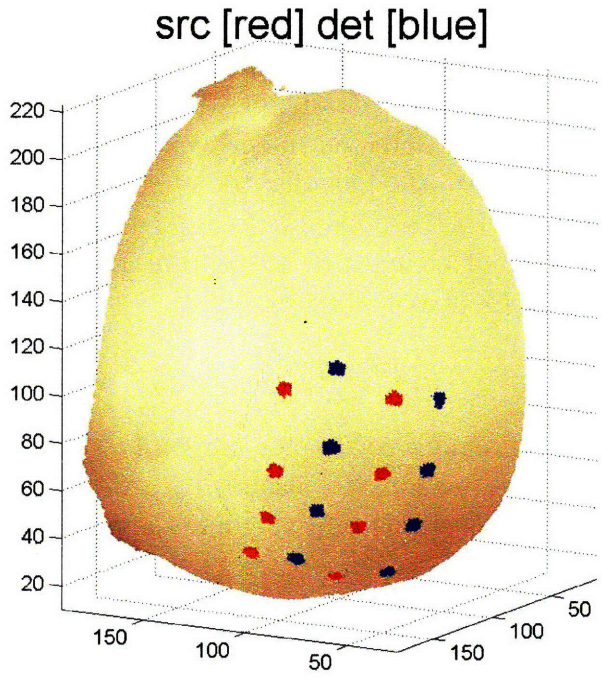


(b)

Figure 5-15: (a) The experimental probe is designed to cover the left hemisphere motor and pre-motor cortex. The probe consists of eight sources (red) and eight detectors (white) in a 4x4 grid. Each detector/source is 2 mm apart from the closest detector/source and 3 mm apart from the closes source/detector. (b) The actual location of the source (red) and detectors (blue) on one of the registered atlases; the source-detector distance of 3 mm is chosen to maximize SNR while still probing the cortical surface.

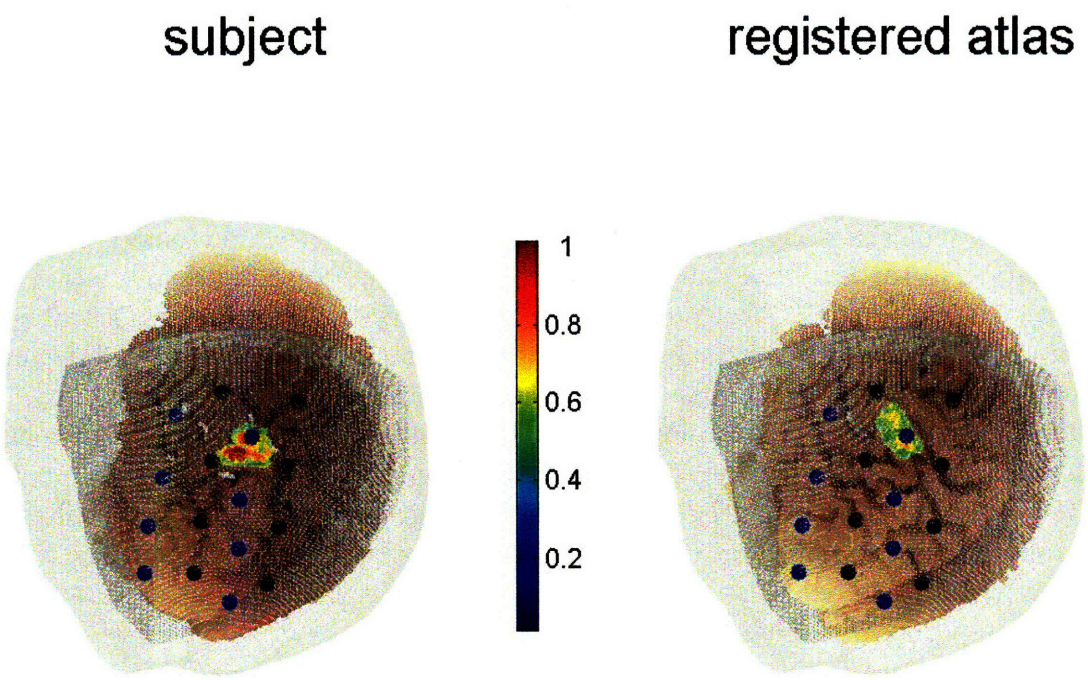


Figure 5-16: Localizing activation: the subject (left) and corresponding registered atlas (right) activation maps are overplotted the cortical surfaces (pink shade) and the scalp surfaces are colored in light gray; the sources (blue circles) and detectors (black circles) locations are also shown; the darker gray sections indicate the areas of data analysis, which is, the sub-volumes in which the heads have been cropped for a more efficient computation. The activation contrast has been normalized at FWHM.

The activation contrast has been normalized at FWHM (colorbar is dimensionless), for better visualization and to focus the comparison between subject- and atlas-based reconstructions to the spatial localization rather than the signal amplitude.

In Figure 5-17a-b and 5-18a-b are shown the vascular response to brain activity for two experimental subjects and their corresponding registered atlases. The top rows show the normalized reconstructed changes in absorption coefficients (in the left column the subject and in the right column the atlas registered to it using $SLR_{10\text{-}20}$), whereas the bottom rows show the activation maps overlapped to the location of the 24 functional ROIs. It is easy to notice that the reconstructed activation using subject-specific or atlas anatomy is localized in the same gyrus: for the subject described in Figure 5-17a-b the activation peak is in the post-central gyrus, where the primary somatosensory areas lie (mainly BA1, BA2, and BA3b), as expected from a typical median-nerve stimulus; in the subject analyzed in Figure 5-18a-b, instead, the activation focus is found in the posterior bank of the post-central gyrus (corresponding to the secondary somatosensory area, or SII) in both subject-guided and atlas-guided reconstructions; the lack of source-detector pairs probing more frontal regions is likely the main cause of the absence of vascular response in the primary

somatosensory area (see Figure 5-16).

Figures 5-19a-b and 5-20c show an axial, sagittal and coronal slice (respectively) for brain activation reconstructed using the subject specific anatomy (left columns) and the registered atlas anatomy (right column). Note that the activations have been normalized (colorbar dimensionless) and that there is no activation outside the brain boundary due to the brain constraint introduced to increase depth resolution (see Section 5.2.5.2 point 6). We could not apply the cortical constraint as described in Boas et al. [19] because the subject brain segmentation (obtained with FreeSurfer watershed algorithm [1]) yields a remarkably thin gray matter compared to that defined on the registered atlas (note the black contour lines) resulting in a significantly different subject/atlas depth resolution. As shown in Figure 5-18 and in more details on the slices plots, using an atlas to guide photon migration does not affect localization of brain activation: note that the position of the activation focus is not exactly the same on the registered atlas, but it is rather on the same anatomical structure (a particular gyrus), which has three wide folds in the subject coronal slice (see Figure 5-20 left image), and only two folds in the atlas' (see Figure 5-20 right image), resulting in a more peaked activation on the subject-based model. The spatial accuracy of the reconstructed vascular activity is confirmed by all the experimental subjects.

### 5.2.6 Conclusions

In this chapter we describe an imaging protocol that uses solely Diffuse Optical Tomography to reconstruct brain activation. The approach consists of using an atlas-based anatomical model instead of the subject's anatomy and simulating photon migration on the atlas model (DOT forward model) while acquiring optical measurements from the subject, and then reconstructing the location of cortical activation (by solving the DOT inverse problem). The benefits of this novel method comes from the elimination of the need for MRI, and its associated issues (such as high costs, possible subject's discomfort and claustrophobia during the MR anatomical scan, prohibiting studies on neonatal subjects, lack of portability).

We first present a preliminary study using one single subject registered to an atlas using MRI-based registration (Section 5.1). We validate our claim that an atlas can be a suitable substitute to the subject specific anatomical model by comparing the simulated optical measurements obtained using the subject specific anatomical model versus the generic adult human head model. The most relevant measurement, the partial pathlength within the brain, indicates that such anatomical approximation can be used without introducing a significant error (relative error $\leq 10\%$), provided that a suitable atlas is selected.

The preliminary study is limited by the size of the dataset (one subject and one atlas) and by the use of a registration algorithm that still needs MR anatomical information. The natural development of the idea of using a general anatomical model in place of the subject specific is described in Section 5.2. Using a dataset of 31 healthy

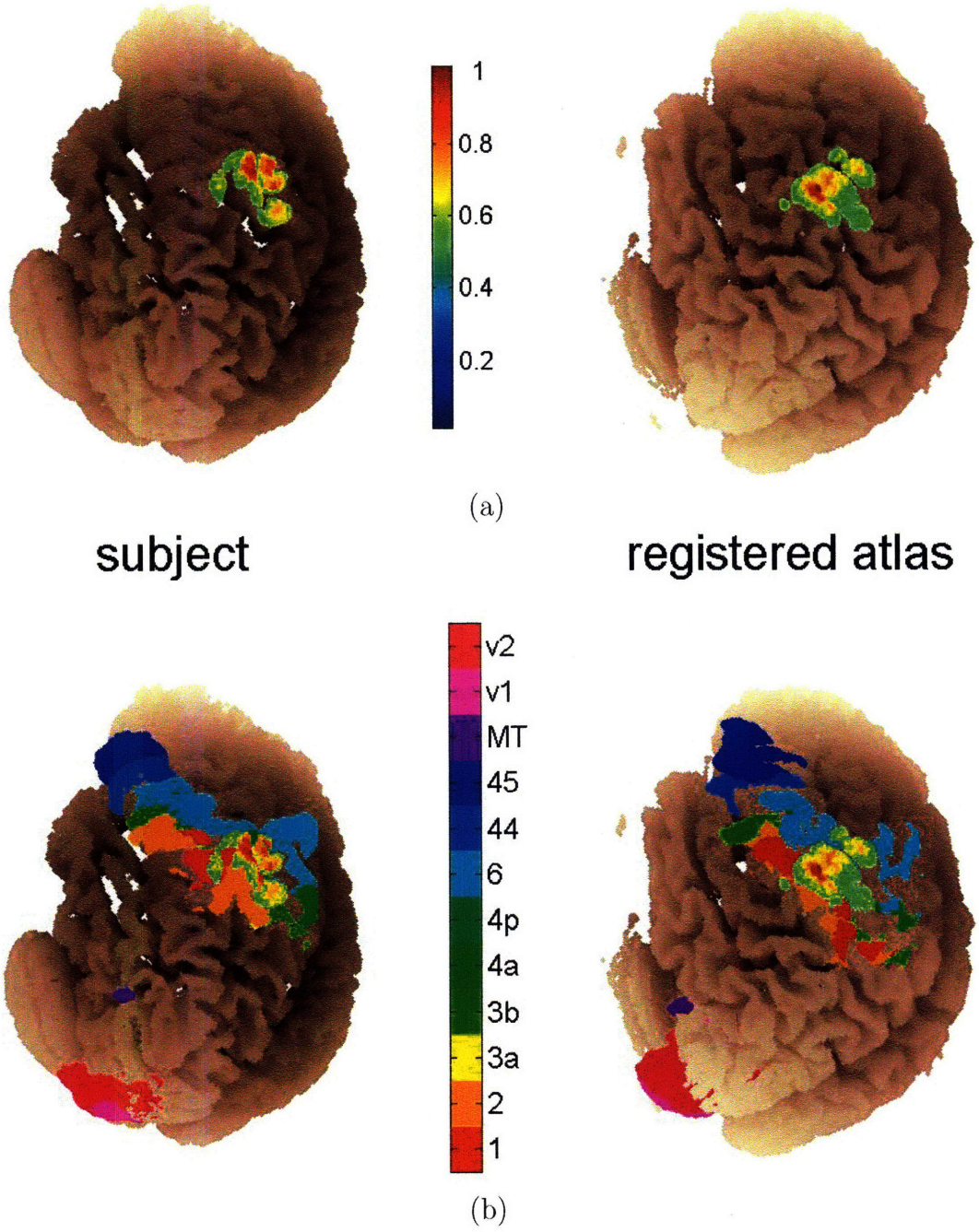


Figure 5-17: Localizing vascular response to brain activation in subject 1: (a) the subject (left) and corresponding registered atlas (right) activation maps are overplotted the cortical surfaces (pink shade). The activation contrast has been normalized at FWHM (full width at half maximum), for better visualization and to focus the comparison between subject- and atlas-based reconstructions to the spatial localization rather than the signal amplitude. (b) The reconstructed activation is overplotted the functional ROIs, labeled as the colorbar indicates, showing that the primary somatosensory area (SI) activates during median-nerve stimuli, as expected.

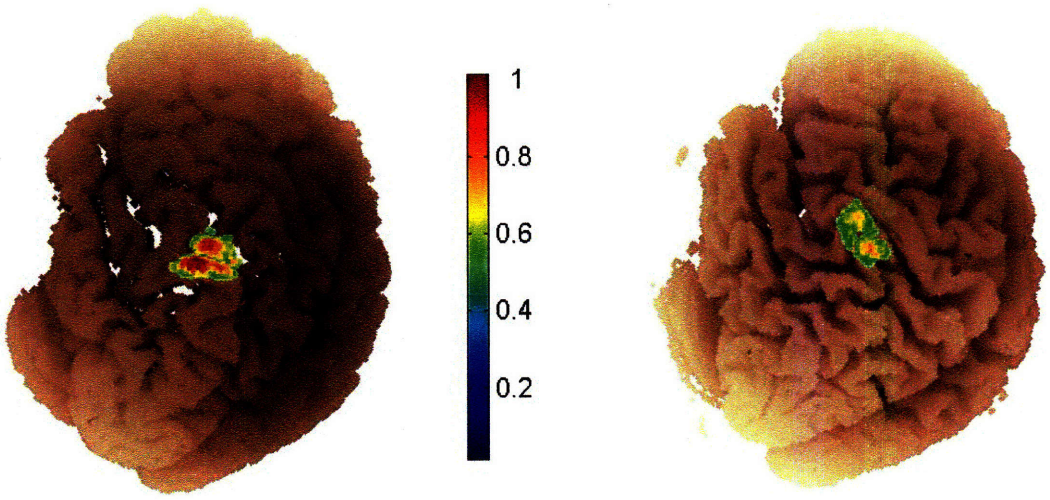


(a)

subject

registered atlas

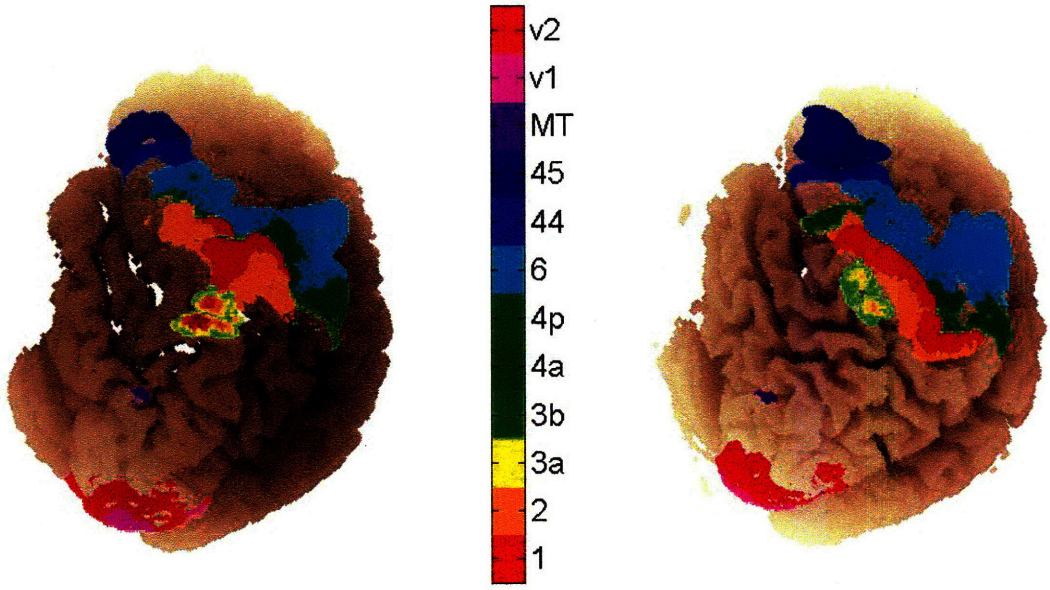


(b)

Figure 5-18: Localizing vascular activity in subject 2: (a) the subject (left) and corresponding registered atlas (right) activation patterns are mapped on the cortical surfaces (pink shade). The activation contrast has been normalized at FWHM (full width at half maximum) at therefore the colorbar is dimensionless. (b) The reconstructed activation is overplotted the 24 functional ROIs, showing that the secondary somatosensory area (SII) respond to median-nerve stimuli.

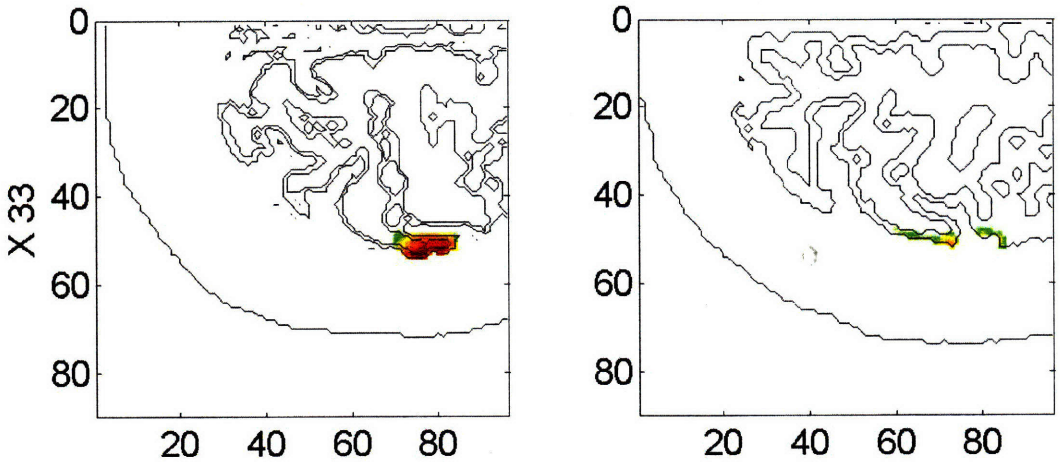


(a)

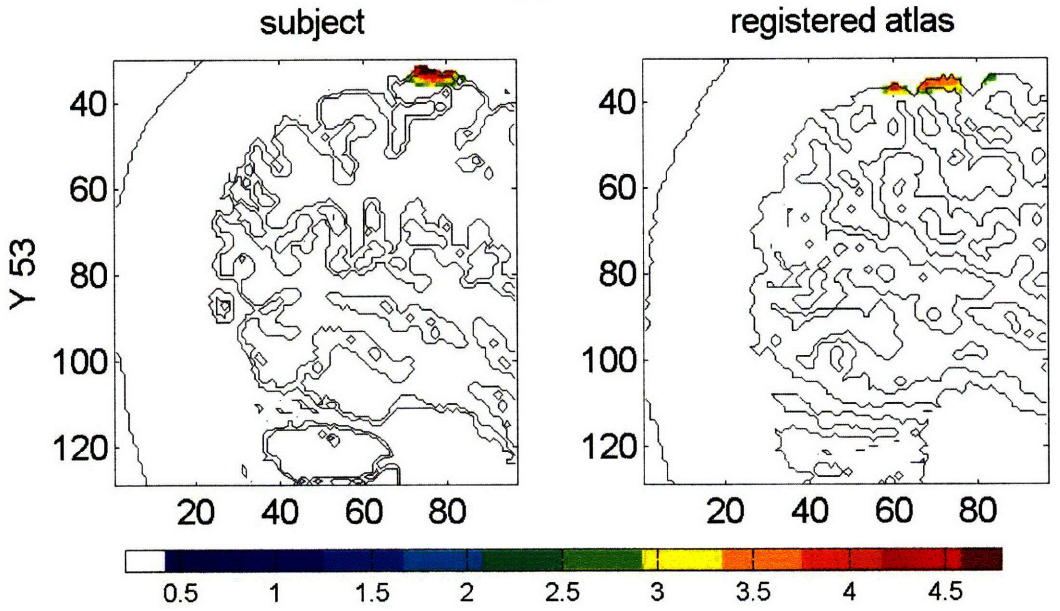


(b)

Figure 5-19: An axial (a) and a sagittal (b) slice of the subject (left image) and the registered atlas (right image) showing the reconstructed brain activation using the subject specific anatomy and the registered atlas anatomy respectively; the black contour lines identify the boundaries of the scalp, gray and white matters. Note that the activations have been normalized (colorbar dimensionless) and that there is no activation outside the brain boundary due to the brain constraint introduced to increase depth resolution (see Section 5.2.5.2 point 6). We could not apply the cortical constraint as described in Boas et al. [19] because the subject brain segmentation (obtained with FreeSurfer watershed algorithm [1]) yield to a remarkably thin gray matter compared to that defined on the registered atlas (note the black contour lines).

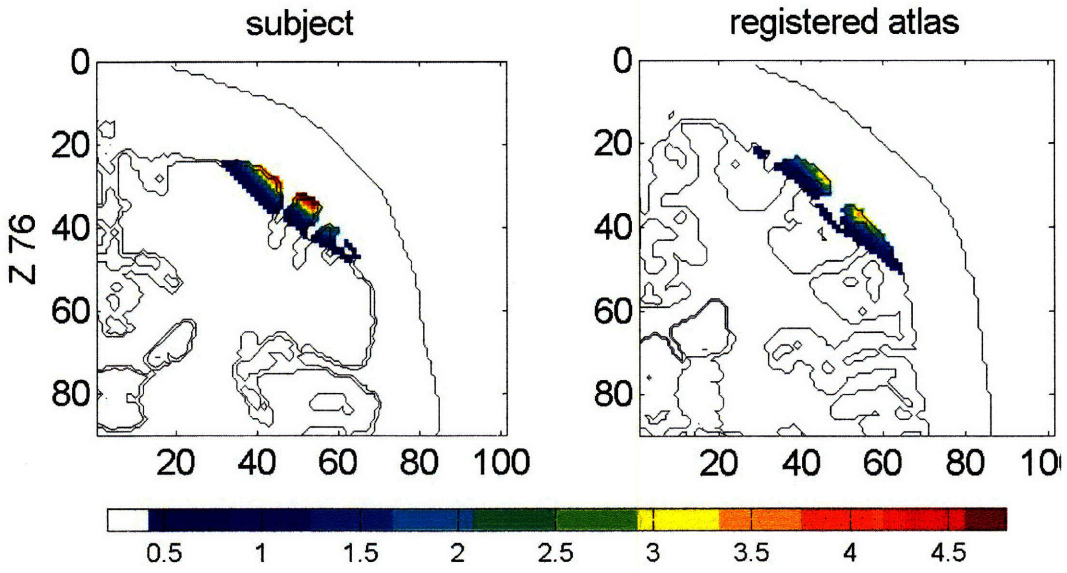


(c)

Figure 5-20: (c) A coronal slice (Z = 73) of the reconstructed activation using the subject specific anatomical model (left image) and the general atlas model (right image); the black contour lines identify the boundaries of the scalp, gray and white matters. As shown in Figure 5-18 and here in more details, using an atlas to guide photon migration does not affect localization of brain activation: note that the position of the activation focus is not exactly the same on the subject and on the registered atlas, but it is rather on the same anatomical structure (a particular gyrus), which wider in the subject (left image) than in the atlas (right image), resulting in a more peaked activation on the atlas-based model.

human subjects, we measure sensitivity to absorption changes (solution of the forward model) on a chosen set of 24 functional Region Of Interests (ROIs) and compare the results obtained using the registered atlas versus these calculated using the true subject's anatomical model on a dataset of 31 healthy subjects. The new registration algorithm, based on superficial landmarks, is described in Chapter 4. The registered atlas' CSF thickness is modified according to the subject's age the atlas is registered to, following up the study of Chapter 2. Moreover, we solve DOT forward and inverse problem on three experimental subjects: optical measurements are acquired on the physical subjects and photon migration is simulated on both the subjects' heads and on the atlases registered to the experimental subjects using $SLR_{10\text{-}20}$; the inverse problem is solved using the subject's data and the reconstructed activation map is compared to that calculated guiding DOT forward model with the registered atlas: the qualitative results (see Figures 5-19 and 5-20) show that the activation focus is localized in the correct gyri using the atlas model, although the subject and atlas cortical geometry is not exactly the same and the activation level of contrast is different. Overall, we showed that is possible to use a general anatomical model to represent a subject's to guide DOT forward model to localize the macroanatomical structure of activation, provided the atlas CSF thickness is customized to match that of the subject represented. The activation reconstruction accuracy on atlas-based DOT is limited to the localization of the activation focus with macroanatomical structure spatial precision (sulci/gyri); therefore, our purely optical imaging protocol is not suitable when desiring a higher spatial resolution (which is not a typical scenario in optical tomography) or when lacking a suitable atlas to represent the specific subject (for example patients with brain lesions in unknown locations or of unknown size). Therefore, in most cases it it possible to obtain accurate optical activation maps while avoiding the costs and logistics of acquiring an anatomical MRI scan of a subject, as shown for our experimental subjects (see Section 5.2.5).

Further improvements of this work include the use of an average atlas instead of the MNI single subject to ensure less anatomical specificity (for example in identifying the functional regions of interest) and therefore a better representation of population anatomical variability. Moreover, the optical probe can be better designed to maximize coverage of the regions of interest; in our study from Section 5.2.4 we designed the probe shown in Figure 5-7 because of its direct relationship with the 10-20 scalp landmarks and because longitudinal studies are easier and more accurate when referencing to a standard scalp-landmarks system; however, in an experimental setup, any optodes configuration can be digitized and transfered to the atlas.

# Chapter 6

# Conclusions

Our main contributions outlined in this thesis include the design of an improved Cerebral Spinal Fluid (CSF) segmentor and a novel Superficial Landmarks-based Registration (SLR) algorithm that are used in the purely optical image process we propose. From our overall results it follows that: (1) CSF thickness, enhanced by our segmentation algorithm, and cortical depth can be used to study non-invasively neurodegeneration and its treatments; (2) the SLR algorithm can be used to improve portability of EEG when used in conjunction with a general conductivity model (atlas); (3) the CSF thickness and cortical depth longitudinal study confirms brain atrophy as an effect of aging; (4) a faster DOT forward problem solver can be used for time-resolved applications, making possible on-line data analysis; (5) brain activation can be accurately localized using a general head model to guide the photon migration simulation.

As reported in this thesis introduction (see Section 1.2), we repeat here a summary of our main contributions and findings and conclude by outlining possible directions of future work.

## 6.1 Cerebral Spinal Fluid role in Diffuse Optical Tomography

To the best of our knowledge, studying the effect of Cerebral Spinal Fluid (CSF) measurements of brain activity has never been done before because CSF does not affect significantly other functional imaging technologies (such as fMRI) and because investigating CSF-induced effects requires having access to its accurate anatomical model, which is difficult to obtain as its MR intensity range is not unique. Our contributions in this field include the design and testing of a semi-supervised segmentation algorithm tailored to accurately identify CSF and bone from T1 weighted multi-flip angle anatomical MRIs (see Section 2.3.2.1). Moreover, we investigate the impact of CSF scattering coefficient ($\mu_s'$) on DOT forward model as it greatly affects optical measurements (see Section 2.1). We successfully validated the hypothesis that varying CSF $\mu_s'$ from zero up to the order of the typical CSF inverse line-of-sight distance, or about 0.3 $mm^{-1}$, does not affect significantly sensitivity to absorption changes in

the brain; this hypothesis is key for applying the diffusion equation (and hence its more computational time efficient analytical solvers) instead of the radiative transit equation to describe photon migration in the human head (see Chapter 3). Furthermore, we study the effect of CSF thickness on DOT measurements (see Section 2.2) and find that a 50% change in CSF thickness produces small errors (less than 15% for source-detector separation $< 32$ mm). Consequent to these findings, we investigate the variability of CSF thickness across population (see Section 2.3) hoping to find a link between personal data (such as gender and age) and CSF thickness, which would lead to the possibility of customizing a generalized anatomical head model (atlas) to replace a specific subject anatomy in the DOT forward model (see Chapter 5). Our results show that CSF thickness is highly correlated with age (p value $< 0.005$), whereas gender has no bearing on CSF thickness. Our collective studies yield these conclusions and main contributions:

1. we provided evidence validating the hypothesis that CSF scattering coefficient can be approximated at $\sim 0.3$ mm$^{-1}$with errors less than 20% in time-domain and continuous wave; consequently, diffusion approximation based solutions of DOT forward problem can be used, greatly improving the computational run time (from $\sim$ 12 hours to few minutes);

2. we designed a novel CSF/bone accurate segmentor that can be used to model human head's tissue types for the EEG, MEG and DOT forward problems;

3. we investigated the age and gender relationship with CSF thickness and found that only age is highly correlated with CSF; this results lead to a linear model of age versus CSF thickness that can be used to customize a general anatomical model of the human head to represent the subject's specific in order to achieve a purely optical tomographic image process;

4. our more accurate CSF segmentor enables us to perform longitudinal studies of CSF thickness to investigate neurodegeneration and test the efficacy of various treatments as done in cortical thickness studies [31, 73, 4, 50, 58, 37, 107, 78, 117, 61, 20, 79, 124, 123, 104, 83].

## 6.2 Faster solver of DOT forward model

An accurate photon migration model is key for a reliable solution of the DOT inverse problem that leads to brain activation maps. The most accurate mathematical model describing photon migration is the Radiative Transfer Equation (RTE), but unfortunately an analytical solution of the RTE is not known and therefore the RTE is solved numerically by using accurate but computationally expensive Monte Carlo based algorithms. In Chapter 3 we investigate the applicability of a faster alternative to a Monte Carlo numerical solution of the RTE (see Equation 1.8) based on the Diffusion Approximation (DA) (see Equation 1.14). For validation purposes, we compare the performances of the Monte Carlo (MC) simulator proposed by Boas et al. [16] with these of the Finite Difference (FD) algorithm presented by Barnett at

al. [13] that solves Diffusion Approximation analytically. Our results show that the Finite Difference approach to the diffusion equation offers greater computational efficiency, but at the cost of modeling accuracy: in particular partial pathlength within the brain measured in continuous-wave using FD introduces an error between 20% and 40% with respect to the pathlength predicted by MC. The time-resolved data are more encouraging, though, suggesting that a Time Domain DOT instrument can succesfully take advantage of a more efficient solution of the Diffusion Approximation of photon migration as long as the first few data points are discarded and the separation between source and detectors is sufficient to probe the brain (errors less than 12% at source-detector distances over 28 mmand after 1.4 ns). Therefore, we conclude that diffusion based methods can well predict photon scattering through the human head provided that a realistic head model is used and the probe is designed to maximize Contrast to Noise Ratio (CNR) in the brain.

## 6.3 Non-volumetric registration algorithm

In Chapter 4, we describe a novel method, $SLR_{10\text{-}20}$, to register a general head model to a specific subject's head based on alignment of superficial landmarks (the EEG 10-20 electrodes system) and we validate it against the subject's anatomical MRI (our ground truth) and against the commonly used volumetric affine registration method available in the Statistical Parametric Mapping (SPM5) toolbox [3]. We analyze a dataset of 32 healthy subjects' MRIs and the MNI single subject atlas (see Section 4.2.1); we describe the superficial landmarks system adopted (the EEG 10-20 international system) and how it is used to estimate the affine transformation matrix (see Section 4.2.3 and the virtual 10-20 algorithm designed by Jurcak et al. [76]); then we present several validation metrics: (1) we compare the surface meshes/volumes of the subjects normalized to the atlas using SPM5 and $SLR_{10\text{-}20}$; (2) we compare the two registration algorithms' performances in surface landmarks preservation, (3) in cortical depth preservation, and (4) CSF thickness preservation; finally, (5) we test our registration algorithm for the preservation of cortical landmarks against "ground truth" (which is, the location of the same landmarks on the un-registered subjects).

Overall, $SLR_{10\text{-}20}$ performs better than SPM5 in preserving mesh, volumes and superficial landmarks; its accuracy in mapping cortical landmarks is not worse than the intrinsic variability of macroanatomical and cytoarchitettonical structures across subjects [40] (see Table B.3), suggesting that $SLR_{10\text{-}20}$ is well suited to register to a specific subject's head a general anatomical head model which is then used to guide DOT forward problem without the intervention of MRI (see Chapter 5).

## 6.4 Purely optical tomography protocol

In Diffuse Optical Imaging of brain activity a 3D MRI-based subject anatomical model is used to simulate light propagation in highly scattering tissues. However, an

MRI scan is expensive and might not always be available for particular subjects or might not be feasible in certain situations (for example, for claustrophobic subjects). Currently the most successful method of solving the DOT inverse problem is to use subject-specific anatomical information which is derived from an MR anatomical scan.

In Chapter 5 we describe an imaging protocol that uses solely Diffuse Optical Tomography to reconstruct brain activation. The approach consists of using an atlas-based anatomical model instead of the subject's anatomy and simulating photon migration on the atlas model (DOT forward model) while acquiring optical measurements from the subject, and then reconstructing the location of cortical activation (by solving the DOT inverse problem). The benefits of this novel method comes from the elimination of the need for MRI, and its associated issues (such as high costs, possible subject's discomfort and claustrophobia during the MR anatomical scan, prohibiting studies on neonatal subjects, lack of portability).

We first present a preliminary study using one single subject registered to an atlas using MRI-based registration (Section 5.1). We validate our claim that an atlas can be a suitable substitute to the subject specific anatomical model by comparing the simulated optical measurements obtained using the subject specific anatomical model versus the generic adult human head model. The most relevant measurement, the partial pathlength within the brain, indicates that such anatomical approximation can be used without introducing a significant error (relative error $\leq 10\%$), provided that a suitable atlas is selected.

The preliminary study is limited by the size of the dataset (one subject and one atlas) and by the use of a registration algorithm that still needs MR anatomical information. The natural development of the idea of using a general anatomical model in place of the subject specific is described in Section 5.2. Using a dataset of 31 healthy human subjects, we measure sensitivity to absorption changes (solution of the forward model) on a chosen set of 24 functional Region Of Interests (ROIs) and compare the results obtained using the registered atlas versus these calculated using the true subject's anatomical model on a dataset of 31 healthy subjects. The new registration algorithm, based on superficial landmarks, is described in Chapter 4. The registered atlas' CSF thickness is modified according to the subject's age the atlas is registered to, following up the study of Chapter 2. Moreover, we solve DOT forward and inverse problem on three experimental subjects: optical measurements are acquired on the physical subjects and photon migration is simulated on both the subjects' heads and on the atlases registered to the experimental subjects using $SLR_{10\text{-}20}$; the inverse problem is solved using the subject's data and the reconstructed activation map is compared to that calculated guiding DOT forward model with the registered atlas: the qualitative results (see Figures 5-19 and 5-20) show that the activation focus is localized in the correct gyri using the atlas model, although the subject and atlas cortical geometry is not exactly the same and the activation level of contrast is different. Overall, we demonstrate that is possible to use a general anatomical model to represent a subject's to guide DOT forward model to localize

the macroanatomical structure of activation.

## 6.5 Future work

Possible directions of future work include:

1. Study the effect of CSF effective scattering coefficient and CSF thickness on the reconstruction of vascular activity (i.e. DOT inverse problem)

2. Investigate further the variability across population of macroanatomical structures/ROIs localization by transfering them into standard space (for example in MNI space) and then analyze region/areas overlap

3. Extend the purely optical tomography validation with simulated group statistics by re-creating the effect of a chosen pathology on reconstructed vascular activity and test whether an atlas-based reconstruction will enable to distinguish between the controls group and patients group as accurately as when using the subject-specific anatomy

4. Increase the experimental dataset to test our proposed purely optical imaging protocol

5. Improve the purely optical tomography protocol by using an average atlas instead of a single subject reference head model

6. Extend the purely optical tomography validation by testing the localization accuracy of atlas-based reconstruction of simulated vascular activity in a set of functional cortical regions with specifically designed probes

# Appendix A

# Glossary

**10-20 system:**

**AC:** Anterior Commissure (give ref to def)

**anagraphical:** information related to personal data such as one's age and gender

**atlas:** general reference head model

**BA:** Brodmann Area

**BOLD:** Blood Oxygen Level Dependent

**CBF:** Cerebral Blood Flow

**CBV:** Cerebral Blood Volume

**$CMRO_2$:** Cerebral Metabolic Rate of Oxygen

**CNR:** Contrast to Noise Ratio

**CSF:** Cerebral Spinal Fluid

**CW:** Continuous Wave (see Equation 2.1 for the mathematical definition)

**DA:** Diffusion Approximation (see Equation 1.14)

**DOI:** Diffuse Optical Imaging, a more general term indicating 2D and 3D optical imaging techniques

**DOT:** Diffuse Optical Tomography: a 3D (hence tomographic) imaging of the vascular response to brain activity

**EEG:** Electroencephalography

**$\Phi$:** light intensity symbol (see intensity definition)

**FD:** Finite Difference

**fluence:** number of photons per unit volume

**fluence rate:** see intensity

**fMRI:** functional Magnetic Resonance Imaging

**FWHM:** Full Width at Half Maximum

**HbO:** Oxy-hemoglobin

**HbR:** Deoxy-hemoglobin

**HbT:** Total hemoglobin

**HDR:** HemoDynamic Response (see hemodynamics)

**hemodynamics:** refers to changes in blood flow and blood oxygenation and is coupled with neural activity

**intensity:** $\Phi(\mathbf{r},t) = \int_{4\pi} R(\mathbf{r},\hat{s},t)d\Omega$, where $R(\mathbf{r},\hat{s},t)$ is the radiance

**normalization:** in the context of registration, means registering an anatomical model to standard space

**MC:** Monte Carlo (used to simulate photon migration in highly scattering biological tissues)

**MEG:** Magnetoencephalography

**MRI:** Magnetic Resonance Imaging (or just MR)

$\mu_a$**:** absorption coefficient: the inverse of the photon mean free path for absorption

$\mu_s$**:** scattering coefficient: the inverse of the photon mean free path for scattering

**NIRS:** Near Infra Red Spectroscopy

**optodes:** a bundle of fibers optic designed to inject or receive near infrared light

**PPF:** Partial Path length Factor is the PPL normalized by the source-detector separation $d$: PPL/$d$

**PPL:** Partial Path Length (see Section 1.1.3, Equation 1.21 for mathematical definition)

**probe:** a set of optodes geometrically distributed on a head surface

**radiance:** $R(\mathbf{r},\hat{s},t)$ (see Section 1.1.2.1)

**registration:** map of an object from its native space into the chosen target space

**ROI:** Region Of Interest

**RTE:** Radiative Transfer Equation (see Equation 1.8)

**SNR:** Signal to Noise Ratio

**$SO_2$:** level of Oxygen Saturation

**TD:** Time Domain (see Equation 1.19 for the mathematical definition)

# Appendix B

# Additional tables

We report here the exhaustive tables describing variability of Partial Path Length (Table B.1) and of anatomical features (Table B.3) across subjects in relation to the location of scalp-landmarks. The variability in PPL is mostly due to the population alignment variability of scalp landmarks-anatomical structures (sulci and gyra) the Brodmann areas are defined by [42, 35], in agreement with other recent publications [5, 42].

## B.1 Partial Path Length variability

Population variability of optical path length in a functional area is mostly due to the different alignment of cortical structures (sulci and gyra) with respect to scalp-landmarks in each subject. We analyzed our database of 31 healthy subjects and measured the PPL on each of our selected 24 functional regions and compiled Table B.1 with these findings. The first column of the table identifies the subject by number followed by an "R" or an "L" for right or left hemisphere respectively. The remaining eleven columns refer to 11 of the 12 regions of interest we investigated (region MT has been omitted because of lack of signal). The data filling the table are the PPL in millimeters as measured by the highest contributer mini probe (see Equation 5.7), and the 10-20 point center of such mini probe is specified in the table.

Table B.1: Variability of PPL in functional ROIs across population [mm]

| Sbj | 1 | 2 | 3a | 3b | 4a | 4p | 6 | 44 | 45 | V1 | V2 |
|---|---|---|---|---|---|---|---|---|---|---|---|
| 1R | 3.54 C4 | 2.35 C4 | 0.01 C4 | 0.73 C4 | 0.65 C4 | 0.09 C4 | 3.78 C4 | 0.04 F8 | 0.42 F8 | 0.28 O2 | 2.49 O2 |
| 1L | 1.14 C3 | 1.92 C3 | 0.01 C3 | 0.94 C3 | 1.34 C3 | 0.38 C3 | 3.80 C3 | 0.02 C3 | 0.05 F7 | 1.18 Oz | 5.44 O1 |
| 2R | 3.77 C4 | 1.66 C4 | 0.04 C4 | 1.18 C4 | 0.23 C4 | 0.09 C4 | 3.13 C4 | 0.06 F8 | 1.07 F8 | 1.63 O2 | 5.97 O2 |
| 2L | 1.61 C3 | 0.93 C3 | 0.03 C3 | 1.08 C3 | 0.52 C3 | 0.10 C3 | 5.04 C3 | 0.01 F7 | 1.09 F7 | 1.58 Oz | 7.19 O1 |
| 3R | 2.66 C4 | 1.85 C4 | 0.05 C4 | 0.05 C4 | 0.24 C4 | 0.12 C4 | 2.77 C4 | 0.01 F8 | 0.01 F8 | 1.41 O2 | 9.55 O2 |
| 3L | 2.77 C3 | 1.74 C3 | 0.06 C3 | 1.60 C3 | 0.42 C3 | 0.61 C3 | 3.54 C3 | 0.02 C3 | 0.00 F7 | 1.54 Oz | 13.64 O1 |
| 4R | 4.04 C4 | 1.49 C4 | 0.03 C4 | 0.69 C4 | 0.23 C4 | 0.11 C4 | 1.47 C4 | 0.29 F8 | 7.60 F8 | 2.17 O2 | 9.02 O2 |
| 4L | 4.59 C3 | 3.54 C3 | 0.02 C3 | 2.02 C3 | 0.56 C3 | 0.10 C3 | 1.20 C3 | 0.12 F7 | 2.42 F7 | 3.31 Oz | 5.43 O1 |
| 5R | 3.38 C4 | 2.73 C4 | 0.08 C4 | 1.69 C4 | 0.38 C4 | 0.14 C4 | 6.86 C4 | 0.03 F8 | 1.04 F8 | 4.40 O2 | 7.56 O2 |
| 5L | 5.21 C3 | 2.52 C3 | 0.06 C3 | 2.21 C3 | 1.26 C3 | 0.29 C3 | 11.35 C3 | 0.05 T3 | 0.36 F7 | 5.04 O1 | 8.08 O1 |
| 6R | 3.34 C4 | 1.62 C4 | 0.04 C4 | 0.00 C4 | 0.00 Fz | 0.13 C4 | 2.24 C4 | 0.08 F8 | 0.00 Fz | 1.26 O2 | 4.81 O2 |
| 6L | 1.48 C3 | 1.04 C3 | 0.02 C3 | 0.95 C3 | 0.02 C3 | 0.21 C3 | 3.00 C3 | 0.00 F7 | 0.19 F7 | 0.00 Oz | 1.89 Oz |
| 7R | 2.51 C4 | 1.07 C4 | 0.00 C4 | 0.22 C4 | 0.18 C4 | 0.04 C4 | 2.46 C4 | 0.09 F8 | 1.92 F8 | 4.08 O2 | 3.12 O2 |
| 7L | 3.71 C3 | 1.67 C3 | 0.00 C3 | 0.48 C3 | 0.11 C3 | 0.01 C3 | 2.06 C3 | 0.01 C3 | 0.12 F7 | 10.07 O1 | 2.10 O1 |
| 8R | 2.61 C4 | 1.13 C4 | 0.04 C4 | 0.69 C4 | 0.16 C4 | 0.06 C4 | 0.98 C4 | 0.18 F8 | 10.40 F8 | 2.07 O2 | 10.16 O2 |
| 8L | 3.55 C3 | 2.02 C3 | 0.04 C3 | 1.35 C3 | 0.26 C3 | 0.08 C3 | 0.57 C3 | 0.10 F7 | 1.72 F7 | 3.84 Oz | 10.97 O1 |
| 9R | 2.11 C4 | 0.69 C4 | 0.02 C4 | 0.39 C4 | 0.24 C4 | 0.06 C4 | 2.44 C4 | 0.00 T4 | 0.02 F8 | 0.04 Oz | 0.63 O2 |
| 9L | 2.61 C3 | 1.19 C3 | 0.01 C3 | 1.23 C3 | 0.29 C3 | 0.03 C3 | 1.47 C3 | 0.00 C3 | 0.00 F7 | 0.22 O1 | 1.28 O1 |
| 10R | 0.60 C4 | 0.30 C4 | 0.00 C4 | 0.14 C4 | 0.03 C4 | 0.01 C4 | 0.91 C4 | 0.01 F8 | 0.20 F8 | 1.88 Oz | 4.01 O2 |
| 10L | 1.48 C3 | 0.89 C3 | 0.00 C3 | 0.43 C3 | 0.13 C3 | 0.01 C3 | 1.03 C3 | 0.01 F7 | 0.11 F7 | 4.11 Oz | 5.72 O1 |
| 11R | 3.45 C4 | 1.26 C4 | 0.01 C4 | 0.54 C4 | 0.42 C4 | 0.13 C4 | 0.74 C4 | 0.28 F8 | 1.58 F8 | 6.31 O2 | 15.83 O2 |
| 11L | 3.01 C3 | 0.93 C3 | 0.02 C3 | 1.62 C3 | 1.40 C3 | 0.17 C3 | 4.83 C3 | 0.04 F7 | 0.47 F7 | 3.15 Oz | 9.95 Oz |
| 12R | 2.62 C4 | 3.48 C4 | 0.01 C4 | 1.48 C4 | 0.07 C4 | 0.03 C4 | 0.96 C4 | 0.14 F8 | 1.54 F8 | 11.89 O2 | 14.57 O2 |
| 12L | 6.13 C3 | 4.53 C3 | 0.01 C3 | 1.81 C3 | 0.11 C3 | 0.02 C3 | 0.97 C3 | 0.01 F7 | 0.73 F7 | 12.49 Oz | 21.02 O1 |
| 14R | 1.40 C4 | 0.48 C4 | 0.00 C4 | 0.08 C4 | 0.05 C4 | 0.01 C4 | 0.17 C4 | 0.04 F8 | 0.95 F8 | 1.80 O2 | 5.05 O2 |
| 14L | 0.82 C3 | 0.67 C3 | 0.00 C3 | 0.08 C3 | 0.02 C3 | 0.00 C3 | 0.04 C3 | 0.00 F7 | 0.19 F7 | 5.10 O1 | 3.12 O1 |
| 15R | 3.84 C4 | 2.98 C4 | 0.08 C4 | 0.84 C4 | 0.42 C4 | 0.28 C4 | 1.45 C4 | 0.09 F8 | 2.72 F8 | 7.99 O2 | 7.52 O2 |
| 15L | 3.45 C3 | 3.07 C3 | 0.02 C3 | 0.79 C3 | 0.38 C3 | 0.07 C3 | 0.39 C3 | 0.44 F7 | 0.53 F7 | 8.87 O1 | 7.95 O1 |
| 16R | 2.49 C4 | 0.90 C4 | 0.05 C4 | 0.85 C4 | 0.30 C4 | 0.14 C4 | 2.19 C4 | 0.07 F8 | 1.83 F8 | 0.06 O2 | 0.31 O2 |
| 16L | 1.27 C3 | 1.21 C3 | 0.02 C3 | 0.73 C3 | 0.28 C3 | 0.09 C3 | 2.11 C3 | 0.01 T3 | 0.32 F7 | 0.22 Oz | 0.62 Oz |
| 17R | 3.82 C4 | 1.26 C4 | 0.00 C4 | 0.84 C4 | 0.14 C4 | 0.02 C4 | 1.70 C4 | 0.00 F8 | 0.11 F8 | 0.48 O2 | 5.44 O2 |
| 17L | 1.45 C3 | 0.54 C3 | 0.00 C3 | 0.77 C3 | 0.30 C3 | 0.03 C3 | 3.68 C3 | 0.00 T3 | 0.02 F7 | 11.67 Oz | 16.40 Oz |
| 18R | 1.43 C4 | 1.44 C4 | 0.01 C4 | 0.19 C4 | 0.04 C4 | 0.02 C4 | 0.20 C4 | 0.49 F8 | 5.58 F8 | 3.79 Oz | 9.85 O2 |
| 18L | 3.21 C3 | 1.89 C3 | 0.01 C3 | 1.01 C3 | 0.19 C3 | 0.04 C3 | 0.69 C3 | 0.09 F7 | 1.52 F7 | 3.40 Oz | 8.06 O1 |
| 19R | 0.23 C4 | 0.19 C4 | 0.00 C4 | 0.04 C4 | 0.02 C4 | 0.00 C4 | 0.08 C4 | 0.09 F8 | 0.91 F8 | 0.66 O2 | 3.34 O2 |
| 19L | 0.47 C3 | 0.40 C3 | 0.00 C3 | 0.06 C3 | 0.06 C3 | 0.02 C3 | 0.17 C3 | 0.10 F7 | 0.57 F7 | 0.41 Oz | 2.87 O1 |
| 20R | 6.54 C4 | 2.51 C4 | 0.06 C4 | 1.24 C4 | 0.64 C4 | 0.21 C4 | 1.99 C4 | 0.48 F8 | 7.64 F8 | 1.41 O2 | 9.11 O2 |
| 20L | 5.93 C3 | 2.61 C3 | 0.03 C3 | 1.27 C3 | 0.45 C3 | 0.09 C3 | 2.86 C3 | 0.19 F7 | 2.79 F7 | 0.93 Oz | 6.87 Oz |
| 21R | 5.65 C4 | 1.33 C4 | 0.02 C4 | 0.89 C4 | 0.31 C4 | 0.08 C4 | 2.57 C4 | 0.05 F8 | 0.47 F8 | 0.44 O2 | 1.92 O2 |
| 21L | 0.38 C3 | 0.30 C3 | 0.01 C3 | 0.46 C3 | 0.54 C3 | 0.12 C3 | 4.49 C3 | 0.02 C3 | 0.04 F7 | 0.28 Oz | 1.54 Oz |
| 22R | 1.23 C4 | 1.58 C4 | 0.00 C4 | 0.26 C4 | 0.04 C4 | 0.01 C4 | 0.14 C4 | 0.01 F8 | 1.20 F8 | 4.11 O2 | 7.07 O2 |
| 22L | 2.72 C3 | 2.14 C3 | 0.00 C3 | 0.56 C3 | 0.19 C3 | 0.03 C3 | 1.01 C3 | 0.00 F7 | 0.15 F7 | 6.88 Oz | 6.26 Oz |
| 23R | 0.43 C4 | 0.17 C4 | 0.00 C4 | 0.35 C4 | 0.22 C4 | 0.04 C4 | 5.61 C4 | 0.01 T4 | 0.21 F8 | 1.06 O2 | 4.89 O2 |
| 23L | 1.22 C3 | 0.16 C3 | 0.00 C3 | 1.00 C3 | 0.28 C3 | 0.06 C3 | 4.33 C3 | 0.01 T3 | 0.27 F7 | 1.32 Oz | 4.17 O1 |
| 24R | 3.34 C4 | 1.21 C4 | 0.01 C4 | 0.44 C4 | 0.22 C4 | 0.07 C4 | 0.62 C4 | 0.17 F8 | 4.52 F8 | 5.08 O2 | 9.19 O2 |
| 24L | 6.98 C3 | 2.12 C3 | 0.01 C3 | 1.80 C3 | 0.47 C3 | 0.07 C3 | 1.36 C3 | 0.06 F7 | 1.92 F7 | 9.57 Oz | 6.10 O1 |
| 25R | 5.07 C4 | 1.64 C4 | 0.01 C4 | 0.66 C4 | 0.26 C4 | 0.09 C4 | 3.35 C4 | 0.03 F8 | 1.10 F8 | 3.74 O2 | 2.47 O2 |
| 25L | 5.47 C3 | 2.05 C3 | 0.02 C3 | 1.81 C3 | 0.76 C3 | 0.08 C3 | 5.85 C3 | 0.03 F7 | 0.98 F7 | 4.67 Oz | 3.94 Oz |
| 26R | 6.03 C4 | 4.56 C4 | 0.07 C4 | 1.13 C4 | 0.48 C4 | 0.01 C4 | 2.26 C4 | 0.26 F8 | 6.10 F8 | 5.43 O2 | 11.07 O2 |
| 26L | 7.04 C3 | 1.35 C3 | 0.03 C3 | 2.12 C3 | 0.69 C3 | 0.17 C3 | 4.12 C3 | 0.19 F7 | 3.34 F7 | 0.71 Oz | 23.92 Oz |
| 27R | 4.31 C4 | 2.44 C4 | 0.04 C4 | 0.79 C4 | 0.42 C4 | 0.14 C4 | 2.28 C4 | 0.18 F8 | 4.03 F8 | 2.21 O2 | 9.26 O2 |
| 27L | 2.66 C3 | 2.34 C3 | 0.03 C3 | 1.23 C3 | 0.41 C3 | 0.08 C3 | 1.65 C3 | 0.02 F7 | 0.18 F7 | 1.40 Oz | 6.40 Oz |

Table B.2: Table B.1 – continuation

| Sbj | 1 | 2 | 3a | 3b | 4a | 4p | 6 | 44 | 45 | V1 | V2 |
|---|---|---|---|---|---|---|---|---|---|---|---|
| 28R | 6.44 C4 | 2.44 C4 | 0.02 C4 | 1.07 C4 | 1.00 C4 | 0.18 C4 | 4.41 C4 | 0.07 F8 | 2.79 F8 | 2.47 O2 | 10.56 O2 |
| 28L | 3.25 C3 | 2.67 C3 | 0.01 C3 | 1.04 C3 | 1.14 C3 | 0.08 C3 | 3.88 C3 | 0.03 F7 | 1.56 F7 | 3.95 O1 | 16.46 O1 |
| 29R | 5.59 C4 | 3.31 C4 | 0.03 C4 | 1.07 C4 | 0.96 C4 | 0.24 C4 | 4.70 C4 | 0.39 F8 | 11.57 F8 | 2.70 O2 | 10.45 O2 |
| 29L | 5.69 C3 | 4.04 C3 | 0.04 C3 | 1.49 C3 | 1.16 C3 | 0.23 C3 | 3.12 C3 | 0.40 F7 | 3.36 F7 | 3.54 O1 | 6.22 O1 |
| 30R | 6.29 C4 | 5.14 C4 | 0.32 C4 | 2.65 C4 | 0.14 C4 | 0.84 C4 | 1.33 C4 | 2.47 F8 | 9.26 F8 | 4.53 Oz | 8.84 O2 |
| 30L | 8.02 C3 | 7.52 C3 | 0.22 C3 | 2.78 C3 | 0.26 C3 | 0.18 C3 | 0.58 C3 | 0.71 F7 | 1.61 F7 | 2.94 O1 | 13.44 O1 |
| 31R | 3.50 C4 | 0.68 C4 | 0.02 T4 | 0.58 C4 | 0.89 C4 | 0.21 C4 | 4.46 C4 | 0.14 F8 | 7.46 F8 | 2.50 Oz | 1.91 Oz |
| 31L | 2.75 C3 | 1.31 C3 | 0.01 C3 | 0.49 C3 | 0.50 C3 | 0.11 C3 | 2.20 C3 | 0.10 F7 | 3.84 F7 | 2.61 O1 | 4.80 O1 |
| 32R | 2.12 C4 | 2.30 C4 | 0.01 C4 | 0.36 C4 | 0.09 C4 | 0.03 C4 | 0.36 C4 | 0.14 F8 | 1.52 F8 | 0.99 O2 | 4.21 O2 |
| 32L | 1.96 C3 | 1.05 C3 | 0.01 C3 | 0.50 C3 | 0.25 C3 | 0.04 C3 | 0.97 C3 | 0.02 F7 | 0.17 F7 | 2.22 O1 | 5.97 O1 |

## B.2 Surface-Cortical landmarks alignment: variability across population

Table B.1 variability analysis is complemented by Table B.3, where are listed the anatomical structures underlying each optode position; the data shown in the table are obtained by projecting each optode scalp-location onto the cortex using the algorithm described in Okamoto et al. [100]; the anatomical structures are calculated as described in Desikan et al. [35]; the first and second columns of the table indicate the 10-20 point center of the mini-probe analyzed and its general location (left-hemisphere/right-hemisphere/central sulcus); the third column reports the anatomical structure onto which the four optodes forming the mini-probe project; the last four columns show each mini-probe optode frequency count (which is, the number of subjects (out of the 26 analyzed) for which that optode projects onto the structure specified in the third column). The tables show the variability across the population of the PPL (Table B.1) mostly due to the intrinsic variability of the ROIs locations, which are identified by specific anatomical structures [42, 35] (Table B.3), in agreement with the findings of Amunts et al. [5] and Fischl et al. [42].

Table B.3: List of anatomical regions optodes project onto

| Mini-probe* | hem | anatomical region** | subjects count*** | | | |
|---|---|---|---|---|---|---|
| C3 | left | none | 1 | 4 | 4 | 3 |
| | | caudalmiddlefrontal | | 2 | | |
| | | postcentral | 12 | 8 | 9 | 14 |
| | | precentral | 3 | 12 | 2 | 9 |
| | | supramarginal | 10 | | 11 | |
| C4 | right | none | 4 | 3 | 2 | 2 |
| | | caudalmiddlefrontal | 2 | | | 1 |
| | | postcentral | 8 | 14 | 10 | 14 |
| | | precentral | 12 | 9 | 14 | 9 |
| F7 | left | none | 3 | 2 | 1 | 2 |
| | | caudalmiddlefrontal | | 1 | | |
| | | lateralorbitofrontal | | | | 1 |
| | | paracentral | | | 1 | |
| | | parsorbitalis | | | | 16 |
| | | parstriangularis | | | | 6 |
| | | postcentral | 14 | 14 | | |
| | | precentral | 9 | 9 | 19 | |
| | | superiorfrontal | | | 5 | |
| | | superiortemporal | | | | 1 |
| F8 | right | none | 2 | 2 | 4 | 6 |
| | | lateralorbitofrontal | | | | 1 |
| | | paracentral | | 10 | | |
| | | parsopercularis | | | 1 | |
| | | parsorbitalis | | | 2 | 13 |
| | | parstriangularis | | | 17 | 6 |
| | | postcentral | 11 | | | |
| | | precentral | | 3 | | |
| | | rostralmiddlefrontal | | | 2 | |
| | | superiorfrontal | | 11 | | |
| | | supramarginal | 13 | | | |
| T6 | right | none | 3 | 2 | 2 | 2 |
| | | fusiform | | | | 3 |
| | | inferiortemporal | | | | 12 |
| | | lateraloccipital | | | | 8 |
| | | middletemporal | | | | 1 |
| | | parsorbitalis | 13 | | | |
| | | parstriangularis | 3 | | | |
| | | postcentral | | | 3 | |
| | | precuneus | | | 5 | |
| | | rostralmiddlefrontal | 7 | | | |
| | | superiorfrontal | | 24 | | |
| | | superiorparietal | | | 16 | |

Table B.4: Table B.3 cont.

| Mini-probe* | hem | anatomical region** | subjects | count*** | | |
|---|---|---|---|---|---|---|
| Fp1 | left | none | 2 | 1 | 1 | 3 |
| | | parsopercularis | | 3 | | |
| | | parsorbitalis | | 3 | | |
| | | parstriangularis | | 18 | | |
| | | postcentral | 13 | | | |
| | | rostralmiddlefrontal | | | 4 | 22 |
| | | superiorfrontal | | | 17 | 1 |
| | | superiortemporal | | 1 | | |
| | | supramarginal | 11 | | | |
| | | frontalpole | | | 4 | |
| Fp2 | right | none | 2 | 2 | 4 | 3 |
| | | caudalmiddlefrontal | 1 | | | |
| | | lateralorbitofrontal | | 1 | | |
| | | parsorbitalis | | 16 | | |
| | | parstriangularis | | 6 | | |
| | | postcentral | 14 | | | |
| | | precentral | 9 | | | |
| | | rostralmiddlefrontal | | | 4 | 1 |
| | | superiorfrontal | | | 17 | 13 |
| | | superiortemporal | | 1 | | |
| | | frontalpole | | | 1 | 9 |
| O1 | left | none | 2 | 6 | 3 | 2 |
| | | lateraloccipital | | | | 23 |
| | | lateralorbitofrontal | | 1 | | |
| | | paracentral | 10 | | | |
| | | parsorbitalis | | 13 | | |
| | | parstriangularis | | 6 | | |
| | | pericalcarine | | | | 1 |
| | | precentral | 3 | | | |
| | | rostralmiddlefrontal | | | 13 | |
| | | superiorfrontal | 11 | | 10 | |
| O2 | right | none | 2 | 4 | 4 | 3 |
| | | lateraloccipital | | | | 23 |
| | | paracentral | 1 | | | |
| | | postcentral | 2 | | | |
| | | precentral | 18 | | | |
| | | superiorfrontal | 3 | 21 | 22 | |
| | | frontalpole | | 1 | | |
| T3 | left | none | 4 | 3 | 2 | 2 |
| | | inferiorparietal | | | 24 | |
| | | inferiortemporal | | | | 5 |
| | | middletemporal | | | | 19 |
| | | parsopercularis | 1 | | | |
| | | parsorbitalis | 2 | | | |
| | | parstriangularis | 17 | | | |
| | | rostralmiddlefrontal | 2 | 13 | | |
| | | superiorfrontal | | 10 | | |

Table B.5: Table B.4 cont.

| Mini-probe* | hem | anatomical region** | subjects count*** | | | |
|---|---|---|---|---|---|---|
| P3 | left | none | 1 | 4 | 2 | 2 |
| | | inferiorparietal | | | | 18 |
| | | paracentral | 1 | | | |
| | | precentral | 19 | | | |
| | | rostralmiddlefrontal | | 4 | | |
| | | superiorfrontal | 5 | 17 | 24 | |
| | | superiorparietal | | | | 5 |
| | | supramarginal | | | | 1 |
| | | frontalpole | | 1 | | |
| P4 | right | none | 4 | 3 | | 2 |
| | | inferiorparietal | | | | 16 |
| | | lateraloccipital | | | 26 | |
| | | parsorbitalis | 9 | | | |
| | | parstriangularis | 9 | | | |
| | | rostralmiddlefrontal | 4 | 18 | | |
| | | superiorfrontal | | 5 | | |
| | | superiorparietal | | | | 8 |
| T4 | right | none | 2 | 3 | 2 | 2 |
| | | inferiorparietal | | | 18 | |
| | | inferiortemporal | | | | 7 |
| | | lateralorbitofrontal | 1 | | | |
| | | middletemporal | | | | 16 |
| | | parsorbitalis | 16 | | | |
| | | parstriangularis | 6 | | | |
| | | rostralmiddlefrontal | | 1 | | |
| | | superiorfrontal | | 13 | | |
| | | superiorparietal | | | 5 | |
| | | superiortemporal | 1 | | | 1 |
| | | supramarginal | | | 1 | |
| | | frontalpole | | 9 | | |
| T5 | left | none | 6 | 4 | 3 | 3 |
| | | fusiform | | | | 2 |
| | | inferiorparietal | | | 10 | |
| | | inferiortemporal | | | | 12 |
| | | lateraloccipital | | | | 6 |
| | | middletemporal | | | | 3 |
| | | parsopercularis | 4 | | | |
| | | parsorbitalis | 3 | | | |
| | | parstriangularis | 11 | | | |
| | | rostralmiddlefrontal | 1 | | | |
| | | superiorfrontal | | 22 | | |
| | | superiorparietal | | | 13 | |
| | | superiortemporal | 1 | | | |

Table B.6: Table B.5 cont.

| Mini-probe* | hem | anatomical region** | subjects count*** | | | |
|---|---|---|---|---|---|---|
| Fpz | center | none | 2 | 1 | 3 | 4 |
| | | paracentral | | 1 | | |
| | | parsorbitalis | | | 13 | |
| | | parstriangularis | | | 3 | |
| | | postcentral | 10 | | | |
| | | precentral | 14 | 19 | | |
| | | rostralmiddlefrontal | | | 7 | 4 |
| | | superiorfrontal | | 5 | | 17 |
| | | frontalpole | | | | 1 |
| Cz | center | none | 4 | 2 | 1 | 1 |
| | | paracentral | | | 9 | 1 |
| | | postcentral | 9 | 10 | 7 | |
| | | precentral | 2 | 14 | 8 | 19 |
| | | superiorfrontal | | | 1 | 5 |
| | | supramarginal | 11 | | | |
| Fz | center | none | 1 | 3 | 3 | 2 |
| | | paracentral | 9 | | | |
| | | parsorbitalis | | 13 | | |
| | | parstriangularis | | 3 | | |
| | | postcentral | 7 | | | |
| | | precentral | 8 | | | |
| | | rostralmiddlefrontal | | 7 | 21 | |
| | | superiorfrontal | 1 | | | 24 |
| | | frontalpole | | | 2 | |
| Pz | center | none | 1 | 3 | 5 | 9 |
| | | lateraloccipital | | | 21 | |
| | | parsopercularis | 3 | | | |
| | | parsorbitalis | 3 | | | |
| | | parstriangularis | 18 | | | |
| | | precuneus | | | | 1 |
| | | rostralmiddlefrontal | | 22 | | |
| | | superiorfrontal | | 1 | | |
| | | superiorparietal | | | | 16 |
| | | superiortemporal | 1 | | | |
| Oz | center | none | 2 | 5 | 3 | 4 |
| | | inferiorparietal | | 1 | | |
| | | lateraloccipital | | 18 | | 20 |
| | | middletemporal | | | 7 | |
| | | parsorbitalis | 1 | | | |
| | | parstriangularis | 21 | | | |
| | | pericalcarine | | | | 1 |
| | | precentral | | | 2 | |
| | | rostralmiddlefrontal | 2 | | | |
| | | superiorparietal | | 2 | | 1 |
| | | superiortemporal | | | 14 | |

* 10-20 point center of the mini-probe
** macroanatomical structures identified on FreeSurfer atlas
*** subject count per optode per mini-probe (4 opt. each)

# Bibliography


[1] https://surfer.nmr.mgh.harvard.edu/fswiki.

[2] http://www.bic.mni.mcgill.ca/brainweb.

[3] http://www.fil.ion.ucl.ac.uk/spm.

[4] M. S. Albert. Cognitive and neurobiologic markers of early alzheimer disease. *Proc. Natl. Acad. Sci. USA*, 93:1354713551, 1996.

[5] K. Amunts, A. Malikovic, H. Mohlberg, T. Schormann, and K. Zilles. Brodmann's areas 17 and 18 brought into stereotaxic space-where and how variable? *Neuroimage*, 11(1):66–84, 2000.

[6] B. Ances. Coupling of changes in cerebral blood flow with neural activity: What must initially dip must come back up. *Journal of Cerebral Blood Flow & Metabolism*, 24(1):1–6, 2004.

[7] L. M. Angelone, S. Tulloch, and et al. New high resolution head model for accurate electromagnetic field computation. In *International Society of Magn. Reson. Med.*, Miami, FL, USA, 2005.

[8] S. Arridge. Photon-measurement density functions. part i: Analytical forms. *Appl. Opt.*, 34:7395–7409, 1995.

[9] S. Arridge. Optical tomography in medical imaging. *Inverse Problems*, 15(2):41 – 93, 1999.

[10] S. Arridge, M. Schweiger, M. Hiraoka, and D. Delpy. A finite element approach for modeling photon transport in tissue. *Medical Physics*, 20:299 – 309, 1993.

[11] S. R. Arridge, H. Dehghani, M. Schweiger, and E. Okada. The finite element model for the propagation of light in scattering media: a direct method for domains with nonscattering regions. *Med Phys*, 27(1):252–64, 2000.

[12] R. Barbour, H. Graber, J. Chang, S. Barbour, P. Koo, and R. Aronson. Mri-guided optical tomography:prospects and computation for a new imaging method. *IEEE Computation Science and Engineering*, 2:63–77, 1995.

[13] A. H. Barnett, J. Culver, A. Sorensen, A. Dale, and D. Boas. Robust inference of baseline optical properties of the human head with 3d segmentation from magnetic resonance imaging. *Applied Optics*, 42:3095–3108, 2003.

[14] M. Bertero and P. Boccacci. *Introduction to Inverse Problems in Imaging.* IOP Publishing, 1998.

[15] D. Boas, D. Brooks, E. Miller, C. DiMarzio, M. Kilmer, R. Gaudette, and Q. Zhang. Imaging the body with diffuse optical tomography. *IEEE Signal Processing Magazine*, 18(6):57 – 75, 2001.

[16] D. Boas, J. Culver, J. Stott, and A. Dunn. Three dimensional monte carlo code for photon migration through complex heterogeneous media including the adult human head. *Optics Express*, 10(3):159 – 170, 2002.

[17] D. Boas, A. Dale, and M. Franceschini. Diffuse optical imaging of brain activation: approaches to optimizing image sensitivity, resolution and accuracy. *Neuroimage*, 23(1):S275–88, 2004.

[18] D. Boas, G. Strangman, J. Culver, R. Hoge, G. Jasdzewski, R. Poldrack, B. Rosen, and J. Mandeville. Can the cerebral metabolic rate of oxygen be estimated with near-infrared spectroscopy? *Physics in Medicine and Biology*, 48(15):2405 – 18, 2003.

[19] D. A. Boas and D. anders M. Simulation study of magnetic resonance imaging-guided cortically constrained diffuse optical tomography of human brain function. *Applied Optics*, 44(10):1957–1968, 2005.

[20] B. Boeve, D. Maraganore, J. Parisi, J. Ahlskog, N. Graff-Radford, R. Caselli, D. Dickson, E. Kokmen, and R. Peterson. Pathologic heterogeneity in clinically diagnosed corticobasal degeneration. *Neurology*, 53(4):795800, 1999.

[21] R. Born and D. Bradley. Structure and function of visual area mt. *Annu Rev Neurosci*, 28:157–89, 2005.

[22] K. Brodmann. *Brodmann's 'Localisation in the Cerebral Cortex'.* Smith-Gordon, London, UK, 1909/1994.

[23] V. Chernomordik, D. Hattery, D. Grosenick, H. Wabnitz, H. Rinneberg, K. Moesta, P. Schlag, and A. Gandjbakhche. Quantification of optical properties of a breast tumor using random walk theory. *Journal of Biomedical Optics*, 7(1):80–7, 2002.

[24] R. Choe, A. Corlu, K. Lee, T. Durduran, S. D. Konecky, M. Grosicka-Koptyra, S. R. Arridge, B. J. Czerniecki, D. L. Fraker, A. DeMichele, B. Chance, M. A. Rosen, and A. G. Yodh. Diffuse optical tomography of breast cancer during neoadjuvant chemotherapy: a case study with comparison to mri. *Med Phys*, 32(4):1128–39, 2005.

[25] D. L. Collins, A. P. Zijdenbos, V. Kollokian, J. Sled, N. Kabani, C. Holmes, and A. Evans. Design and construction of a realistic digital brain phantom. *IEEE transactions on medical imaging*, 17(3), 1998.

[26] R. C.S. and C. Sherrington. On the regulation of the blood-supply of the brain. *J Physiol.*, 11:85–158, 1890.

[27] A. Custo, W. Wells III, A. Barnett, E. Hillman, and D. Boas. Effective scattering coefficient of the cerebral spinal fluid in adult head models for diffuse optical imaging. *Appl. Opt.*, 45(19):4747–4755, 2006.

[28] A. Custo and W. M. Wells III. Combined optical and magnetic functional brain imaging. In *Organization for Human Brain Mapping*, Florence, Italy, June 2006. Organization for Human Brain Mapping.

[29] A. Custo and W. M. Wells III. Effect of csf thickness in diffuse optical imaging. In *Organization for Human Brain Mapping*, Chicago, IL, USA, June 2007. Organization for Human Brain Mapping.

[30] F. Darvas, J. Ermer, J. Mosher, and R. Leahy. Generic head models for atlas-based eeg source analysis. *Hum Brain Mapp.*, 27(2):129–43, 2006.

[31] M. J. De Leon, A. E. George, J. Golomb, C. Tarshish, A. Convit, A. Kluger, S. De Santi, T. McRae, S. H. Ferris, B. Reisberg, C. Ince, H. Rusinek, M. Bobinski, B. Quinn, D. Miller, and H. Wisniewski. Frequency of hippocampal formation atrophy in normal aging and alzheimer's disease. *Neurobiol. Aging*, 18(1):111, 1997.

[32] H. Dehghani, S. R. Arridge, M. Schweiger, and D. T. Delpy. Optical tomography in the presence of void regions. *J Opt Soc Am A Opt Image Sci Vis*, 17(9):1659–70, 2000.

[33] H. Dehghani and D. T. Delpy. Near-infrared spectroscopy of the adult head: Effect of scattering and absorbing obstructions in the cerebrospinal fluid layer on light distribution in the tissue. *Applied Optics*, 39(25):4721–4729, 2000.

[34] H. Dehghani, D. T. Delpy, and S. R. Arridge. Photon migration in non-scattering tissue and the effects on image reconstruction. *Phys Med Biol*, 44(12):2897–906, 1999.

[35] R. Desikan, F. Sgonne, B. Fischl, B. Quinn, B. Dickerson, D. Blacker, R. Buckner, A. Dale, R. Maguire, B. Hyman, M. Albert, and R. Killiany. An automated labeling system for subdividing the human cerebral cortex on mri scans into gyral based regions of interest. *Neuroimage*, 31(3):968–80, 2006.

[36] A. Devor, A. Dunn, M. Andermann, I. Ulbert, D. Boas, and A. Dale. Coupling of total hemoglobin concentration, oxygenation, and neural activity in rat somatosensory cortex. *Neuron*, 39(2):353–359, 2003.

[37] K. L. Double, G. M. Halliday, J. J. Kril, J. A. Harasty, K. Cullen, W. S. Brooks, H. Creasey, and G. A. Broe. Topography of brain atrophy during normal aging and alzheimer's disease. *Neurobiol. Aging*, 17(4):513521, 1996.

[38] A. Duncan, J. Meek, M. Clemence, C. Elwell, L. Tyszczuk, M. Cope, and D. Delpy. Optical pathlength measurements on adult head, calf and forearm and the head of the newborn infant using phase resolved optical spectroscopy. *Phys Med Biol.*, 40(2), 1995.

[39] M. Firbank, S. Arridge, M. Schweiger, and D. Delpy. An investigation of light transport through scattering bodies with non-scattering regions. *Physics in Medicine and Biology*, 41(4):767 – 83, 1996.

[40] B. Fischl and A. Dale. Measuring the thickness of the human cerebral cortex from magnetic resonance images. *Proceedings of the National Academy of Sciences*, 97:11044–11049, 2000.

[41] B. Fischl, A. Liu, and A. Dale. Automated manifold surgery: Constructing geometrically accurate and topologically correct models of the human cerebral cortex. *IEEE Transactions on Medical Imaging*, 20(1):70–80, 2001.

[42] B. Fischl, N. Rajendran, E. Busa, J. Augustinack, O. Hinds, B. Yeo, H. Mohlberg, K. Amunts, and K. Zilles. Cortical folding patterns and predicting cytoarchitecture. *Cerebral Cortex*, In press, 2007.

[43] B. Fischl, D. Salat, E. Busa, M. Albert, M. Dieterich, C. Haselgrove, A. van der Kouwe, R. Killiany, D. Kennedy, S. Klaveness, A. Montillo, N. Makris, B. Rosen, and A. Dale. Whole brain segmentation: automated labeling of neuroanatomical structures in the human brain. *Neuron.*, 33(3):341–55, 2002.

[44] B. Fischl, D. Salat, A. van der Kouwe, N. Makris, F. Sgonne, and A. Dale. Sequence-independent segmentation of magnetic resonance images. *NeuroImage*, 23:S69–S84, 2004.

[45] B. Fischl, M. Sereno, and A. M. Dale. Cortical surface-based analysis ii: Inflation, flattening, and surface-based coordinate system. *NeuroImage*, 9:195–207, 1999.

[46] B. Fischl, M. Sereno, R. Tootell, and A. Dale. High-resolution inter-subject averaging and a coordinate system for the cortical surface. *Human Brain Mapping*, 8:272–284, 1999.

[47] B. Fischl, A. van der Kouwe, C. Destrieux, E. Halgren, F. Segonne, D. Salat, E. Busa, L. Seidman, J. Goldstein, D. Kennedy, V. Caviness, N. Makris, B. Rosen, and A. Dale. Automatically parcellating the human cerebral cortex. *Cerebral Cortex*, 14:11–22, 2004.

[48] M. Franceschini, K. Moesta, S. Fantini, G. Gaida, E. Gratton, H. Jess, W. Mantulin, M. Seeber, P. Schlag, and M. Kaschke. Frequency-domain techniques enhance optical mammography: initial clinical results. *Proc.Natl.Acad.Sci.*, 94:6468–6473, 1997.

[49] M. A. Franceschini, S. Fantini, J. H. Thompson, J. P. Culver, and D. A. Boas. Hemodynamic evoked response of the sensorimotor cortex measured non-invasively with near infrared optical imaging. *Psychophysiology*, 40:548–560, 2003.

[50] G. B. Frisoni, A. Beltramello, C. Weiss, C. Geroldi, A. Bianchetti, and M. Trabucchi. Linear measures of atrophy in mild alzheimer disease. *Am. J. Neuroradiol.*, 17:913923, 1996.

[51] K. Friston. Statistical parametric mapping, 1994.

[52] K. Friston, O. Josephs, G. Rees, and R. Turner. Nonlinear event-related responses in fmri. *Magn Reson Med.*, 39(1):41–52, 1998.

[53] M. Fuchs, J. Kastner, M. Wagner, S. Hawes, and J. Ebersole. A standardized boundary element method volume conductor model. *Clin Neurophysiol.*, 113:702712, 2002.

[54] Y. Fukui, Y. Ajichi, and E. Okada. Monte carlo prediction of near-infrared light propagation in realistic adult and neonatal head models. *Applied Optics*, 42(16):2881 – 7, 2003.

[55] E. Gratton, V. Toronov, U. Wolf, M. Wolf, and A. Webb. Measurement of brain activity by near-infrared light. *J Biomed Opt*, 10(1):11008, 2005.

[56] G. Gratton and M. Fabiani. Shedding light on brain function: the event-related optical signal. *Trends in Cognitive Sciences*, 5(8):357–363, 2001.

[57] H. Gray. *Anatomy of the Human Body.* Lea & Febiger, Philadelphia, 1918.

[58] Y. Grignon, C. Duyckaerts, C. Bennecib, and J. J. Hauw. Cytoarchitectonic alterations in the supramarginal gyrus of late onset alzheimer's disease. *Acta. Neuropathol.*, 95(4):395406, 1998.

[59] D. Grosenick, H. Wabnitz, K. T. Moesta, J. Mucke, M. Moller, C. Stroszczynski, J. Stossel, B. Wassermann, P. M. Schlag, and H. Rinneberg. Concentration and oxygen saturation of haemoglobin of 50 breast tumours determined by time-domain optical mammography. *Phys Med Biol*, 49(7):1165–81, 2004.

[60] R. J. Grubb, M. Raichle, J. Eichling, and M. Ter-Pogossian. The effects of changes in paco2 on cerebral blood volume, blood flow, and vascular mean transit time. *Stroke*, 5:630–9, 1974.

[61] G. M. Halliday, D. A. McRitchie, V. Macdonald, K. L. Double, R. J. Trent, and E. McCusker. Regional specificity of brain atrophy in huntington's disease. *Exp. Neurol.*, 154(2):663672, 1998.

[62] T. Hayashi, Y. Kashio, and E. Okada. Hybrid monte carlo-diffusion method for light propagation in tissue with a low-scattering region. *Applied Optics*, 42(16):2888 – 96, 2003.

[63] A. Hielscher, R. E. Alcouffe, and R. L. Barbour. Comparison of finite-difference transport and diffusion calculations for photon migration in homogeneous and heterogeneous tissues. *Physics in Medicine and Biology*, 43(5):1285 – 1302, 1998.

[64] A. Hielscher, S. Jacques, L. Wang, and F. Tittel. The influence of boundary conditions on the accuracy of diffusion theory in time-resolved reflectance spectroscopy of biological tissues. *Physics in Medicine and Biology*, 40(11):1957 – 75, 1995.

[65] E. Hillman. *Experimental and theoretical investigations of near infrared tomographic imaging methods and clinical applications.* PhD thesis, University College London, 2002.

[66] C. Holmes, R. Hoge, D. L. Collins, R. Woods, A. Toga, and A. Evans. Enhancement of mr images using registration for signal averaging. *Journal of Computer Assisted Tomography*, 22:324 – 333, 1998.

[67] B. Horwitz, K. Amunts, R. Bhattacharyya, D. Patkin, K. Jeffries, K. Zilles, and A. Braun. Activation of broca's area during the production of spoken and signed language: a combined cytoarchitectonic mapping and pet analysis. *Neuropsychologia*, 41(14):1868–76, 2003.

[68] Y. Hoshi and M. Tamura. Detection of dynamic changes in cerebral oxygenation coupled to neuronal function during mental work in man. *Neuroscience Letters*, 150:5–8, 1993.

[69] Y. Hoshi and M. Tamura. Fluctuations in the cerebral oxygenation state during the resting period in functional mapping studies of the human brain. *Med. Biol. Eng. Comput. (UK)*, 35(4):328 – 30, 1997.

[70] T. J. Huppert, R. D. Hoge, A. M. Dale, M. A. Franceschini, and D. A. Boas. Quantitative spatial comparison of diffuse optical imaging with blood oxygen level-dependent and arterial spin labeling-based functional magnetic resonance imaging. *Journal Biomed Optics*, 11(6), 2006.

[71] F. Hyder, R. Shulman, and D. Rothman. A model for the regulation of cerebral oxygen delivery. *J Appl Physiol*, 85:554–64, 1998.

[72] X. Intes, J. Ripoll, Y. Chen, S. Nioka, A. G. Yodh, and B. Chance. In vivo continuous-wave optical breast imaging enhanced with indocyanine green. *Med Phys*, 30(6):1039–47, 2003.

[73] J. Jack, C. R., R. C. Petersen, Y. C. Xu, S. C. Waring, P. C. OBrien, E. G. Tangalos, G. E. Smith, R. J. Ivnik, and E. Kokmen. Medial temporal atrophy on mri in normal aging and very mild alzheimer's disease. *Neurology*, 49:786790, 1997.

[74] M. Jones, J. Berwick, D. Johnston, and J. Mayhew. Concurrent optical imaging spectroscopy and laser-doppler flowmetry: the relationship between blood flow, oxygenation, and volume in rodent barrel cortex. *Neuroimage*, 13:1002–15, 2001.

[75] D. K. Joseph, T. J. Huppert, M. A. Franceschini, and D. A. Boas. Diffuse optical tomography system to image brain activation with improved spatial resolution and validation with functional magnetic resonance imaging. *Appl Opt*, 45(31), 2006.

[76] V. Jurcak, M. Okamoto, A. Singh, and I. Dan. Virtual 10-20 measurement on mr images for inter-modal linking of transcranial and tomographic neuroimaging methods. *NeuroImage*, 26:1184–1192, 2005.

[77] V. Jurcak, D. Tsuzuki, and I. Dan. 10/20, 10/10, and 10/5 systems revisited: their validity as relative head-surface-based positioning systems. *Neuroimage*, 34(4):1600–11, 2007.

[78] J. A. Kaye, T. Swihart, D. Howieson, A. Dame, M. M. Moore, T. Karnos, R. Camicioli, M. Ball, B. Oken, and G. Sexton. Volume loss of the hippocampus and temporal lobe in healthy elderly persons destined to develop dementia. *Neurology*, 48(5):12971304, 1997.

[79] J. Kiernan and A. Hudson. Frontal lobe atrophy in motor neuron diseases. *Brain*, 117:747757, 1994.

[80] S. Kim and K. Ugurbil. Comparison of blood oxygenation and cerebral blood flow effects in fmri: estimation of relative oxygen consumption change. *Magn Reson Med*, 38:59–65, 1997.

[81] H. Koizumi, T. Yamamoto, A. Maki, Y. Yamashita, H. Sato, H. Kawaguchi, and N. Ichikawa. Optical topography: practical problems and new applications. *Applied Optics*, 42:3054–3062, 2003.

[82] T. Koyama, A. Iwasaki, Y. Ogoshi, and E. Okada. Practical and adequate approach to modeling light propagation in an adult head with low-scattering regions by use of diffusion theory. *Appl Opt*, 44(11):2094–103, 2005.

[83] J. Kwon, R. McMarley, Y. Hirayasu, J. Anderson, I. Fischer, R. Kikinis, F. Jolesz, and M. Shenton. Left planum temporale volume reduction in schizophrenia. *Arch. Gen. Psychiatry*, 56(2):142148, 1999.

[84] A. Li, E. L. Miller, M. E. Kilmer, T. J. Brukilacchio, T. Chaves, J. Stott, Q. Zhang, T. Wu, M. Chorlton, R. H. Moore, D. B. Kopans, and D. A. Boas. Tomographic optical breast imaging guided by three-dimensional mammography. *Appl Opt*, 42(25):5181–5190, 2003.

[85] N. Logothetis. The underpinning of the bold functional magnetic resonance imaging signal. *Journal of Neuroscience*, 23:3963–3971, 2003.

[86] N. Makris, L. M. Angelone, S. Tulloch, S. Sorg, D. Kennedy, and G. Bonmassar. Mri-based comprehensive anatomic model of the human head. *submitted*, 2007.

[87] D. Malonek and A. Grinvald. Interactions between electrical activity and cortical microcirculation revealed by imaging spectroscopy: implications for functional brain mapping. *Science*, 272(5261):551–4, 1996.

[88] J. Mayhew, D. Johnston, J. Martindale, M. Jones, J. Berwick, and Y. Zheng. Increased oxygen consumption following activation of brain: theoretical footnotes using spectroscopic data from barrel cortex. *Neuroimage*, 13:975–87, 2001.

[89] J. Mohr. *Studies in Neurolinguistics*. Academic Press, Witaker H & Witaker NA, New York, 1976.

[90] B. Montcel, R. Chabrier, and P. Poulet. Detection of cortical activation with time-resolved diffuse optical methods. *Applied Optics*, 44:1942 – 1947, 2005.

[91] C. Moore and R. Cao. The hemo-neural hypothesis: On the role of blood flow in information processing. *J Neurophysiol*, 2007.

[92] V. Ntziachristos, A. Yodh, M. Schnall, and B. Chance. Mri-guided diffuse optical spectroscopy of malignant and benign breast lesions. *Neoplasia*, 4(4):347–354, 2002.

[93] G. Ojemann, J. Ojemann, E. Lettich, and M. Berger. Cortical language localization in left, dominant hemisphere. an electical stimulation mapping investigation in 117 patients. *J Neurosurg*, 71:31626, 1989.

[94] E. Okada and D. Delpy. The effect of a non-scattering layer on time-resolved photon migration paths. *Proceedings of the SPIE - The International Society for Optical Engineering*, 3566:2 – 9, 1999.

[95] E. Okada and D. Delpy. Effect of discrete scatterers in csf layer on optical path length in the brain. *Proceedings of the SPIE - The International Society for Optical Engineering Photon Migration, Diffuse Spectroscopy and Optical Coherence Tomography*, 4160:196–203, 2000.

[96] E. Okada and D. Delpy. Near-infrared light propagation in an adult head model. i. modeling of low-level scattering in the cerebrospinal fluid layer. *Applied Optics*, 42(16):2906 – 14, 2003.

[97] E. Okada, M. Firbank, and D. Delpy. Effect of overlying tissue on the spatial sensitivity profile of near-infrared spectroscopy. *Physics in Medicine and Biology*, 40(12):2093 –, 1995.

[98] E. Okada, M. Firbank, M. Schweiger, S. Arridge, M. Cope, and D. Delpy. Theoretical and experimental investigation of near-infrared light propagation in a model of the adult head. *Applied Optics*, 36(1):21 – 31, 1997.

[99] E. Okada, M. Schweiger, S. Arridge, M. Firbank, and D. Delpy. Experimental validation of monte carlo and finite-element methods of estimation of the optical path length in inhomogeneous tissue. *Applied Optics*, 35:3362–3371, 1996.

[100] M. Okamoto and I. Dan. Automated cortical projection of head-surface locations for transcranial functional brain mapping. *NeuroImage*, 26:18–28, 2005.

[101] R. Oostenveld and P. Praamstra. The five percent electrode system for high-resolution eeg and erp measurements. *Clin Neurophysiol*, 112(4):713–9, 2001.

[102] M. Pena, A. Maki, D. Kovacic, G. Dehaene-Lambertz, H. Koizumi, F. Bouquet, and J. Mehler. Sounds and silence: an optical topography study of language recognition at birth. *Proc Natl Acad Sci U S A*, 100:11702–11705, 2003.

[103] W. Penfield and L. Roberts. *Speech and Brain Mechanisms.* Princeton Univ Press, Princeton, 1959.

[104] A. Pfefferbaum and L. Marsh. Structural brain imaging in schizophrenia. *Clin. Neurosci.*, 3(2):105111, 1995.

[105] B. Pogue and K. Paulsen. High-resolution near-infrared tomographic imaging simulations of the rat cranium by use of a priori magnetic resonance imaging structural information. *Optics Letters*, 23:1716–1718, 1998.

[106] J. Riley, S. Arridge, Y. Chrysanthou, H. Dehghani, E. Hillman, and M. Schweiger. The radiosity diffusion model in 3d. *Proceedings of the SPIE - The International Society for Optical Engineering Photon Migration, Optical Coherence Tomography, and Microscopy, 18-21 June 2001*, 4431:153–64, 2001.

[107] H. Rusinek, M. J. de Leon, A. E. George, L. A. Stylopoulos, R. Chandra, G. Smith, T. Rand, M. Mourino, and H. Kowalski. Alzheimer disease: measuring loss of cerebral gray matter with mr imaging. *Radiology (Easton, Pa.)*, 178(1):109114, 1991.

[108] D. Salat, R. Buckner, A. Snyder, D. Greve, R. Desikan, E. Busa, J. Morris, A. Dale, and B. Fischl. Thinning of the cerebral cortex in aging. *Cereb Cortex.*, 14(7), 2004.

[109] N. Shah, A. E. Cerussi, D. Jakubowski, D. Hsiang, J. Butler, and B. J. Tromberg. The role of diffuse optical spectroscopy in the clinical management of breast cancer. *Dis Markers*, 19(2-3):95–105, 2003.

[110] S. Srinivasan, B. W. Pogue, S. Jiang, H. Dehghani, C. Kogel, S. Soho, J. J. Gibson, T. D. Tosteson, S. P. Poplack, and K. D. Paulsen. Interpreting hemoglobin and water concentration, oxygen saturation and scattering measured in vivo by near-infrared breast tomography. *Proc Natl Acad Sci U S A*, 100(21):12349–54, 2003.

[111] J. Steinbrink, H. Wabnitz, H. Obrig, A. Villringer, and H. Rinneberg. Determining changes in nir absorption using a layered model of the human head. *Phys Med Biol*, 46(3):879–896, 2001.

[112] G. Strangman, M. A. Franceschini, and D. A. Boas. Factors affecting the accuracy of near-infrared spectroscopy concentration calculations for focal changes in oxygenation parameters. *Neuroimage*, 18:865–879, 2003.

[113] S. Takahshi and Y. Yamada. Simulation of 3d light propagation in a layered head model including a clear csf layer. *OSA TOPS: Advances in Optical Imaging and Photon Migration*, 21:2 - 6, 1998.

[114] P. Taroni, G. Danesini, A. Torricelli, A. Pifferi, L. Spinelli, and R. Cubeddu. Clinical trial of time-resolved scanning optical mammography at 4 wavelengths between 683 and 975 nm. *J Biomed Opt*, 9(3):464–73, 2004.

[115] K. Uludag, M. Kohl, J. Steinbrink, H. Obrig, and A. Villringer. Cross talk in the lambert-beer calculation for near-infrared wavelengths estimated by monte carlo simulations. *Journal of Biomedical Optics*, 7:51–9, 2002.

[116] A. Villringer and U. Dirnagl. Coupling of brain activity and cerebral blood flow: basis of functional neuroimaging. *Cerebrovasc Brain Metab Rev.*, 7(3):240–76, 1995.

[117] J. P. Vonsattel and M. DiFiglia. Huntington disease. *J. Neuropathol. Exp. Neurol.*, 57(5):369384, 1998.

[118] L. Wang and H. i Wu. *Biomedical Optics: Principles and Imaging.* Wiley, 2007.

[119] L. Wang, S. Jacques, and L. Zheng. Mcml-monte carlo modeling of light transport in multi-layered tissues. *Computer Methods and Programs in Biomedicine*, 47(2):131 - 46, 1995.

[120] T. Wilcox, H. Bortfeld, R. Woods, E. Wruck, and D. A. Boas. Using near-infrared spectroscopy to assess neural activation during object processing in infants. *J Biomed Opt*, 10:11010, 2005.

[121] T. Wolf, U. Lindauer, A. Villringer, and U. Dirnagl. Excessive oxygen or glucose supply does not alter the blood flow response to somatosensory stimulation or spreading depression in rats. *Brain Res*, 761(2):290–9, 1997.

[122] A. Yodh and B. Chance. Spectroscopy and imaging with diffusing photons. *Phys. Today*, pages 34–40, 1995.

[123] R. B. Zipursky, E. K. Lambe, S. Kapur, and D. J. Mikulis. Cerebral gray matter volume deficits in first episode psychosis. *Arch. Gen. Psychiatry*, 55(6):540546, 1998.

[124] R. B. Zipursky, K. O. Lim, E. V. Sullivan, B. W. Brown, and A. Pfefferbaum. Widespread cerebral gray matter volume deficits in schizophrenia. *Arch. Gen. Psychiatry*, 49(3):195205, 1992.